INSTITUTO SUPERIOR TÉCNICO
Universidade Técnica de Lisboa

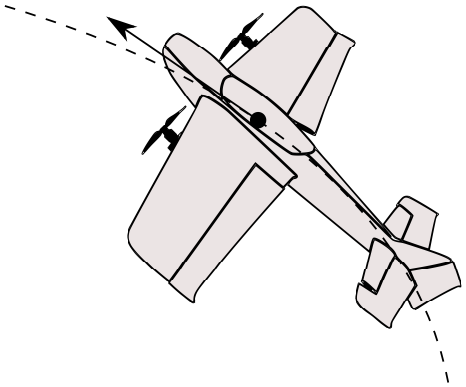

Autonomous Transition Flight for a Vertical Take-Off and Landing Aircraft

Pedro Daniel Graça Casau

Dissertação para obtenção do grau:

Mestre em Engenharia Aeroespacial

Comité de Avaliação

Presidente:	Prof. Doutor João Manuel Lage de Miranda Lemos
Orientador:	Prof. Doutor Carlos Jorge Ferreira Silvestre
Vogal:	Prof. Doutor Miguel Ayala Botto

Setembro 2010

Resumo

A presente tese aborda os problemas de modelação e controlo de um veículo aéreo não tripulado (UAV) de asa fixa em voo vertical e em voo horizontal, assim como o voo de transição entre estes dois estados distintos do envelope de voo. A primeira contribuição desta tese consiste na elaboração de um modelo dinâmico que permita caracterizar o comportamento do UAV tanto em voo vertical como em voo horizontal. O sistema é ainda modelado como um Autómato, no qual comportamento discreto é introduzido através de um supervisor, i.e. um algoritmo que altera o controlador consoante o modo de operação em que o UAV se encontra. A segunda contribuição consiste na realização de um controlador que, através de técnicas de controlo linear permita *i)* estabilização em voo vertical e horizontal e, *ii)* seguimento de uma trajectória de transição. A terceira contribuição consiste na implementação de um controlador não linear que é localmente *input-to-state stable* (ISS), permitindo o seguimento de uma trajectória de transição.

Palavras-chave: aeronaves VTOL, Sistemas Híbridos, Regulador Quadrático Linear, sistemas ISS.

Abstract

This thesis addresses modelling and control problems for an model-scale Unmanned Air Vehicle (UAV) which is intended to perform Vertical Take-Off and Landing (VTOL) autonomously as well as transition to level flight. The first contribution of this thesis is the description of an accurate UAV nonlinear model which captures both hovering and level flight behaviors. Furthermore, the Hybrid Automata framework is introduced into the model by means of *supervisory control* which provides dynamics switching between modes of operation. The second contribution concerns the problems of *i)* Hover and Level Flight stabilization and, *ii)* Transition trajectory tracking by means of linear control techniques. Finally, a control law which renders the system locally Input-to-State Stable (ISS) is designed within the Hybrid Systems' framework allowing for practical trajectory tracking.

Keywords: VTOL aircraft, Hybrid Automata, Linear Quadratic Regulator, ISS systems.

Acknowledgements

I would like to thank my advisor Professor Carlos Silvestre for all the invaluable help and availability throughout this semester.

I would also like to thank David Cabecinhas for all the time spent answering my questions and reviewing my work which would be incomplete had not been for his help.

I wish to thank António Henriques, Anabela Reis, Carlos Henriques, Dário Silva, Duarte Afonso, João Teixeira, Noel Leitão and Nuno Silva for their inconditional support and friendship throughout the course. I'm also grateful to everyone who, in some way or another, has helped me get through these years.

My last thanks go to Margarida and Maria João for their everlasting love, and to my parents Fernando and Teresa to whom I owe everything I have.

The work presented in this thesis was partly funded by Fundação para a Ciência e Tecnologia.

Contents

List of Tables

List of Figures

List of Symbols

Aerodynamics

α	Angle of attack
$\mathcal{AR}$	Aspect ratio
β	Sideslip angle
δ_j	Actuator j deflection
$\mathbf{f}_a$	Aerodynamic force
$\mathbf{m}_a$	Aerodynamic torque
$\mathbf{r}$	Aerodynamic center location
$\overline{\alpha}$	Upper stall angle
ρ	Atmospheric density
$\underline{\alpha}$	Lower stall angle
A	Planform area
C_D	Coefficient of Drag
C_L	Coefficient of Lift
D	Drag
e	Oswald's efficiency
L	Lift
u_p	Propeller slipstream velocity

Dynamics

$\mathbf{I}$	Aircraft tensor of inertia
$\mathbf{p}_B$	Aircraft position.
$\mathbf{v}_B$	Aircraft linear velocity
ϕ	Roll angle
ψ	Yaw angle angle
$\boldsymbol{\omega}_B$	Aircraft angular velocity
θ	Pitch angle
m	Aircraft mass
p	Aircraft roll velocity
q	Aircraft pitch velocity
r	Aircraft yaw velocity
u	Aircraft forward velocity
v	Aircraft lateral velocity
w	Aircraft downward velocity

Gravity

$\mathbf{f}_g$	Gravity force
$\mathbf{m}_g$	Gravity torque
g	Gravity acceleration

Hybrid Automaton

$\bar{\phi}$	Roll angle limits $-\bar{\phi} < \phi < \bar{\phi}$
$\bar{\psi}$	Roll angle limits $-\bar{\psi} < \psi < \bar{\psi}$
$\bar{\theta}$	Pitch angle limits $-\bar{\theta} < \theta < \bar{\theta}$
$\chi_{q_1 \to q_2}$	Neighborhood around reference trajectory starting point $v^*_{q_1 \to q_2}(0)$
$\mathcal{D}$	Domain mapping
$\mathcal{E}$	Set of Edges

$\mathcal{G}$	Guard mapping
$\mathcal{Q}$	Set of Operating Modes
$\mathcal{R}$	Reset map
q	Operating Mode
q^*	Desired Operating Mode
v	Aircraft trajectory
$\boldsymbol{\mu}$	Aircraft actuator input
$\boldsymbol{\xi}$	Aircraft state
$f(q, \boldsymbol{\xi}, \boldsymbol{\mu})$	Flow map

Kinematics

$\mathbf{i}$	Unit vector along the Ox direction
$\mathbf{j}$	Unit vector along the Oy direction
$\mathbf{k}$	Unit vector along the Oz direction
$\{I\}$	Inertial Reference Frame (NED or UEN)
$\{N\}$	North-East-Down coordinate frame (NED)
$\{U\}$	Up-East-North coordinate frame (UEN)
${}^B_I\mathbf{R}$	Rotation matrix from $\{I\}$ to $\{B\}$

Linear controller

$(\mathbf{A}, \mathbf{B}, \mathbf{C}, \mathbf{D})$	Linear state space model
$(\mathbf{Q}, \mathbf{R})$	LQR weighting matrices
$(\boldsymbol{\xi}_0, \boldsymbol{\mu}_0)$	Equilibrium point
$(\tilde{\boldsymbol{\xi}}, \tilde{\boldsymbol{\mu}})$	Deviations from equilibrium
$\bar{\boldsymbol{\xi}}$	Integrator variables
λ	Matrix eigenvalues

Nonlinear controller

$\bar{x}$	Bound on the absolute value of x
Δ	Restrictions on the disturbances
$\delta_u,\ \delta_w,\ \delta_q$	Disturbances
$c_u,\ c_w,\ c_q,\ c_\theta$	Controller restrictions on initial states
$k_u,\ k_w,\ k_q,\ k_\theta$	Controller gains

Propellers

$\mathbf{f}_p$	Propellers' forces
$\mathbf{m}_p$	Propellers' torques
$\mathbf{r}_p$	Propeller location
τ	Propeller input torque
C_P	Coefficient of Power
C_T	Coefficient of Thrust
C_{P_0}	Coefficient of Power at $J = 0$
C_{P_M}	Coefficient of Power at $J = J_M$
C_{T_0}	Coefficient of Thrust at $J = 0$
d	Propeller diameter
I_p	Propeller moment of inertia
J	Advance ratio
J_M	Advance ratio of zero thrust
n	Propeller speed
Q	Propeller drag torque
T	Thrust

Chapter 1

Introduction

The demand for Unmanned Air Vehicles (UAVs) has escalated in the past few years due to their contributions in commercial and defense applications, including fire surveillance and mitigation operations, agricultural fields spraying, infrastructure inspection, among others (see e.g. [1], [2], [3], [4] and [5]). Several UAV configurations have been developed to meet the requirements imposed by such applications, including fixed-wing and tilt wing aircraft, rotorcrafts and ducted-fan vehicles.

Recent developments described in [4], [6] and [7] have shown that fixed-wing Vertical Take-Off and Landing (VTOL) aircrafts can perform both long endurance missions and precise maneuvering within exiguous environments. The versatility of such aircrafts combines helicopter precise trajectory tracking with conventional fixed-wing airplanes ability to cover large distances, delivering a final solution which largely exceeds the capabilities of its predecessors. However, the problem of achieving robust transitions between hover and leveled flights is difficult for its exquisite dynamics. To this end, several control methodologies have been employed, including robust linear control, feedback linearization techniques and adaptive controllers (see e.g. [8], [9], [10] and [11]) but these different approaches still lack a formal proof of stability and robustness.

The very different aircraft dynamics between hover and leveled flights suggest that supervisory control (i.e. the application of different control techniques for each operating mode) is a plausible solution for the given problem. Similar methodologies, like the ones described in [12] and [13], have been successfully employed in a variety of applications. Controller switching during operating mode transitions adds discrete behavior to the continuous UAV model, creating a new layer of complexity which must be dealt appropriately.

Systems which display both continuous and discrete behavior have been under an intense research effort over the last decade. This study has given rise to several concepts such as hybrid automata [14]

and switched systems [15] which fall within the broader category of Hybrid Dynamical Systems described in [12]. The discrete behavior built into these systems may appear naturally for certain applications such as UAV landing and take-off (see e.g. [16] and [17]) but may also be the consequence of digital control or supervisory control [18].
The solution proposed in this thesis employs supervisory control by modeling the small-scale UAV within the Hybrid Automata framework, dividing the aircraft flight envelope into Hover, Transition and Level operating modes. Linear optimal control techniques are employed for system stabilization in hover and level flight while linear and nonlinear control solutions are exploited for stabilization during transition flight.

1.1 Problem Statement

A fixed-wing model-scale UAV is required to perform wide range missions as well as precise docking maneuvers for battery recharging, for example. This mission scope relies on a UAV which has VTOL capabilities, stable level flight, robust transition from hover to level flight and *vice-versa*. A plausible application is described in Figure 1.1. UAV operation described in Figure 1.1 considers a remotely operated UAV which may perform autonomous transitions from and to level flight according to the operator's commands. During the transition the operator does not interact with the UAV. This thesis addresses the problems which are posed by autonomous aircraft operation during the operating modes highlighted in Figure 1.1. This problem is threefold:

1. Elaborate an aircraft dynamic model which accurately depicts its behavior during hover, level flight and transition maneuvers;
2. Build a control law which stabilizes the aircraft dynamics during each operating mode;
3. Verify the controller's robustness.

1.2 State of the Art

The advent of new sensor electronics and high thrust-to-weight small-scale motors has fueled the research of VTOL aircrafts, namely model-scale unmanned air vehicles. The work presented in [4] encompasses the first attempt to study and build a small aircraft with VTOL capabilities. The paper discusses the advantages of a fixed wing aircraft over helicopter and insect-like flying platforms in terms of endurance and maneuverability in near-Earth scenarios, i.e. within highly cluttered terrain. Transition between cruise and hover is tackled with open-loop maneuvers which are tested with a

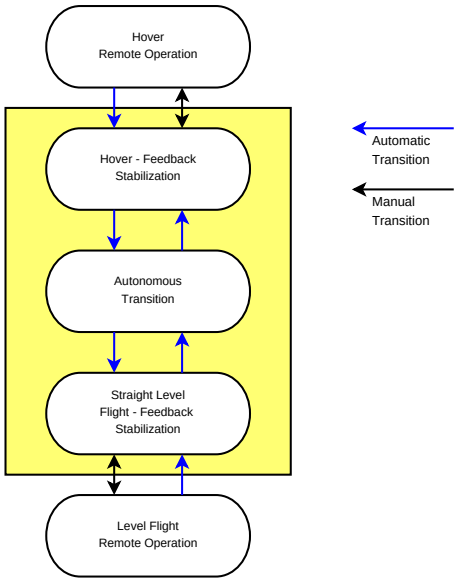

Figure 1.1: UAV Operation Diagram.

very simple model. However, a real world test shows the platform transition capabilities under manual control. The work presented in [6] further develops the aircraft model and provides an implementation for trajectory tracking in hover and level flights using linear control techniques. The transition between the two different modes of operation is achieved by means of open-loop maneuvers and controller switching near the desired operating points. This control strategy successfully provides autonomous transition to a model-scale aircraft. More recently, the work developed in [7] also employed open-loop maneuvers which seem to constitute the most popular option for autonomous transition.

Nevertheless, controlled transition by means of linear optimal techniques has been exploited in [8] and [9] which resorted to computer simulations in order to test the controller's reliability. The thesis [10] and [11] develop adaptive gain-scheduled controllers which are computationally expensive and rely on accurate parameter estimation in order to achieve stable reference tracking.

1.3 Thesis outline

This thesis is divided into three major chapters:

- Chapter 2 which describes the aircraft dynamic model;
- Chapter 3 which proceeds into linear control techniques development;
- Chapter 4 which introduces a novel method for nonlinear transition control.

Each chapter is structured along the same lines. They begin with a brief introduction to concepts and previous results which are relevant for the remaining analysis. Then, a description of the developed work is presented. In Chapters 3 and 4 simulation results are also presented before the chapter summary.

The appendixes provide complementary information to the subjects discussed throughout this text.

Chapter 2

Nonlinear UAV Model

Throughout this chapter a nonlinear model is developed for an UAV with a conventional wing/tail configuration. The aircraft has two propellers mounted on each side of a trapezoidal wing which provide thrust and whose backward driven flow (otherwise known as *slipstream*) interacts with the free-stream flow resulting from the aircraft motion, creating aerodynamic forces and moments. The set of available aircraft actuators are:

- Propellers - the aircraft has two propellers mounted on each fore side of the wing whose main purpose is to provide thrust, but they may also provide lateral stabilization through differential control;

- Rudder - it is located aft of the vertical stabilizer and provides lateral control;

- Elevator - it is located aft of the horizontal stabilizer and provides pitch control;

- Ailerons/flaps - these two terms are used to distinguish the differential mode (ailerons) and the common mode (flaps) of the actuators located aft of the wing. The ailerons provide roll control while the flaps control the amount of lift that the wing produces.

The propeller, aerodynamic and gravity forces are all accounted for when describing the vehicle dynamics and kinematics which are introduced in Sections 2.3 and 2.2. The UAV nonlinear model introduced in these sections is represented by (2.1) with system state $\boldsymbol{\xi} \in \mathbb{R}^{14}$ and actuators input $\boldsymbol{\mu} \in \mathbb{R}^{6}$. The standard aircraft dynamics nomenclature described in [19] is employed in both state and

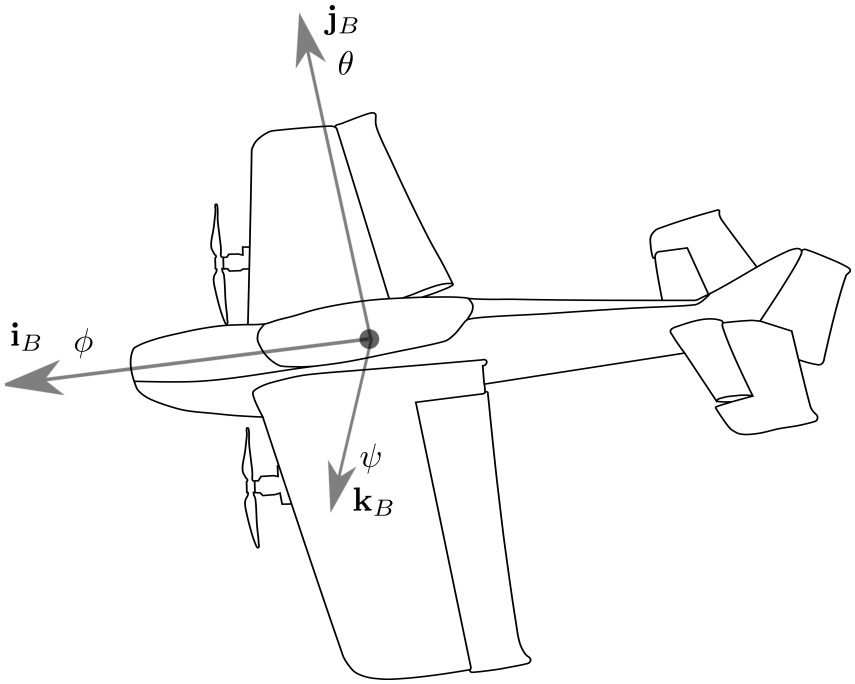

Figure 2.1: Aircraft Body Reference Frame and Actuators.

input variables (see Table 2.1).

$$\dot{\boldsymbol{\xi}} = f(\boldsymbol{\xi}, \boldsymbol{\mu}) \tag{2.1}$$

$$\boldsymbol{\xi} = [n_1 \quad n_2 \quad u \quad v \quad w \quad p \quad q \quad r \quad \phi \quad \theta \quad \psi \quad x \quad y \quad z]^T \tag{2.2}$$

$$\boldsymbol{\mu} = [\tau_1 \; \tau_2 \; \delta_a \; \delta_e \; \delta_r \; \delta_f] \tag{2.3}$$

Section 2.4 further extends the UAV nonlinear model to an UAV hybrid automaton.

2.1 Notation

Due to immense number of symbols which embody the parameters included in the aircraft model equations, a set of rules is required to improve their clarity. Such rules are presented in this section.

- Scalar values are represented by either uppercase and lowercase letters (example: ρ and A);
- Vectors are represented by boldface lowercase letters (example: $\mathbf{v}$);
- Matrices are represented by boldface uppercase letters (example: $\mathbf{I}$);
- Coordinate frames are represented by a capital letter in closed brackets (example: $\{I\}$);
- The identity $\frac{\partial A}{\partial x} = A_x$ will be often used to represent derivatives;

- A set of subscript letters are used to identify the source of any given attribute. w, hs, vs, p, e, r, a and f identify the wing, horizontal stabilizer, vertical stabilizer, propeller, elevator, rudder, aileron and flaps, respectively (example: A_w is the wing's planform area);
- Superscripts identify the vector's coordinate frame (example: ${}^N\mathbf{v}_B$ is the aircraft velocity with coordinates given in the NED reference frame and ${}^U\mathbf{v}_B$ is the same vector with coordinates given in the UEN reference frame).

2.2 Aircraft Kinematics

The aircraft kinematics are a description of the aircraft's position and attitude which depend on its linear and angular velocities. This description requires the definition of the following coordinate reference frames:

- North-East-Down (NED);
- Up-East-North (UEN);
- Body Reference Frame (BRF);

2.2.1 The NED frame

The North-East-Down reference frame $\{N\}$ is an orthogonal reference frame defined by the right handed set of unitary vectors $\{\mathbf{i}_N, \mathbf{j}_N, \mathbf{k}_N\}$ whose origin is at some point in the Earth's surface with a given latitude and longitude as depicted in Figure 2.2.

- $\mathbf{i}_N$ is tangent to the earth's surface and points to the geographic North;
- $\mathbf{j}_N$ is normal to $\mathbf{i}_N$, tangent to the Earth's surface and points to the East;
- $\mathbf{k}_N$ completes the right handed set.

For the purpose of modeling the motion of a unmanned air vehicle, this reference frame will be considered an inertial reference frame, i.e. Earth is considered flat and still.

2.2.2 The UEN frame

The Up-East-North reference frame $\{U\}$ is an orthogonal reference frame defined by the right handed set of unitary vectors $\{\mathbf{i}_U, \mathbf{j}_U, \mathbf{k}_U\}$ whose origin is coincident with that of the NED frame.

Variable	Units	Description
$n_{1,2}$	Hz	Propeller 1(2) speed.
$\mathbf{v}_B = [u\ v\ w]^T$	m/s	Aircraft's linear velocity.
$\boldsymbol{\omega}_B = [p\ q\ r]^T$	rad/s	Aircraft's angular velocity.
ϕ	rad	Roll angle.
θ	rad	Pitch angle.
ψ	rad	Yaw Angle.
${}^N\mathbf{p}_B = [x\ y\ z]^T$	m	Position in three dimensional space (NED reference frame).
$\tau_{1,2}$	N.m	Propeller 1(2) input torque.
δ_a	rad	Aileron deflection.
δ_e	rad	Elevator deflection.
δ_r	rad	Rudder deflection.
δ_f	rad	Flap deflection.

Table 2.1: State and Input variables description.

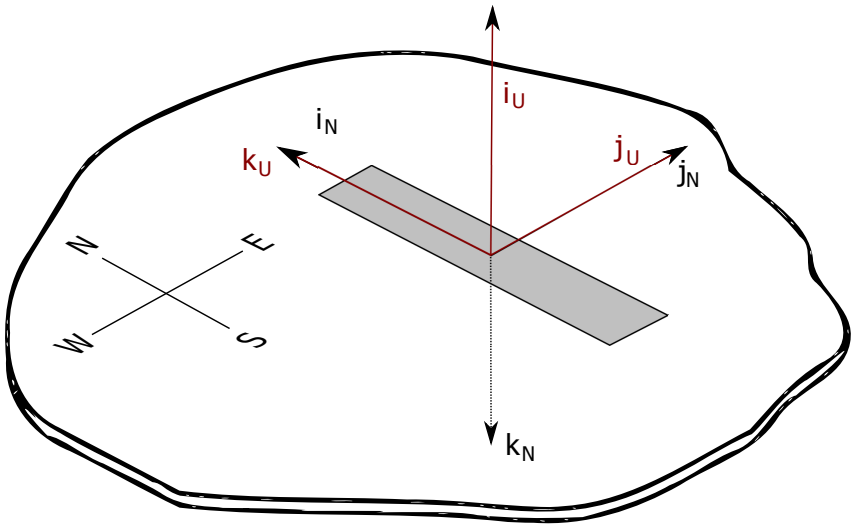

Figure 2.2: North-East-Down and Up-East-North reference frames

- $\mathbf{k}_U$ is tangent to the earth's surface and points to the geographic North;
- $\mathbf{j}_U$ is normal to $\mathbf{k}_U$, tangent to the Earth's surface and points to the East;
- $\mathbf{i}_U$ completes the right handed set.

For the purpose of modeling the motion of a unmanned air vehicle, this reference frame will also be considered an inertial reference frame.

2.2.3 The BRF frame

The Body Reference Frame $\{B\}$ has its origin in the aircraft center of gravity and is defined orthogonal and right handed set of unitary vectors $\{\mathbf{i}_B, \mathbf{j}_B, \mathbf{k}_B\}$ which satisfy the following specifications:

- $\mathbf{i}_B$ is collinear with the aircraft's zero lift axis which lies on the symmetry plane (roll axis);
- $\mathbf{j}_B$ is normal to the symmetry plane (pitch axis);
- $\mathbf{k}_B$ completes the right handed set (yaw axis).

Each of the axis in the Body Reference Frame are related with very well known angles from aircraft flight mechanics literature.

2.2.4 Rotations in 3-Dimensional Space

Each of the reference frames defined earlier can be obtained from each other by means of linear transformations which are represented by matrices with the properties:

1. Matrix ${}^B_I\mathbf{R}$ maps vector coordinates in $\{I\}$ to $\{B\}$, i.e. ${}^B\mathbf{v} = {}^B_I\mathbf{R}{}^I\mathbf{v}$;[1]
2. Rotation matrix inverse is represented by changing the subscript with the superscript, i.e. $({}^B_I\mathbf{R})^T = {}^I_B\mathbf{R}$;
3. Rotation matrix inverse equals its transpose, i.e. ${}^B_I\mathbf{R}({}^B_I\mathbf{R})^{-1} = {}^B_I\mathbf{R}{}^I_B\mathbf{R} = \mathbf{E}$ where $\mathbf{E}$ is the identity matrix;
4. The rotation does not change the length of the base vectors, therefore $\det({}^B_I\mathbf{R}) = 1$;
5. The rotation matrix is given by

$$ {}^B_I\mathbf{R} = \begin{bmatrix} {}^I\mathbf{i}_B.{}^I\mathbf{i}_I & {}^I\mathbf{i}_B.{}^I\mathbf{j}_I & {}^I\mathbf{i}_B.{}^I\mathbf{k}_I \\ {}^I\mathbf{j}_B.{}^I\mathbf{i}_I & {}^I\mathbf{j}_B.{}^I\mathbf{j}_I & {}^I\mathbf{j}_B.{}^I\mathbf{k}_I \\ {}^I\mathbf{k}_B.{}^I\mathbf{i}_I & {}^I\mathbf{k}_B.{}^I\mathbf{j}_I & {}^I\mathbf{k}_B.{}^I\mathbf{k}_I \end{bmatrix}. \tag{2.4} $$

[1] The reference frame $\{I\}$ is a representation of any given inertial reference frame.

6. Its derivative is given by

$$\dot{{}^B_I\mathbf{R}} = S^T(\boldsymbol{\omega}_B){}^B_I\mathbf{R}, \tag{2.5}$$

where $S(x) \in \mathbb{R}^{3\times3}$ is the skew symmetric matrix such that $S(x)y = x \times y$ for all $x, y \in \mathbb{R}^3$.

This set of linear transformations builds the well-known SO(3) group [20] which is parametrized by three independent parameters which can be specified in different ways, each of which has its own advantages and disadvantages. The most widely used parametrizations are

- Euler Angles
- Quaternions
- Angle-Axis

Using Euler Angles parametrization, the rotation matrix ${}^B_I\mathbf{R}$ is the result of three rotations around the basis vectors. These rotations can be ordered in several different ways, e.g. 3-2-1 is usually used to indicate that the first rotation is performed around the Oz axis, then around the Oy axis of the rotated frame and finally around the Ox axis. The 3-2-1 rotation is the most common choice in aircraft applications for it is related with the very well-known yaw, pitch and roll angles whose representation is the triplet (ϕ, θ, ψ). These parameters map the rotation matrix according to

$${}^B_I\mathbf{R} = \begin{bmatrix} \cos\psi\cos\theta & \sin\psi\cos\theta & -\sin\theta \\ \cos\psi\sin\theta\sin\phi - \sin\psi\cos\phi & \sin\psi\sin\theta\sin\phi + \cos\psi\cos\phi & \cos\theta\sin\phi \\ \cos\phi\sin\theta\cos\psi + \sin\psi\sin\phi & \sin\psi\sin\theta\cos\phi - \cos\psi\sin\phi & \cos\theta\cos\phi \end{bmatrix}. \tag{2.6}$$

The 3-2-1 Euler angles derivatives are

$$\begin{aligned} \dot{\phi} &= p + (r\cos\phi + q\sin\phi)\tan\theta, \\ \dot{\theta} &= q\cos\phi + r\sin\phi, \\ \dot{\psi} &= (r\cos\phi + q\sin\phi)/\cos\theta. \end{aligned} \tag{2.7}$$

This parametrization has the obvious drawback of having singularities when $\theta = \pm90^\circ$, but it has some advantages with respect to the other options which are discussed in [8]. Using the inertial frame $\{U\}$ while in Hover and $\{N\}$ while in Level Flight (with appropriate switching) avoids these singularities and provides all the benefits of choosing such intuitive parameters.

2.2.5 Position in 3-Dimensional Space

The position description is much simpler than the attitude description. The current position is the integral over time of the aircraft velocity after an appropriate change of reference frame. In the current application, the aircraft position is computed in the NED reference frame by

$$\dot{{}^N\mathbf{p}}_B = {}^N_B\mathbf{R}\mathbf{v}_B. \tag{2.8}$$

2.3 Dynamics

The aircraft dynamic model is obtained from the application of the second Newton's law to rigid bodies which results into the equations

$$\sum_{j=1}^{n} \mathbf{f}_j = m(\dot{\mathbf{v}}_B + \boldsymbol{\omega}_B \times \mathbf{v}_B), \tag{2.9}$$

$$\sum_{j=1}^{m} \mathbf{m}_j = \mathbf{I}\dot{\boldsymbol{\omega}}_B + \boldsymbol{\omega}_B \times (\mathbf{I}\boldsymbol{\omega}_B), \tag{2.10}$$

where $\mathbf{I} \in \mathbb{R}^{3\times3}$ is the vehicle's tensor of inertia and $m \in \mathbb{R}$ is its mass. The propellers, aerodynamic loads and gravity produce the forces and moments which affect the aircraft's behavior and are described by the equations

$$\sum_{j=1}^{n} \mathbf{f}_j = \mathbf{f}_g + \mathbf{f}_p + \mathbf{f}_a, \tag{2.11}$$

$$\sum_{j=1}^{n} \mathbf{m}_j = \mathbf{m}_g + \mathbf{m}_p + \mathbf{m}_a, \tag{2.12}$$

where the subscripts g, p and a stand for gravity, propellers and aerodynamic interactions, respectively, which are discussed in the following subsections.

2.3.1 Gravity

The force $\mathbf{f}_g$ is easily described in the inertial coordinate frames because it is directed downwards along the positive Oz axis in $\{N\}$ and along negative Ox axis in $\{U\}$. The gravity force must be described in the coordinate frame $\{B\}$ therefore the required axis transformation is given by (2.15).

$${}^{N}\mathbf{f}_g = [0\ 0\ mg]^T \tag{2.13}$$

$${}^{U}\mathbf{f}_g = [-mg\ 0\ 0]^T \tag{2.14}$$

$$\mathbf{f}_g = {}^{B}_{I}\mathbf{R}^{I}\mathbf{f}_g \tag{2.15}$$

The moment $\mathbf{m}_g$ is present due to center of gravity displacement with respect to the center of mass, but for applications such as UAV motion control, this term is usually neglected.

2.3.2 Propeller

A propeller is a collection of infinitesimal airfoils distributed with a certain angle γ over its radius. Blade element theory is usually used to find the Coefficient of Thrust (C_T) and Coefficient of Power

(C_P) which depend on the propeller geometry, Reynolds number (Re) and Advance Ratio (J) given by

$$C_T = C_T(Re, J, shape), \tag{2.16}$$

$$C_P = C_P(Re, J, shape), \tag{2.17}$$

$$J = \frac{u}{nd}, \tag{2.18}$$

where u is the free-stream velocity normal to the propeller's plane (the propeller's plane is therefore assumed to be yOz in the aircraft body reference frame), n is the propeller's rotation speed and d denotes the propeller's diameter. According to [21] the dependence with the Reynolds number may be neglected and because the propeller's geometry is usually known, C_T and C_P become functions of the advance ratio only and are reasonably approximated by

$$C_T = C_{T_0}\left(1 - \frac{J}{J_M}\right) \tag{2.19}$$

$$C_P = C_{P_0} + \left(\frac{J}{J_M}\right)^2 (C_{P_M} - C_{P_0}) \tag{2.20}$$

where C_{T_0} is the Coefficient of Thrust at zero velocity, C_{P_0} is the Coefficient of Power at zero velocity,

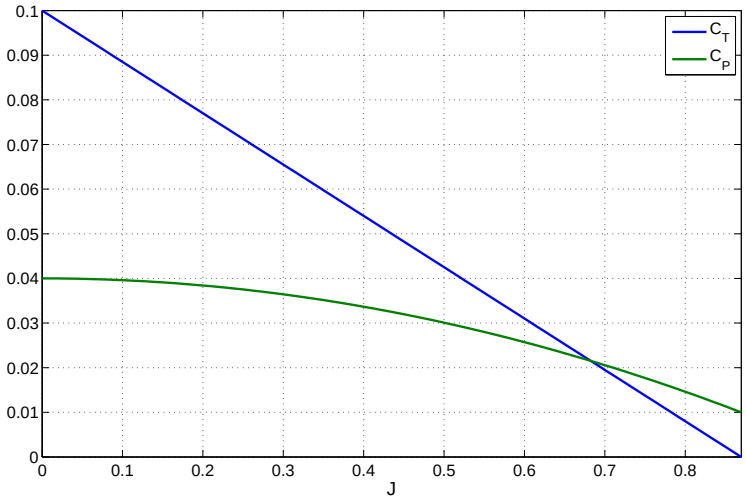

Figure 2.3: Coefficient of Thrust and Coefficient of Power curves with data from Section 2.5.

J_M is the advance ratio of zero thrust and C_{P_M} is the Coefficient of Power at $J = J_M$. The coefficients in (2.16) and (2.17) are related with the propeller's thrust and power according to

$$T = \rho n^2 d^4 C_T(J), \tag{2.21}$$

$$P = \rho n^3 d^5 C_P(J), \tag{2.22}$$

where ρ is the atmospheric density.

The propeller does not instantaneously change its velocity because it has to overcome resisting torques which counteract the input torque. The propeller's dynamic model is approximated by

$$I_p 2\pi \dot{n} = \tau - Q, \tag{2.23}$$

where I_p is its moment of inertia (along the symmetry axis), τ is the input torque and Q is the aerodynamic drag torque acting on the propeller which is given by

$$Q = \frac{P}{2\pi n}. \tag{2.24}$$

The set of moments acting on the aircraft body due to propeller rotation ($\mathbf{m}_p$) includes the acceleration torque ($\mathbf{m}_{acc}$), the drag torque ($\mathbf{m}_{drag}$), the gyroscopic torque ($\mathbf{m}_{gyro}$) and the displacement torque ($\mathbf{m}_{dis}$) which arises from the displacement $\mathbf{r}_p$ of the propeller's center with respect to the center of gravity.

$$\mathbf{m}_{p_i} = \mathbf{m}_{acc_i} + \mathbf{m}_{drag_i} + \mathbf{m}_{gyro_i} + \mathbf{m}_{dis_i} \tag{2.25}$$

$$\mathbf{m}_{acc_i} = (-1)^i [I_p 2\pi \dot{n}_i \; 0 \; 0]^T \tag{2.26}$$

$$\mathbf{m}_{drag_i} = (-1)^i [Q_i \; 0 \; 0]^T \tag{2.27}$$

$$\mathbf{m}_{gyro_i} = (-1)^i \boldsymbol{\omega}_B \times [I_p 2\pi n_i \; 0 \; 0]^T \tag{2.28}$$

$$\mathbf{m}_{dis_i} = \mathbf{r}_{p_i} \times [T_i \; 0 \; 0]^T \tag{2.29}$$

The subscript $i \in \{1, 2\}$ in the formulæ above distinguishes each propeller and their moments' signs change according to the propeller's rotation. Although some forces in the propeller's disk plane appear when the free stream flow is not normal to it, these forces may be neglected because they are much smaller than the aerodynamic forces acting on the aircraft body. Therefore, thrust will be considered normal to the propeller's disk from here on. The total thrust and torque produced by the propellers is given by the following equations.

$$\mathbf{f}_p = \begin{bmatrix} T_{p_1} + T_{p_2} \\ 0 \\ 0 \end{bmatrix} \tag{2.30}$$

$$\mathbf{m}_p = \mathbf{m}_{p_1} + \mathbf{m}_{p_2} \tag{2.31}$$

So far the discussion concerned solely the set of forces and moments acting on the aircraft body due to the propeller's rotation. However, this rotation produces a backward flow which is named *slipstream* (which has velocity u_p) that acts upon the aircraft's lifting surfaces. Equation (2.32) is derived in

Appendix B and is valid under the assumptions that the airflow is inviscid, incompressible and steady, that is, it does not vary over time.

$$T = \frac{1}{2}\rho\frac{\pi d^2}{4}(u_p^2 - u^2) \tag{2.32}$$

2.3.3 Aerodynamics

Modeling the aircraft aerodynamics is usually the hardest but also the most important task in order to achieve a reliable model. The work presented in this section has [6] as a major reference.

In general, the interaction between the propellers' slipstream, the aircraft body and the free stream flow is very complex but it is the control engineer duty to simplify the reality down to some basic relations which capture the most important phenomenonæ occurring in the system. The most simple relation which describes the interaction between the slipstream and the free-stream flows is achieved using superposition, which means that the forces and moments produced by the aircraft's lifting surfaces are considered separately for the slipstream and for the free-stream flows and added together in the end. Under this assumption the slipstream velocity is given by

$$u_p = \sqrt{\frac{8T}{\rho\pi d^2}}, \tag{2.33}$$

which is calculated by algebraic inversion of (2.32) considering null forward velocity $u = 0$.

Some relevant aerodynamic quantities are the angle of attack (α) and the sideslip angle (β) which are defined by

$$\alpha = \arctan\left(\frac{w}{u}\right), \tag{2.34}$$

$$\beta = \arcsin\left(\frac{v}{||\mathbf{v}_B||}\right). \tag{2.35}$$

The lift produced when $\alpha = 0$ is null because the axis Ox is collinear with the aircraft's zero lift axis. For $\alpha \neq 0$ the lift and the drag of a generic surface i[2], is given by (2.36) and (2.37), which greatly depend on the surface's *Coefficient of Lift* (C_L) and the *Coefficient of Drag* (C_D).

$$L_i = \frac{1}{2}\rho A_i \|\mathbf{v}_B\|^2 C_{L_i} \tag{2.36}$$

$$D_i = \frac{1}{2}\rho A_i \|\mathbf{v}_B\|^2 C_{D_i} \tag{2.37}$$

In their most generic description, C_L and C_D are functions of the actuator deflection and system's state, first order derivatives, second order derivatives and so on. However, a suitable description of

[2]The subscript i can be replaced by any identifier. w, a, hs, vs identify the wing, aileron, horizontal stabilizer and vertical stabilizer surfaces. The subscript p is used to identify propeller dependent properties. The subscript j can be replaced by the identifier a, e, r or f which identify the ailerons, elevator, rudder and flaps, respectively.

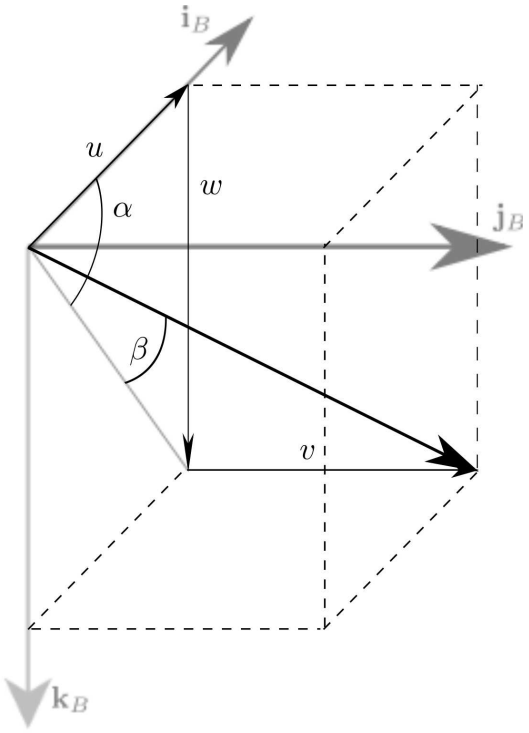

Figure 2.4: Sideslip and Angle of Attack representation in the body axis.

these coefficients is achieved by the relations

$$C_L = C_L(\alpha, \delta_j), \tag{2.38}$$

$$C_D = C_{D_0} + \frac{C_L^2}{\pi \mathcal{A}\mathcal{R} e}, \tag{2.39}$$

where δ_j is the deflection of the surface's actuator (if any), C_{D_0} is the friction Coefficient of Drag, $\mathcal{AR}$ is the surface's aspect ratio and e is its efficiency. Under the small angle approximation, the relation (2.40) is valid and the surfaces' lift and drag are easily calculated[3].

$$C_L = \begin{cases} C_{L_\alpha}\alpha + C_{L_{\delta_j}}\delta_j, & \text{if } -C_{L_{max}} \leq C_L \leq C_{L_{max}} \\ 0, & \text{otherwise} \end{cases} \tag{2.40}$$

It is noticeable from (2.40) that C_L is lower bounded at $-C_{L_{max}}$ and upper bounded at $C_{L_{max}}$. These limits induce loss of lift (stall) at angles of attack such that $\alpha \notin [\underline{\alpha}, \bar{\alpha}]$ where

$$\bar{\alpha}(\delta_j) = \frac{C_{L_{max}} - C_{L_{\delta_j}}\delta_j}{C_{L_\alpha}}, \tag{2.41}$$

$$\underline{\alpha}(\delta_j) = -\frac{C_{L_{max}} + C_{L_{\delta_j}}\delta_j}{C_{L_\alpha}}. \tag{2.42}$$

The following equations are derived from the application of (2.36) and (2.37) to the wing, horizontal

[3]Under the small angle approximation other simplifications are performed: the transformation from the wind axis is not performed, i.e. lift is created along the negative Oz axis of the Body Reference Frame and drag appears in the negative Ox axis. Furthermore, it will be considered that $\|\mathbf{v}_B\|^2 \simeq u^2$.

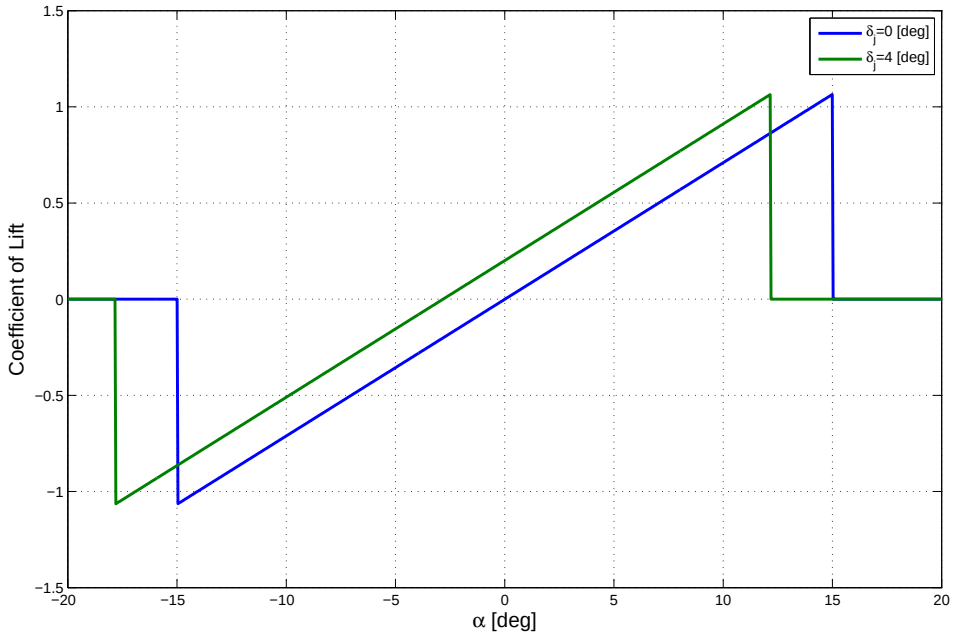

Figure 2.5: Coefficient of Lift vs Angle of Attack. The figure also shows an upward shift due to actuator deflection which reduces the stall angle.

stabilizer and vertical stabilizer.

$$L_w = 1 - \frac{1}{2}\rho A_w u^2 C_{L_w} - \frac{1}{2}\rho A_{p,w}\left(u_{p_1}^2 + u_{p_2}^2\right) C_{L_{p,w}} \tag{2.43a}$$

$$D_w = -\frac{1}{2}\rho A_w u^2 \left(C_{D_{0_w}} + \frac{C_{L_w}^2}{\pi \mathcal{R}_w e_w}\right) - \frac{1}{2}\rho A_{p,w}(u_{p_1}^2 + u_{p_2}^2)\left(C_{D_{0_{p,w}}} + \frac{C_{L_{p,w}}^2}{\pi \mathcal{R}_w e_w}\right) \tag{2.43b}$$

$$L_{vs} = -\frac{1}{2}\rho A_{vs} u^2 \left(C_{L_{\beta_{vs}}}\beta - C_{L_{\delta_{r_{vs}}}}\delta_r\right) + \frac{1}{2}\rho A_{p,vs}\left(\frac{u_{p1}^2 + u_{p2}^2}{2}\right) C_{L_{\delta_{r_{p,vs}}}}\delta_r \tag{2.43c}$$

$$D_{vs} = -\frac{1}{2}\rho A_{vs} u^2 \left(C_{D_{0_{vs}}} + \frac{C_{L_{vs}}^2}{\pi \mathcal{R}_{vs} e_{vs}}\right) - \frac{1}{2}\rho A_{p,vs}(u_{p_1}^2 + u_{p_2}^2)\left(C_{D_{0_{p,vs}}} + \frac{C_{L_{p,vs}}^2}{\pi \mathcal{R}_{vs} e_{vs}}\right) \tag{2.43d}$$

$$L_{hs} = -\frac{1}{2}\rho A_{hs} u^2 \left(C_{L_{\delta_{e_w}}}\delta_e + C_{L_{\alpha_{hs}}}\alpha\right) - \frac{1}{2}\rho A_{p,hs}\left(u_{p1}^2 + u_{p2}^2\right) C_{L_{\delta_{e_{p,hs}}}}\delta_e \tag{2.43e}$$

$$D_{hs} = -\frac{1}{2}\rho A_{hs} u^2 \left(C_{D_{0_{hs}}} + \frac{C_{L_{hs}}^2}{\pi \mathcal{R}_{hs} e_{hs}}\right) - \frac{1}{2}\rho A_{p,hs}(u_{p_1}^2 + u_{p_2}^2)\left(C_{D_{0_{p,hs}}} + \frac{C_{L_{p,hs}}^2}{\pi \mathcal{R}_{hs} e_{hs}}\right) \tag{2.43f}$$

The aileron deflection δ_a does not contribute to the wing lift because a downward deflection on a side of the wing is compensated with a upward deflection on the other side. The aerodynamic forces acting in the aircraft are given by (2.44) under the small angle approximation.

$$\mathbf{f}_a = \begin{bmatrix} D_w + D_{hs} + D_{vs} \\ L_{vs} \\ L_w + L_{hs} \end{bmatrix} \tag{2.44}$$

In order to calculate the moments acting in the aircraft the distances of the aileron's mean pressure center ($\mathbf{r}_a$), its slipstream mean pressure center ($\mathbf{r}_{p,a}$), horizontal stabilizer's aerodynamic center ($\mathbf{r}_{hs}$),wing's aerodynamic center ($\mathbf{r}_w$) and vertical stabilizer's aerodynamic center ($\mathbf{r}_{vs}$) are included in the equations that follow.

$$M_a = -\frac{1}{2}\rho u^2 A_a \mathbf{r}_a.\mathbf{j}_B C_{L_{\delta_{a_w}}} \delta_a - \frac{1}{2}\rho \left(u_{p1}^2 + u_{p2}^2\right) A_{p,a} \mathbf{r}_{p,a}.\mathbf{j}_B C_{L_{\delta_{a_{p,w}}}} \delta_a \tag{2.45}$$

$$\mathbf{m}_{hs} = \mathbf{r}_{hs} \times [0\ 0\ L_{hs}]^T \tag{2.46}$$

$$\mathbf{m}_{vs} = \mathbf{r}_{vs} \times [0\ L_{vs}\ 0]^T \tag{2.47}$$

$$\mathbf{m}_w = \mathbf{r}_w \times [0\ 0\ L_w]^T \tag{2.48}$$

The last term in the aerodynamic moments is a damping moment which is caused by the slipstream lag [4] and also an angle of attack increase in the tail due to rotation. The stabilizing moment produced due to this effect is depicted in Figures 2.6a and 2.6b and it is described by the relations

$$M_{damp_q} = -\frac{1}{2}\rho A_{p,hs} C_{L_{\alpha_{hs}}} q(\mathbf{r}_p.\mathbf{i}_B - \mathbf{r}_{hs}.\mathbf{i}_B)\left(u_{p_1} + u_{p_2}\right) - \frac{1}{2}\rho A_{hs} C_{L_{\alpha_{hs}}} (\mathbf{r}_{hs}.\mathbf{i}_B)^2 qu \tag{2.49}$$

$$M_{damp_r} = -\frac{1}{2}\rho A_{p,vs} C_{L_{\alpha_{vs}}} r(\mathbf{r}_p.\mathbf{i}_B - \mathbf{r}_{vs}.\mathbf{i}_B)(u_{p_1} + u_{p_2}) - \frac{1}{2}\rho A_{vs} C_{L_{\beta_{vs}}} (\mathbf{r}_{vs}.\mathbf{i}_B)^2 ru \tag{2.50}$$

The aerodynamic moment $\mathbf{m}_a$ is defined by

$$\mathbf{m}_a = \mathbf{m}_w + \mathbf{m}_{hs} + \mathbf{m}_{vs} + \begin{bmatrix} M_a \\ M_{damp_q} \\ M_{damp_r} \end{bmatrix}. \tag{2.51}$$

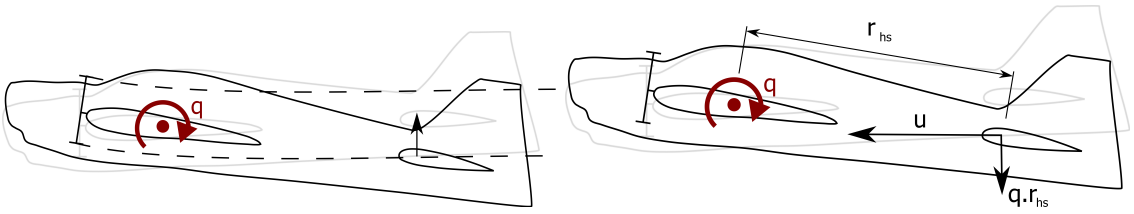

(a) Damping pitch moment due to propellers lag.

(b) Damping moment due to pitch rotation.

Figure 2.6: Damping pitch moment.

2.4 Hybrid Automaton

Although the differential equations which model the UAV dynamics are continuous, discrete behaviour is built into the model due to controller switching when performing a transition between operating

[4] The time $\Delta t = \frac{\mathbf{r}_p.\mathbf{i}_B - \mathbf{r}_{(hs,vs)}.\mathbf{i}_B}{u_p}$ the slipstream takes to reach the tail due to finite slipstream velocity u_p.

modes. This discrete behaviour is modelled by means of a Hybrid Automaton represented in Figure 2.7 which requires the definition of the operating modes, the domain mapping, the flow map, the guard mapping and the reset map. The full hybrid automata framework is presented in [14].
The controllers which are used in Hover, Transition and Level operating modes are identified by $\boldsymbol{\mu}_H$, $\boldsymbol{\mu}_X$ and $\boldsymbol{\mu}_L$, respectively. These controllers are dependent on the current aircraft state $\boldsymbol{\xi}$ but also on the reference trajectory for a given transition from the operating mode q_1 to q_2 the $\boldsymbol{\xi}^*_{q_1 \to q_2}(t)$. Furthermore, a new input variable $q^* \in \mathcal{Q}^* = \{H, L\}$ is required to inform the controller which is the desired Operating Mode and whether transition is required.

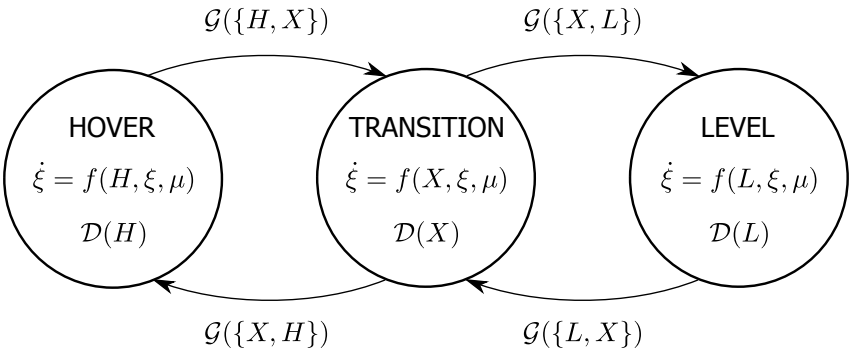

Figure 2.7: UAV Hybrid Automaton with three states: Hover (H); Transition(X); Level Flight (L)

2.4.1 Operating Modes

The hybrid automaton operating mode q must belong to the set $\mathcal{Q} = \{H, X, L\}$ which has the meaning

- H - Hover operating mode with Hover controller selected, i.e. $\boldsymbol{\mu} = \boldsymbol{\mu}_H(\boldsymbol{\xi}, \boldsymbol{\xi}^*(t))$;
- X - Transition operating mode with Transition controller selected, i.e. $\boldsymbol{\mu} = \boldsymbol{\mu}_X(\boldsymbol{\xi}, \boldsymbol{\xi}^*(t))$;
- L - Level operating mode with Level controller selected, i.e. $\boldsymbol{\mu} = \boldsymbol{\mu}_L(\boldsymbol{\xi}, \boldsymbol{\xi}^*(t))$.

2.4.2 Flow Map

The flow map $f : \mathcal{Q} \times \mathbb{R}^{14} \times U \to \mathbb{R}^{14}$ describes the evolution of the state variables in each operating mode $q \in \mathcal{Q}$, i.e. in each operating mode the state's derivative is given by

$$\dot{\boldsymbol{\xi}} = f(q, \boldsymbol{\xi}, \boldsymbol{\mu}_q) \tag{2.52}$$

where function f is the the set of previously defined differential equations (2.7), (2.8), (2.9) and (2.10).

Variable	Value/deg
$\bar{\phi}_H$	180
$\bar{\theta}_H$	15
$\bar{\psi}_H$	15
$\bar{\phi}_X$	180
$\bar{\theta}_X$	90
$\bar{\psi}_X$	180
$\bar{\phi}_L$	15
$\bar{\theta}_L$	15
$\bar{\psi}_L$	180

Table 2.2: Domain Mapping variables definition. Notice that $\bar{\phi}_H = 180°$ and $\bar{\psi}_L = 180°$ because the corresponding states do not interfere with the dynamics, i.e. they are pure integrators.

2.4.3 Domain Mapping

For each operating mode, the domain mapping $\mathcal{D} : \mathcal{Q} \rightrightarrows \mathbb{R}^{14} \times \mathbb{R}^6 \times \mathcal{Q}^*$ assigns the set where the variables $(\boldsymbol{\xi}, \boldsymbol{\mu}_q)$ may range. The actuators physical limits are therefore built into the model with the domain mapping $\mathcal{D}$ and the definition of the set U in (2.53).

$$U = [\tau_{min}, \tau_{max}]^2 \times [\delta_{a_{min}}, \delta_{a_{max}}] \times [\delta_{e_{min}}, \delta_{e_{max}}] \times [\delta_{r_{min}}, \delta_{r_{max}}] \times [\delta_{f_{min}}, \delta_{f_{max}}] \times \mathcal{Q}^* \tag{2.53}$$

The domain mapping defined below is built under the knowledge that Up-East-North inertial reference frame is used to model aircraft kinematics during Hover and Transition while North-East-Down inertial reference frame is used during Level[5].

$$\begin{aligned}
\mathcal{D}(H) =& [n_{min}, n_{max}]^2 \times \mathbb{R}^6 \times B_{\bar{\phi}_H}(0) \times B_{\bar{\theta}_H}(0) \times B_{\bar{\psi}_H}(0) \times \mathbb{R}^2 \times \mathbb{R}_{\leq 0} \times U \\
\mathcal{D}(X) =& [n_{min}, n_{max}]^2 \times \mathbb{R}_{\geq 0} \times \mathbb{R}^5 \times B_{\bar{\phi}_X}(0) \times B_{\bar{\theta}_X}(0) \times B_{\bar{\psi}_X}(0) \times \mathbb{R}^2 \times \mathbb{R}_{<0} \times U \\
\mathcal{D}(L) =& [n_{min}, n_{max}]^2 \times \mathbb{R}_{\geq 0} \times \mathbb{R}^5 \times B_{\bar{\phi}_L}(0) \times B_{\bar{\theta}_L}(0) \times B_{\bar{\psi}_L}(0) \times \mathbb{R}^2 \times \mathbb{R}_{<0} \times U \bigcap \\
& \{(u, w) \in \mathbb{R}_{>0} \times \mathbb{R} : \underline{\alpha} < \arctan(w/u) < \bar{\alpha}\}
\end{aligned} \tag{2.54}$$

In the domain dapping $\mathcal{D}$, a suitable choice of the variables $\bar{\theta}_H$ and $\bar{\theta}_L$ (see Figure 3.4 is required for the Hover and Level operating modes domains to lie within the corresponding basin of attraction, i.e. if $\mathcal{B}_q$ is the basin of attraction for the operating mode q then $\mathcal{D}(q) \subset \mathcal{B}_q$. The Transition controller should work for the whole flight envelope. Furthermore, positive longitudinal velocity is required in Transition and Level operating modes and the aircraft is required to be always above ground (otherwise it would crash).

[5] $B_R(\mathbf{p})$ represents the Ball of radius $R \in \mathbb{R}$ around point $\mathbf{p} \in \mathbb{R}^n$, i.e. the set $\{\mathbf{x} \in \mathbb{R}^n : \|\mathbf{x} - \mathbf{p}\| < R\}$

2.4.4 Edges

The set of edges $\mathcal{E} \subset \mathcal{Q} \times \mathcal{Q}$ identifies any operating mode transition from q_1 to q_2 represented in Figure 2.7 with the pair (q_1, q_2). The possible operating mode transitions in this model are

$$\begin{array}{ll} (H,X) & (X,L) \\ (L,X) & (X,H) \end{array}$$

2.4.5 Guard Mapping

The Guard Mapping $\mathcal{G} : \mathcal{E} \rightrightarrows \mathbb{R}^{14} \times \mathbb{R}^6 \times \mathcal{Q}^*$ determines for each pair (q_1, q_2) the set to which the aircraft state must belong in order to perform the transition. The switch to Transition flight will be performed only if the aircraft state is close enough to the reference trajectory which is described by

$$v^*_{X\to q}(t) = (\boldsymbol{\xi}^*_{X\to q}(t), \boldsymbol{\mu}^*_{X\to q}(t)),$$

where $X \to q$ identifies the approach maneuver from the operating mode X to the operating mode $q \in \{H, L\}$. Switching from Transition to either Hover or Level is performed whenever the aircraft state belongs to some set X_q such that $X_q \subset \mathcal{D}(q)$ where $q \in \{H, L\}$ identifies Hover or Level Flight Operating points.

$$\begin{aligned} \mathcal{G}(H,X) =& B_{\chi_{H\to X}}(v^*_{X\to L}(0)) \\ \mathcal{G}(X,L) =& \left\{(\boldsymbol{\xi},\boldsymbol{\mu}) \in \mathcal{D}(L) : |\phi| \le \bar{\phi}_{X\to L} \wedge |\theta| \le \bar{\theta}_{X\to L} \wedge |\psi| \le \bar{\psi}_{X\to L} \wedge q^* = L\right\} \\ \mathcal{G}(L,X) =& B_{\chi_{L\to X}}(v^*_{X\to H}(0)) \\ \mathcal{G}(X,H) =& \left\{(\boldsymbol{\xi},\boldsymbol{\mu}) \in \mathcal{D}(L) : |\phi| \le \bar{\phi}_{X\to H} \wedge |\theta| \le \bar{\theta}_{X\to H} \wedge |\psi| \le \bar{\psi}_{X\to H} \wedge q^* = H\right\} \end{aligned} \tag{2.55}$$

The variables $\bar{\phi}_{X\to H}$, $\bar{\phi}_{X\to L}$, $\bar{\theta}_{X\to H}$, $\bar{\theta}_{X\to H}$, $\bar{\psi}_{X\to H}$ and $\bar{\psi}_{X\to L}$ have a 13 degree value which is consistent with the condition $X_q \subset \mathcal{D}(q)$. The variables $\chi_{H\to X}$ and $\chi_{L\to X}$ have different values depending on the controller robustness. In Chapter 3 they take the value 0.1 while in Chapter 4 their value must be such that the controller restrictions on initial conditions are not violated. A guard mapping representation is given in Figure 2.8a. As an example, Figure 2.8b depicts the pitch angle domain and transition boundaries in Level which are identified by $\bar{\theta}_L$ and $\bar{\theta}_{X\to L}$, respectively. The domains and boundaries in terms of roll and yaw angles are similarly defined.

2.4.6 Reset Map

For each $(q_1, q_2) \in \mathcal{E}$ and $(\boldsymbol{\xi}, \boldsymbol{\mu}) \in \mathcal{G}(q_1, q_2)$, the reset map $\mathcal{R} : \mathcal{E} \times \mathbb{R}^{14} \times U \to \mathbb{R}^{14} \times U$ identifies the jump of the state variable $\boldsymbol{\xi}$ during the operating mode transition from q_1 to q_2. State changes occur

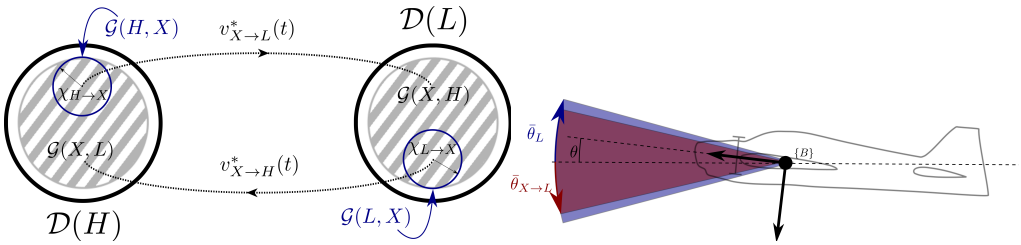

(a) Guard mapping representation. (b) Pitch angle domain and transition boundaries in Level.

Figure 2.8: Guard mapping and domain mapping representations.

when switching from Transition to Level due to different attitude parametrization between the operating modes. The reset map is given by

$$\begin{aligned}
\mathcal{R}(H,X) &= \boldsymbol{\xi},\\
\mathcal{R}(X,L) &= [n_1\ n_2\ u\ v\ w\ p\ q\ r\ \arctan({}^B_N\mathbf{R}_{23}/{}^B_N\mathbf{R}_{33})\ \arcsin(-{}^B_N\mathbf{R}_{13})\ \arctan({}^B_N\mathbf{R}_{12}/{}^B_N\mathbf{R}_{11})\ x\ y\ z]^T,\\
\mathcal{R}(L,X) &= [n_1\ n_2\ u\ v\ w\ p\ q\ r\ \arctan({}^B_U\mathbf{R}_{23}/{}^B_U\mathbf{R}_{33})\ \arcsin(-{}^B_U\mathbf{R}_{13})\ \arctan({}^B_U\mathbf{R}_{12}/{}^B_U\mathbf{R}_{11})\ x\ y\ z]^T,\\
\mathcal{R}(X,H) &= \boldsymbol{\xi},
\end{aligned} \tag{2.56}$$

where the symbol $\mathbf{R}_{ij}$ is the matrix $\mathbf{R}$ element which is found at the i-th row and j-th column.

2.5 Model Parameters

The tables comprised in this section list the model parameters' values which are used in subsequent sections to perform aircraft dynamic simulations using the simulation environment described in Appendix C. The parameters have been estimated for the model-scale UAV depicted in Figure 2.9 according to the details presented in Appendix A.

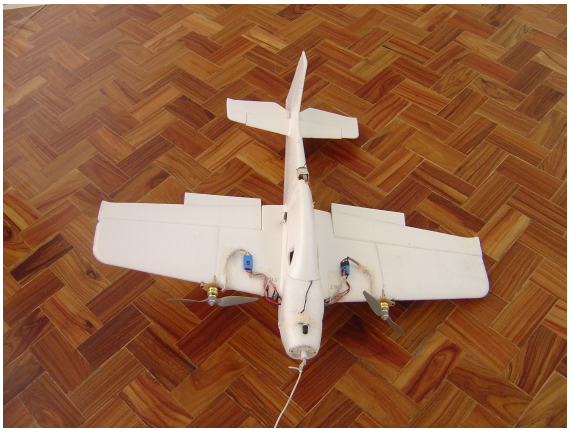

Figure 2.9: Model-scale UAV.

Symbol	Value	Units	Description
$\mathbf{r}_{p_1}$	$[0.1\ 0.21\ 0]^T$	m	Propeller 1 location
$\mathbf{r}_{p_2}$	$[0.1\ -0.21\ 0]^T$	m	Propeller 2 location
d	0.23	m	Propellers diameter
I_p	10^{-5}	kg.m^2	Propellers moment of inertia
C_{T_0}	0.1	-	Propeller's initial Coefficient of Thrust
C_{P_0}	0.04	-	Propeller's initial Coefficient of Power
n_{max}	200	rps	Propeller's maximum speed (rotations per second)
n_{min}	0	rps	Propeller's minimum speed (rotations per second)
τ_{max}	0.2	N.m	Propeller's maximum torque
τ_{min}	0	rps	Propeller's minimum torque
T_{max}	13.7	N	Propeller's maximum Thrust
T_{min}	0	rps	Propeller's minimum Thrust

Table 2.3: Propellers parameters.

Symbol	Value	Units	Description
m	1.64	kg	Aircraft Mass
$\mathbf{I}_x$	0.06	kg.m^2	Aircraft's Principal Moment of Inertia (Ox axis)
$\mathbf{I}_y$	0.08	kg.m^2	Aircraft's Principal Moment of Inertia (Oy axis)
$\mathbf{I}_z$	0.13	kg.m^2	Aircraft's Principal Moment of Inertia (Oz axis)

Table 2.4: Aircraft body parameters.

Symbol	Value	Units	Description
$\mathbf{r}_{hs}$	$[-0.56\ 0\ 0]^T$	m	Horizontal Stabilizer aerodynamic center location
$c_{r_{hs}}$	0.15	m	Horizontal Stabilizer root chord
$c_{t_{hs}}$	0.1	m	Horizontal Stabilizer tip chord
b_{hs}	0.46	m	Horizontal Stabilizer span
Λ_{hs}	6.2	deg	Horizontal Stabilizer sweep
A_{hs}	0.0575	m^2	Horizontal Stabilizer planform area
$A_{p,hs}$	0.015	m^2	Slipstream washed area
$\mathcal{R}_{hs}$	3.68	-	Horizontal Stabilizer aspect ratio
$C_{L_{\alpha_{hs}}}$	4.07	rad^{-1}	Horizontal Stabilizer $\partial C_L/\partial\alpha$
$C_{D_{0_{hs}}}$	0.01	-	Horizontal Stabilizer Parasitic Coefficient of Drag
e	0.8	m	Horizontal Stabilizer efficiency
$C_{L_{\delta_{e_{hs}}}}$	4.07	rad^{-1}	Horizontal Stabilizer $\partial C_L/\partial\delta_e$
$C_{L_{\delta_{e_{p,hs}}}}$	4.07	rad^{-1}	Slipstream washed Horizontal Stabilizer $\partial C_L/\partial\delta_a$

Table 2.5: Horizontal stabilizer parameters.

Symbol	Value	Units	Description
$\mathbf{r}_{vs}$	$[-0.63\ 0\ 0]^T$	m	Vertical Stabilizer aerodynamic center location
$c_{r_{vs}}$	0.12	m	Vertical Stabilizer root chord
$c_{t_{vs}}$	0.09	m	Vertical Stabilizer tip chord
b_{vs}	0.26	m	Vertical Stabilizer span
A_{vs}	0.0273	m^2	Vertical Stabilizer planform area
$A_{p,vs}$	0.006	m^2	Slipstream washed area
$\mathcal{AR}_{hs}$	2.48	-	Vertical Stabilizer aspect ratio
$C_{L_{\alpha_{vs}}}$	4.07	rad^{-1}	Vertical Stabilizer $\partial C_L/\partial\alpha$
$C_{D_{0_{vs}}}$	0.01	-	Vertical Stabilizer Parasitic Coefficient of Drag
e	0.8	m	Vertical Stabilizer efficiency
$C_{L_{\delta_{r_{vs}}}}$	3.48	rad^{-1}	Vertical Stabilizer $\partial C_L/\partial\delta_r$
$C_{L_{\delta_{r_{p,vs}}}}$	3.48	rad^{-1}	Slipstream washed Vertical Stabilizer $\partial C_L/\partial\delta_a$

Table 2.6: Vertical stabilizer parameters.

Symbol	Value	Units	Description
$\mathbf{r}_w$	$[0.03\ 0\ 0]^T$	m	Wing aerodynamic center location
c_{r_w}	0.33	m	Wing root chord
c_{t_w}	0.22	m	Wing tip chord
b_w	1.07	m	Wing span
Λ_w	5.9	deg	Wing sweep
A_w	0.29	m^2	Wing planform area
$A_{p,w}$	0.066	m^2	Slipstream washed area
$\mathcal{AR}_w$	3.89	-	Wing aspect ratio
$C_{L_{\alpha_w}}$	4.15	rad^{-1}	Wing $\partial C_L/\partial\alpha$
$C_{D_{0_w}}$	0.01	-	Wing Parasitic Coefficient of Drag
e	0.8	m	Wing efficiency
$C_{L_{\delta_{a_w}}}$	2.88	rad^{-1}	Wing $\partial C_L/\partial\delta_a$
$C_{L_{\delta_{f_w}}}$	2.88	rad^{-1}	Wing $\partial C_L/\partial\delta_f$
$C_{L_{\delta_{a_{p,w}}}}$	3.63	rad^{-1}	Slipstream washed wing $\partial C_L/\partial\delta_a$
$C_{L_{\delta_{f_{p,w}}}}$	3.63	rad^{-1}	Slipstream washed wing $\partial C_L/\partial\delta_f$
$\mathbf{r}_a$	$[0\ 0.3\ 0]^T$	m	Aileron center of pressure
$\mathbf{r}_{p,a}$	$[0\ 0.2\ 0]^T$	m	Aileron slipstream washed center of pressure

Table 2.7: Wing parameters.

2.6 Summary

This chapter was focused on the aircraft dynamics and kinematics modeling which employed standard flight dynamics nomenclature. The kinematics description required the definition of the coordinate frames:

- North-East-Down (NED);
- Up-East-North (UEN);
- Body Reference Frame (BRF),

where the first two are considered to be inertial reference frames whose origin is located at the same point on the Earth's surface. The UEN is obtained from NED by means of the rotation matrix ${}^{U}_{N}\mathbf{R}$ while BRF requires a translation by the vector ${}^{I}\mathbf{p}_{B}$ and a rotation which is given by the matrix ${}^{B}_{I}\mathbf{R}$. Euler angles constitute the chosen SO(3) parametrization instead of quaternions and angle-axis parametrizations, providing the benefits of working with more intuitive parameters.

The system dynamics require the definition of external forces and moments acting on the aircraft which are divided into three classes:

- Gravity;
- Propellers, and;
- Aerodynamics.

The aerodynamic forces have two contributions resulting from the free-stream flow and the propeller slipstream flow. These contributions are calculated separately and combined together using the superposition principle.

In the end, the system's description is fine-tuned in order to include the switching events which are induced by supervisory control. This task is accomplished within the Hybrid Automata framework, which divides the flight envelope into three operating modes: Hover, Transition and Level. The Hover and Level operating modes are identified by two disjoint sets which are connected together by means of a reference maneuver to be executed within the Transition operating mode's domain. The control laws which allow Level and Hover stabilization as well as reference tracking are exploited in the next chapters.

Chapter 3

Linear Quadratic Regulator

This chapter briefly describes the Linear Quadratic Regulator in Section 3.1 and then proceeds into the required UAV model linearization in Section 3.2. Reference trajectories design, controller synthesis and simulation results are presented in Sections 3.3, 3.4 and 3.5, respectively.

3.1 Description

Given a state-space model

$$\begin{aligned} \dot{\boldsymbol{\xi}}(t) &= \mathbf{A}(t)\boldsymbol{\xi}(t) + \mathbf{B}(t)\boldsymbol{\mu}(t) \\ \mathbf{z} &= \mathbf{C}(t)\boldsymbol{\xi}(t) + \mathbf{D}(t)\boldsymbol{\mu}(t), \end{aligned} \tag{3.1}$$

where $\boldsymbol{\mu} \in \mathbb{R}^m$ is the actuators input, $\boldsymbol{\xi} \in \mathbb{R}^n$ is the system state and $\mathbf{z} \in \mathbb{R}^k$ is the observations vector, the Linear Quadratic Regulator (LQR) provides an optimal feedback control solution for it minimizes the cost function

$$\mathcal{J} = \frac{1}{2}\int_0^\infty \boldsymbol{\xi}^T\mathbf{Q}\boldsymbol{\xi} + \boldsymbol{\mu}^T\mathbf{R}\boldsymbol{\mu}dt. \tag{3.2}$$

This solution requires the state-space model to be controllable[1] and observable[2], producing the full state feedback control law (3.3) (see [22]).

$$\boldsymbol{\mu} = -\mathbf{K}\boldsymbol{\xi} \tag{3.3}$$

The LQR control structure has already been extensively studied and is categorized as very reliable, for it has high gain and phase margins [23]. This control solution requires the system to be linear, however it has been proved that stabilization of a nonlinear system is also feasible within a neighbourhood of the equilibrium point [24].

[1] The linear system in (3.1) is controllable if the matrix $\mathbf{W} = [\mathbf{B}\ \mathbf{AB}\ \mathbf{A}^2\mathbf{B}\ \ldots\ \mathbf{A}^n\mathbf{B}]$ has rank n

[2] The linear system in (3.1) is observable if the matrix $\mathbf{V} = [\mathbf{C}^T\ \mathbf{A}^T\mathbf{C}^T\ (\mathbf{A}^2)^T\mathbf{C}^T\ \ldots\ (\mathbf{A}^{n-1})^T\mathbf{C}^T]$ has rank n

3.2 UAV Linear Model

It is possible to linearize (2.1) around the operating point $(\boldsymbol{\xi}_0, \boldsymbol{\mu}_0)$ using a first order Taylor expansion.

$$\dot{\tilde{\boldsymbol{\xi}}} \simeq \tilde{\boldsymbol{\xi}}_0 + \left.\frac{\partial f}{\partial \boldsymbol{\xi}}\right|_{\boldsymbol{\xi}=\boldsymbol{\xi}_0} \tilde{\xi} + \left.\frac{\partial f}{\partial \boldsymbol{\mu}}\right|_{\boldsymbol{\mu}=\boldsymbol{\mu}_0} \tilde{\boldsymbol{\mu}} \tag{3.4}$$

The terms $\tilde{\boldsymbol{\xi}} = \boldsymbol{\xi} - \boldsymbol{\xi}_0$ and $\tilde{\boldsymbol{\mu}} = \boldsymbol{\mu} - \boldsymbol{\mu}_0$ in (3.4) depict the state and input deviations from the equilibrium point. The matrix $\mathbf{A} = \partial f/\partial \boldsymbol{\xi}|_{\boldsymbol{\xi}=\boldsymbol{\xi}_0}$ supplies important information about the aircraft dynamic properties at a given equilibrium point through the inspection of its eigenvalues. In level flight these can be sorted out according to very well-known aircraft modes [19]: Phugoid, Short-Period, Spiral, Roll and Dutch Roll.

As stated in Chapter 1 the UAV transition should take the aircraft from an equilibrium point in Hover to another equilibrium point in straight level flight. During the transition, the UAV spans a large set of different operating points therefore posing a serious threat on aircraft stability within the flight envelope.

3.2.1 Hover

Given an operating point $(\boldsymbol{\xi}_{H_0}, \boldsymbol{\mu}_{H_0}) \in \mathcal{D}(H)$ which lies within the aircraft Hover domain, the matrix pair $(\mathbf{A}_H, \mathbf{B}_H) \in \mathbb{R}^{14\times 14} \times \mathbb{R}^{14\times 6}$ characterizes the system's dynamics near the prescribed operating point[3].

$$\begin{aligned} \boldsymbol{\xi}_{H_0} &\simeq [154.7 \quad 154.7 \quad 0 \quad 0 \quad 0 \quad 0 \quad 0 \quad 0 \quad 0 \quad \pi/2 \quad 0 \quad 0 \quad 0 \quad -1]^T \\ \boldsymbol{\mu}_{H_0} &\simeq [0.12 \quad 0.12 \quad 0 \quad 0 \quad 0 \quad 0]^T \end{aligned} \tag{3.5}$$

A generic description of matrices $\mathbf{A}_H$ and $\mathbf{B}_H$ is provided in (3.6) and (3.7) which gives useful insight on the system dynamics near the hover operating point.

$$\mathbf{A}_H = \begin{bmatrix} \frac{\partial \dot{n}_1}{\partial n_1} & 0 & 0 & 0 & 0 & 0 & 0 & 0 & 0 & 0 & 0 & 0 & 0 & 0 \\ 0 & \frac{\partial \dot{n}_2}{\partial n_2} & 0 & 0 & 0 & 0 & 0 & 0 & 0 & 0 & 0 & 0 & 0 & 0 \\ \frac{\partial \dot{u}}{\partial n_1} & \frac{\partial \dot{u}}{\partial n_1} & \frac{\partial \dot{u}}{\partial u} & 0 & 0 & 0 & 0 & 0 & 0 & 0 & 0 & 0 & 0 & 0 \\ 0 & 0 & 0 & 0 & 0 & 0 & 0 & 0 & 0 & 0 & g & 0 & 0 & 0 \\ 0 & 0 & 0 & 0 & 0 & 0 & 0 & 0 & 0 & -g & 0 & 0 & 0 & 0 \\ 0 & 0 & 0 & 0 & 0 & \frac{\partial \dot{p}}{\partial p} & 0 & 0 & 0 & 0 & 0 & 0 & 0 & 0 \\ 0 & 0 & 0 & 0 & 0 & 0 & \frac{\partial \dot{q}}{\partial q} & 0 & 0 & 0 & 0 & 0 & 0 & 0 \\ \frac{\partial \dot{r}}{\partial n_1} & \frac{\partial \dot{r}}{\partial n_2} & 0 & 0 & 0 & 0 & 0 & \frac{\partial \dot{r}}{\partial r} & 0 & 0 & 0 & 0 & 0 & 0 \\ 0 & 0 & 0 & 0 & 0 & 1 & 0 & 0 & 0 & 0 & 0 & 0 & 0 & 0 \\ 0 & 0 & 0 & 0 & 0 & 0 & 1 & 0 & 0 & 0 & 0 & 0 & 0 & 0 \\ 0 & 0 & 0 & 0 & 0 & 0 & 0 & 1 & 0 & 0 & 0 & 0 & 0 & 0 \\ 0 & 0 & 0 & 0 & 1 & 0 & 0 & 0 & 0 & 0 & 0 & 0 & 0 & 0 \\ 0 & 0 & 0 & 1 & 0 & 0 & 0 & 0 & 0 & 0 & 0 & 0 & 0 & 0 \\ 0 & 0 & -1 & 0 & 0 & 0 & 0 & 0 & 0 & 0 & 0 & 0 & 0 & 0 \end{bmatrix} \tag{3.6}$$

[3]The chosen operating point may or may not be an equilibrium point, i.e. the relation $\dot{\tilde{\boldsymbol{\xi}}}_0 = 0$ does not necessarily hold.

$$\mathbf{B}_H = \begin{bmatrix} \frac{\partial \dot{n}_1}{\partial \tau_1} & 0 & 0 & 0 & 0 & 0 \\ 0 & \frac{\partial \dot{n}_2}{\partial \tau_2} & 0 & 0 & 0 & 0 \\ 0 & 0 & 0 & 0 & 0 & 0 \\ 0 & 0 & 0 & 0 & \frac{\partial \dot{v}}{\partial \delta_r} & 0 \\ 0 & 0 & 0 & \frac{\partial \dot{w}}{\partial \delta_e} & 0 & \frac{\partial \dot{w}}{\partial \delta_f} \\ \frac{\partial \dot{p}}{\partial \tau_1} & \frac{\partial \dot{p}}{\partial \tau_2} & \frac{\partial \dot{p}}{\partial \delta_a} & 0 & 0 & 0 \\ 0 & 0 & 0 & \frac{\partial \dot{q}}{\partial \delta_e} & 0 & \frac{\partial \dot{q}}{\partial \delta_f} \\ 0 & 0 & 0 & 0 & \frac{\partial \dot{r}}{\partial \delta_r} & 0 \\ 0 & 0 & 0 & 0 & 0 & 0 \\ 0 & 0 & 0 & 0 & 0 & 0 \\ 0 & 0 & 0 & 0 & 0 & 0 \\ 0 & 0 & 0 & 0 & 0 & 0 \\ 0 & 0 & 0 & 0 & 0 & 0 \\ 0 & 0 & 0 & 0 & 0 & 0 \end{bmatrix} \tag{3.7}$$

During hover the dynamics are characterized by a very small set of parameters which can be computed using the data provided in Section 2.5. The results are listed in Table 3.1.

Parameter	Value	Units	Description
$\frac{\partial \dot{n}_{1,2}}{\partial n_{1,2}}$	-24.7278	s^{-1}	Stabilizing torque due to rotor friction.
$\frac{\partial \dot{u}}{\partial n_{1,2}}$	0.0634	m/s	Longitudinal acceleration provided by increased torque rotation.
$\frac{\partial \dot{u}}{\partial u}$	-0.3169	s^{-1}	Longitudinal velocity damping.
$\frac{\partial \dot{p}}{\partial p}$	0	s^{-1}	Roll damping is not present in the nonlinear model therefore it is not part of its linearization.
$\frac{\partial \dot{q}}{\partial q}$	-8.0084	s^{-1}	Pitch damping.
$\frac{\partial \dot{r}}{\partial n_{1,2}}$	$\mp$0.2143	rad/s	Increased propeller 1 rotation provides negative yawing moment while increased propeller 2 rotation provides positive yawing moment.
$\frac{\partial \dot{r}}{\partial r}$	-2.0976	s^{-1}	Yaw damping.
$\frac{\partial \dot{n}_{1,2}}{\partial \tau_{1,2}}$	15195	$N^{-1}m^{-1}s^{-2}$	Increased input torque increases propeller rotation.
$\frac{\partial \dot{v}}{\partial \delta_r}$	2.5706	$ms^{-2}rad^{-1}$	Lateral acceleration due to rudder deflection.
$\frac{\partial \dot{w}}{\partial \delta_e}$	-15.1889	$ms^{-2}rad^{-1}$	Vertical acceleration due to elevator deflection.
$\frac{\partial \dot{w}}{\partial \delta_f}$	-57.7593	$ms^{-2}rad^{-1}$	Vertical acceleration due to flap deflection.
$\frac{\partial \dot{p}}{\partial \tau_{1,2}}$	$\mp$20.8333	$rad\,s^{-2}N^{-1}m^{-1}$	Rolling moment due to differential propeller acceleration.
$\frac{\partial \dot{p}}{\partial \delta_a}$	-399.2930	s^{-2}	Roll acceleration due to aileron deflection.
$\frac{\partial \dot{q}}{\partial \delta_e}$	-217.9611	s^{-2}	Pitch acceleration due to elevator deflection.
$\frac{\partial \dot{q}}{\partial \delta_f}$	44.8958	s^{-2}	Pitch acceleration due to flap deflection.
$\frac{\partial \dot{r}}{\partial \delta_r}$	-25.6826	s^{-2}	Yaw acceleration due to rudder deflection.

Table 3.1: Hover linear model parameters.

Taking into account the set of parameters provided in Table 3.1 it is possible to outline some dynamics features which characterize the aircraft behavior while in hover.

- Despite having two propellers there are no cross-coupled torques which usually arise from gyroscopic effects because the propellers are counter-rotating at the same speed;
- Out of all lifting surface actuators, the highest torque is provided by the ailerons due to their higher surface size;
- Both flaps and elevator act upon the same axis therefore creating lifting forces and pitch moments but their purposes are very different. The elevator is used mainly to provide pitching moments while the flaps are used to provide wing lift control;
- Rudder, Ailerons and propellers differential control can be used to provide lateral stabilization.

A quantitative analysis is made by inspection of matrix $\mathbf{A}_H$ eigenvalues $\boldsymbol{\lambda}_H$. It has five poles on the Left Half-Plane (LHP) which identify the damping of n_1, n_2, u, q and r while the remaining poles are located at the complex plane's origin identifying them as integrators (see Figure 3.1).

$$\boldsymbol{\lambda}_H = [-24.7 \ -24.7 \ -0,317\,0\,0\,0 \ -8.01 \ -2.10\,0\,0\,0\,0\,0\,0]^T \tag{3.8}$$

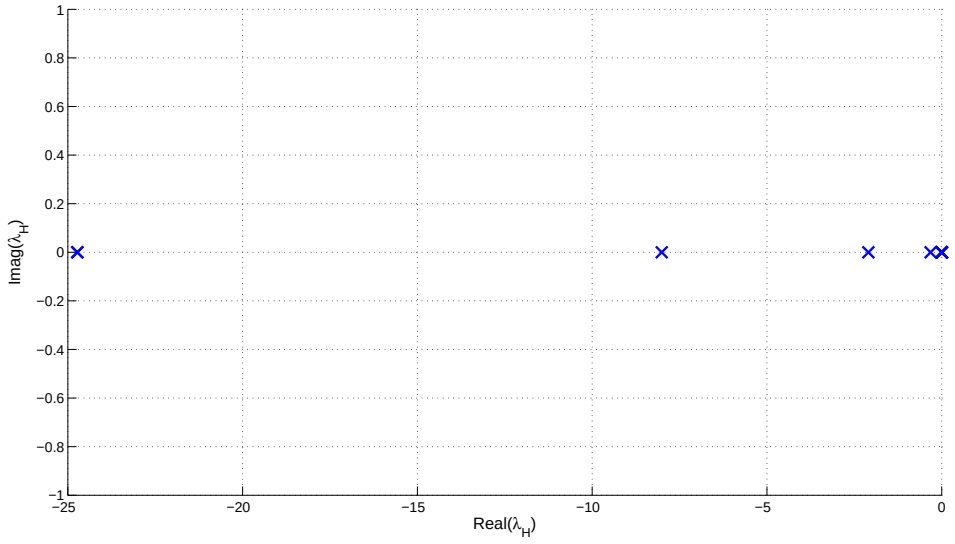

Figure 3.1: Hover operating point pole map. There are five stable poles and nine integrators overlapped at the complex plane's origin.

3.2.2 Level

Given an operating point $(\boldsymbol{\xi}_{L_0}, \boldsymbol{\mu}_{L_0}) \in \mathcal{D}(L)$ which lies within the aircraft Level operating mode domain, the matrix pair $(\mathbf{A}_L, \mathbf{B}_L) \in \mathbb{R}^{14\times14} \times \mathbb{R}^{14\times6}$ characterizes the system's dynamics near the prescribed operating point. A low velocity for the straight level flight operating point was chosen because it requires additional control effort. The height z_0 was arbitrarily chosen for it does not affect the dynamics, i.e. it is a pure integrator.

$$\begin{aligned}\boldsymbol{\xi}_{L_0} &\simeq [112.4 \quad 112.4 \quad 10.8 \quad 0 \quad 1.9 \quad 0 \quad 0 \quad 0 \quad 0 \quad \pi/18 \quad 0 \quad -1]^T \\ \boldsymbol{\mu}_{H_0} &\simeq [0.052 \quad 0.052 \quad 0 \quad -0.065 \quad 0 \quad 0]^T\end{aligned} \tag{3.9}$$

A generic description of matrices $\mathbf{A}_L$ and $\mathbf{B}_L$ is provided in (3.10) and (3.11) which also display important information about the system near the level flight operating point.

$$\mathbf{A}_L = \begin{bmatrix}
\frac{\partial \dot{n}_1}{\partial n_1} & 0 & \frac{\partial \dot{n}_1}{\partial u} & 0 & 0 & 0 & 0 & 0 & 0 & 0 & 0 & 0 & 0 & 0 \\
0 & \frac{\partial \dot{n}_2}{\partial n_2} & \frac{\partial \dot{n}_2}{\partial u} & 0 & 0 & 0 & 0 & 0 & 0 & 0 & 0 & 0 & 0 & 0 \\
\frac{\partial \dot{u}}{\partial n_1} & \frac{\partial \dot{u}}{\partial n_1} & \frac{\partial \dot{u}}{\partial u} & 0 & \frac{\partial \dot{u}}{\partial w} & 0 & -w_0 & 0 & 0 & -g\cos\theta_0 & 0 & 0 & 0 & 0 \\
0 & 0 & 0 & \frac{\partial \dot{v}}{\partial v} & 0 & \frac{\partial \dot{v}}{\partial p} & 0 & -u_0 & g\cos\theta_0 & 0 & 0 & 0 & 0 & 0 \\
\frac{\partial \dot{w}}{\partial n_1} & \frac{\partial \dot{w}}{\partial n_2} & \frac{\partial \dot{w}}{\partial u} & 0 & \frac{\partial \dot{w}}{\partial w} & 0 & u_0 & 0 & 0 & -g\sin\theta_0 & 0 & 0 & 0 & 0 \\
0 & 0 & 0 & \frac{\partial \dot{p}}{\partial v} & 0 & \frac{\partial \dot{p}}{\partial p} & 0 & \frac{\partial \dot{p}}{\partial r} & 0 & 0 & 0 & 0 & 0 & 0 \\
\frac{\partial \dot{q}}{\partial n_1} & \frac{\partial \dot{q}}{\partial n_2} & \frac{\partial \dot{q}}{\partial u} & 0 & \frac{\partial \dot{q}}{\partial w} & 0 & \frac{\partial \dot{q}}{\partial q} & 0 & 0 & \frac{\partial \dot{q}}{\partial \theta} & 0 & 0 & 0 & 0 \\
\frac{\partial \dot{r}}{\partial n_1} & \frac{\partial \dot{r}}{\partial n_2} & 0 & \frac{\partial \dot{r}}{\partial v} & 0 & \frac{\partial \dot{r}}{\partial p} & 0 & \frac{\partial \dot{r}}{\partial r} & 0 & 0 & 0 & 0 & 0 & 0 \\
0 & 0 & 0 & 0 & 0 & 1 & 0 & \tan\theta_0 & 0 & 0 & 0 & 0 & 0 & 0 \\
0 & 0 & 0 & 0 & 0 & 0 & 1 & 0 & 0 & 0 & 0 & 0 & 0 & 0 \\
0 & 0 & 0 & 0 & 0 & 0 & 0 & 1/\cos\theta_0 & 0 & 0 & 0 & 0 & 0 & 0 \\
0 & 0 & \cos\theta_0 & 0 & -\sin\theta_0 & 0 & 0 & 0 & 0 & 0 & 0 & 0 & 0 & 0 \\
0 & 0 & 0 & 1 & 0 & 0 & 0 & 0 & 0 & 0 & 0 & 0 & 0 & 0 \\
0 & 0 & \sin\theta_0 & 0 & \cos\theta_0 & 0 & 0 & 0 & 0 & 0 & 0 & 0 & 0 & 0
\end{bmatrix} \tag{3.10}$$

$$\mathbf{B}_L = \begin{bmatrix}
\frac{\partial \dot{n}_1}{\partial \tau_1} & 0 & 0 & 0 & 0 & 0 \\
0 & \frac{\partial \dot{n}_2}{\partial \tau_2} & 0 & 0 & 0 & 0 \\
0 & 0 & 0 & \frac{\partial \dot{u}}{\partial \delta_e} & 0 & \frac{\partial \dot{u}}{\partial \delta_e} \\
0 & 0 & 0 & 0 & \frac{\partial \dot{v}}{\partial \delta_r} & 0 \\
0 & 0 & 0 & \frac{\partial \dot{w}}{\partial \delta_e} & 0 & \frac{\partial \dot{w}}{\partial \delta_f} \\
\frac{\partial \dot{p}}{\partial \tau_1} & \frac{\partial \dot{p}}{\partial \tau_2} & \frac{\partial \dot{p}}{\partial \delta_a} & 0 & 0 & 0 \\
0 & 0 & 0 & \frac{\partial \dot{q}}{\partial \delta_e} & 0 & \frac{\partial \dot{q}}{\partial \delta_f} \\
0 & 0 & 0 & 0 & \frac{\partial \dot{r}}{\partial \delta_r} & 0 \\
0 & 0 & 0 & 0 & 0 & 0 \\
0 & 0 & 0 & 0 & 0 & 0 \\
0 & 0 & 0 & 0 & 0 & 0 \\
0 & 0 & 0 & 0 & 0 & 0 \\
0 & 0 & 0 & 0 & 0 & 0 \\
0 & 0 & 0 & 0 & 0 & 0
\end{bmatrix} \tag{3.11}$$

The Level operating mode requires the calculation of more parameters than the Hover operating mode. This set of parameters is listed in Table 3.2.

Parameter	Value	Units	Description
$\frac{\partial \dot{n}_{1,2}}{\partial n_{1,2}}$	-17.7306	s^{-1}	Stabilizing torque due to rotor friction.
$\frac{\partial \dot{n}_{1,2}}{\partial u}$	32.4560	$s^{-1}m^{-1}$	Propeller acceleration due to increased airspeed.
$\frac{\partial \dot{u}}{\partial n_{1,2}}$	0.0342	m/s	Longitudinal acceleration due to increased propeller rotation.
$\frac{\partial \dot{u}}{\partial u}$	-0.2530	s^{-1}	Longitudinal velocity damping.
$\frac{\partial \dot{u}}{\partial w}$	-0.7508	s^{-1}	Longitudinal velocity decceleration due to increased angle of attack.
$\frac{\partial \dot{v}}{\partial v}$	-0.3781	s^{-1}	Lateral velocity damping.
$\frac{\partial \dot{v}}{\partial p}$	1.9103	$ms^{-1}rad^{-1}$	Lateral velocity acceleration due to roll rotation.
$\frac{\partial \dot{w}}{\partial n_{1,2}}$	0.0048	ms^{-1}	Vertical velocity acceleration due to increased propeller rotation.
$\frac{\partial \dot{w}}{\partial u}$	-0.8916	s^{-1}	Vertical velocity acceleration due to increased forward velocity.
$\frac{\partial \dot{w}}{\partial w}$	-5.6191	s^{-1}	Vertical velocity damping.
$\frac{\partial \dot{p}}{\partial p}$, $\frac{\partial \dot{p}}{\partial v}$, $\frac{\partial \dot{p}}{\partial r}$	0	s^{-1}	Roll damping and roll acceleration due to lateral velocity and yawing motion, respectively.
$\frac{\partial \dot{q}}{\partial n_{1,2}}$	0.0693	$rad\,s^{-1}$	Pitch rate acceleration due to propeller rotation.
$\frac{\partial \dot{q}}{\partial u}$	0.2602	$rad\,s^{-1}m^{-1}$	Pitch rate acceleration due to forward velocity.
$\frac{\partial \dot{q}}{\partial w}$	-9.5274	$rad\,s^{-1}m^{-1}$	Pitch rate acceleration due to downward velocity.
$\frac{\partial \dot{q}}{\partial q}$	-11.7192	s^{-1}	Pitch damping.
$\frac{\partial \dot{q}}{\partial \theta}$	0	s^{-2}	Pitch rate acceleration due to pitch angle.
$\frac{\partial \dot{r}}{\partial n_{1,2}}$	$\mp$0.1161	rad/s	Increased propeller 1 rotation provides negative yawing moment while increased propeller 2 rotation provides positive yawing moment.
$\frac{\partial \dot{r}}{\partial v}$	-3.7777	$rad\,s^{-1}m^{-1}$	Yaw rate acceleration due to lateral velocity.
$\frac{\partial \dot{r}}{\partial r}$	-3.5064	s^{-1}	Yaw damping.
$\frac{\partial \dot{n}_{1,2}}{\partial \tau_{1,2}}$	15195	$N^{-1}m^{-1}s^{-2}$	Increased input torque increases propeller rotation.
$\frac{\partial \dot{u}}{\partial \delta_e}$	-0.4370	$ms^{-2}rad^{-1}$	Forward acceleration due to elevator deflection.
$\frac{\partial \dot{u}}{\partial \delta_f}$	-5.4010	$ms^{-2}rad^{-1}$	Forward acceleration due to flap deflection.
$\frac{\partial \dot{v}}{\partial \delta_r}$	4.8361	$ms^{-2}rad^{-1}$	Lateral acceleration due to rudder deflection.
$\frac{\partial \dot{w}}{\partial \delta_e}$	-14.2581	$ms^{-2}rad^{-1}$	Vertical acceleration due to elevator deflection.
$\frac{\partial \dot{w}}{\partial \delta_f}$	-52.3694	$ms^{-2}rad^{-1}$	Vertical acceleration due to flap deflection.
$\frac{\partial \dot{p}}{\partial \tau_{1,2}}$	$\mp$20.8333	$rad\,s^{-2}N^{-1}m^{-1}$	Rolling moment due to differential propeller acceleration.
$\frac{\partial \dot{p}}{\partial \delta_a}$	-486.4866	s^{-2}	Roll acceleration due to aileron deflection.
$\frac{\partial \dot{q}}{\partial \delta_e}$	-204.6042	s^{-2}	Pitch acceleration due to elevator deflection.
$\frac{\partial \dot{q}}{\partial \delta_f}$	40.7063	s^{-2}	Pitch acceleration due to flap deflection.
$\frac{\partial \dot{r}}{\partial \delta_r}$	-48.3175	s^{-2}	Yaw acceleration due to rudder deflection.

Table 3.2: Level linear model parameters.

It is possible to identify the aircraft modes discussed in Section 3.2 by the analysis of matrix $\mathbf{A}_L$ eigenvalues $\boldsymbol{\lambda}_L$ which are plotted on the complex plane in Figure 3.2.

$$\boldsymbol{\lambda}_L = \begin{bmatrix} 0 \\ 0 \\ 0 \\ 0 \\ -8.6764 + 9.6698i \\ -8.6764 - 9.6698i \\ -17.8711 \\ -0.0491 + 0.7864i \\ -0.0491 - 0.7864i \\ -17.7306 \\ -2.0174 + 6.2281i \\ -2.0174 - 6.2281i \\ 0 \\ 0,1501 \end{bmatrix} \tag{3.12}$$

Level flight eigenvalues for the operating mode under consideration can be sorted into the aircraft

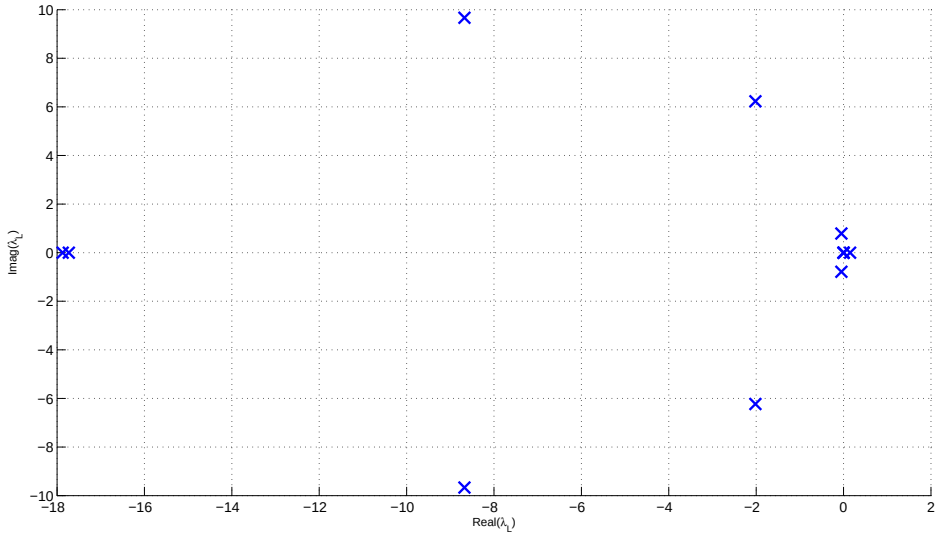

Figure 3.2: Level operating point pole map.

dynamic modes introduced in Section 3.2 decomposing the full matrix into lateral and longitudinal sub-matrices. This requires, however, the forward velocity influence in the propellers' dynamics to be neglected. Under this assumption the newly computed matrix eigenvalues do not change significantly which reiterates the validity of the approximation. Table 3.3 summarizes the result of this analysis.

Despite the Roll dynamic mode which is marginally stable unlike the most common aircrafts every other dynamic mode has very acceptable values for each dynamic mode, i.e. Phugoid, Short-Period and Dutch Roll are oscillatory being the Phugoid slightly damped and the Spiral mode is unstable.

Eigenvalues	**Damping Coefficient (ζ)**	**Natural Frequency (ω_n)**	**Aircraft Mode**
$-8.7 \pm 9,7i$	0.668	13.0 rad/s	Short-Period
$-0.049 \pm 0.79i$	0.062	0.79 rad/s	Phugoid
$-2.0 \pm 6.2i$	0.31	6.55 rad/s	Dutch Roll
0.15	-	-	Spiral
0	-	-	Roll

Table 3.3: Level Flight Eigenvalues categorization according to usual aircraft dynamic modes

3.2.3 Transition

The transition flight does not have an equilibrium point in the same sense as level flight and hover but linearization around some equilibrium point is required in order to obtain the Transition controller explained in Section 3.4.2. The chosen operating point given in (3.13) is very similar to the Hover operating point. However, its forward velocity of 1 m/s provides the linear model with characteristics which are present both in hover and level flight.

$$\begin{aligned} \boldsymbol{\xi}_{X_0} &\simeq [157.3 \quad 157.3 \quad 1 \quad 0 \quad 0 \quad 0 \quad 0 \quad 0 \quad 0 \quad \pi/2 \quad 0 \quad 0 \quad 0 \quad -1]^T \\ \boldsymbol{\mu}_{X_0} &\simeq [0.12 \quad 0.12 \quad 0 \quad 0 \quad 0 \quad 0]^T \end{aligned} \tag{3.13}$$

Matrices $\mathbf{A}_X$ and $\mathbf{B}_X$ in (3.14) and (3.15) provide relevant information about the system at the operating point in (3.13).

$$\mathbf{A}_X = \begin{bmatrix} \frac{\partial \dot{n}_1}{\partial n_1} & 0 & \frac{\partial \dot{n}_1}{\partial u} & 0 & 0 & 0 & 0 & 0 & 0 & 0 & 0 & 0 & 0 & 0 \\ 0 & \frac{\partial \dot{n}_2}{\partial n_2} & \frac{\partial \dot{n}_2}{\partial u} & 0 & 0 & 0 & 0 & 0 & 0 & 0 & 0 & 0 & 0 & 0 \\ \frac{\partial \dot{u}}{\partial n_1} & \frac{\partial \dot{u}}{\partial n_1} & \frac{\partial \dot{u}}{\partial u} & 0 & 0 & 0 & 0 & 0 & 0 & 0 & 0 & 0 & 0 & 0 \\ 0 & 0 & 0 & \frac{\partial \dot{v}}{\partial v} & 0 & 0 & 0 & -u_0 & 0 & 0 & -g & 0 & 0 & 0 \\ 0 & 0 & 0 & 0 & \frac{\partial \dot{w}}{\partial w} & 0 & u_0 & 0 & 0 & -g & 0 & 0 & 0 & 0 \\ 0 & 0 & 0 & 0 & 0 & \frac{\partial \dot{p}}{\partial p} & 0 & 0 & 0 & 0 & 0 & 0 & 0 & 0 \\ 0 & 0 & 0 & 0 & \frac{\partial \dot{q}}{\partial w} & 0 & \frac{\partial \dot{q}}{\partial q} & 0 & 0 & 0 & 0 & 0 & 0 & 0 \\ \frac{\partial \dot{r}}{\partial n_1} & \frac{\partial \dot{r}}{\partial n_2} & 0 & \frac{\partial \dot{r}}{\partial v} & 0 & 0 & 0 & \frac{\partial \dot{r}}{\partial r} & 0 & 0 & 0 & 0 & 0 & 0 \\ 0 & 0 & 0 & 0 & 0 & 1 & 0 & 0 & 0 & 0 & 0 & 0 & 0 & 0 \\ 0 & 0 & 0 & 0 & 0 & 0 & 1 & 0 & 0 & 0 & 0 & 0 & 0 & 0 \\ 0 & 0 & 0 & 0 & 0 & 0 & 0 & 1 & 0 & 0 & 0 & 0 & 0 & 0 \\ 0 & 0 & 0 & 0 & 1 & 0 & 0 & 0 & 0 & 0 & 0 & 0 & 0 & 0 \\ 0 & 0 & 0 & 1 & 0 & 0 & 0 & 0 & 0 & 0 & 0 & 0 & 0 & 0 \\ 0 & 0 & -1 & 0 & 0 & 0 & 0 & 0 & 0 & 0 & 0 & 0 & 0 & 0 \end{bmatrix} \tag{3.14}$$

$$\mathbf{B}_X = \begin{bmatrix} \frac{\partial \dot{n}_1}{\partial \tau_1} & 0 & 0 & 0 & 0 & 0 \\ 0 & \frac{\partial \dot{n}_2}{\partial \tau_2} & 0 & 0 & 0 & 0 \\ 0 & 0 & 0 & \frac{\partial \dot{u}}{\partial \delta_e} & 0 & \frac{\partial \dot{u}}{\partial \delta_e} \\ 0 & 0 & 0 & 0 & \frac{\partial \dot{v}}{\partial \delta_r} & 0 \\ 0 & 0 & 0 & \frac{\partial \dot{w}}{\partial \delta_e} & 0 & \frac{\partial \dot{w}}{\partial \delta_f} \\ \frac{\partial \dot{p}}{\partial \tau_1} & \frac{\partial \dot{p}}{\partial \tau_2} & \frac{\partial \dot{p}}{\partial \delta_a} & 0 & 0 & 0 \\ 0 & 0 & 0 & \frac{\partial \dot{q}}{\partial \delta_e} & 0 & \frac{\partial \dot{q}}{\partial \delta_f} \\ 0 & 0 & 0 & 0 & \frac{\partial \dot{r}}{\partial \delta_r} & 0 \\ 0 & 0 & 0 & 0 & 0 & 0 \\ 0 & 0 & 0 & 0 & 0 & 0 \\ 0 & 0 & 0 & 0 & 0 & 0 \\ 0 & 0 & 0 & 0 & 0 & 0 \\ 0 & 0 & 0 & 0 & 0 & 0 \\ 0 & 0 & 0 & 0 & 0 & 0 \end{bmatrix} \tag{3.15}$$

It is noticeable from the matrices' analysis that system slightly resembles that of Hover. The system eigenvalues ($\boldsymbol{\lambda}_X$) are computed after substituting the values in Table 3.4 into the matrices $\mathbf{A}_X$ and $\mathbf{B}_X$ and presented in (3.16) and depicted in Figure 3.3.

$$\boldsymbol{\lambda}_X = \begin{bmatrix} 0 \\ 0 \\ 0 \\ 0 \\ -1.6586 + 0.9320i \\ -1.6586 - 0.9320i \\ -25.1476 \\ -25.1323 \\ 0.9596 \\ -0.3096 \\ -8.4646 \\ -1.4879 \\ 0.7063 \\ 0 \end{bmatrix} \tag{3.16}$$

3.3 Reference Trajectories

The reference transition trajectories were generated with some intuitive insight about the system and considering that the transition is to occur in the vertical plane, i.e. the aircraft is laterally stabilized. Therefore, the triplet (u^*, w^*, θ^*) fully defines the aircraft state at any given point. It is desirable that the reference trajectories do not lead the aircraft to a stall situation as it can be hazardous.

Parameter	Value	Units	Description
$\frac{\partial \dot{n}_{1,2}}{\partial n_{1,2}}$	-25.1323	s^{-1}	Stabilizing torque due to rotor friction.
$\frac{\partial \dot{n}_{1,2}}{\partial u}$	2.9958	$s^{-1}m^{-1}$	Propeller acceleration due to increased airspeed.
$\frac{\partial \dot{u}}{\partial n_{1,2}}$	0.0634	m/s	Longitudinal acceleration due to increased propeller rotation.
$\frac{\partial \dot{u}}{\partial u}$	-0.3249	s^{-1}	Longitudinal velocity damping.
$\frac{\partial \dot{v}}{\partial v}$	-0.0354	s^{-1}	Lateral velocity damping.
$\frac{\partial \dot{w}}{\partial w}$	-0.5348	s^{-1}	Vertical velocity damping.
$\frac{\partial \dot{p}}{\partial p}$	0	s^{-1}	Roll damping.
$\frac{\partial \dot{q}}{\partial w}$	-0.9067	rad $s^{-1}m^{-1}$	Pitch rate acceleration due to downward velocity.
$\frac{\partial \dot{q}}{\partial q}$	-8.7115	s^{-1}	Pitch damping.
$\frac{\partial \dot{r}}{\partial n_{1,2}}$	$\mp$0.2143	rad/s	Increased propeller 1 rotation provides negative yawing moment while increased propeller 2 rotation provides positive yawing moment.
$\frac{\partial \dot{r}}{\partial v}$	-0.3541	rad $s^{-1}m^{-1}$	Yaw rate acceleration due to lateral velocity.
$\frac{\partial \dot{r}}{\partial r}$	-2.3221	s^{-1}	Yaw damping.
$\frac{\partial \dot{n}_{1,2}}{\partial \tau_{1,2}}$	15195	$N^{-1}m^{-1}s^{-2}$	Increased input torque increases propeller rotation.
$\frac{\partial \dot{v}}{\partial \delta_r}$	2.6064	$ms^{-2}rad^{-1}$	Lateral acceleration due to rudder deflection.
$\frac{\partial \dot{w}}{\partial \delta_e}$	-15.2785	$ms^{-2}rad^{-1}$	Vertical acceleration due to elevator deflection.
$\frac{\partial \dot{w}}{\partial \delta_f}$	-58.0843	$ms^{-2}rad^{-1}$	Vertical acceleration due to flap deflection.
$\frac{\partial \dot{p}}{\partial \tau_{1,2}}$	$\mp$20.8333	rad $s^{-2}N^{-1}m^{-1}$	Rolling moment due to differential propeller acceleration.
$\frac{\partial \dot{p}}{\partial \delta_a}$	-402.6001	s^{-2}	Roll acceleration due to aileron deflection.
$\frac{\partial \dot{q}}{\partial \delta_e}$	-219.2470	s^{-2}	Pitch acceleration due to elevator deflection.
$\frac{\partial \dot{q}}{\partial \delta_f}$	45.1484	s^{-2}	Pitch acceleration due to flap deflection.
$\frac{\partial \dot{r}}{\partial \delta_r}$	-26.0403	s^{-2}	Yaw acceleration due to rudder deflection.

Table 3.4: Transition linear model parameters.

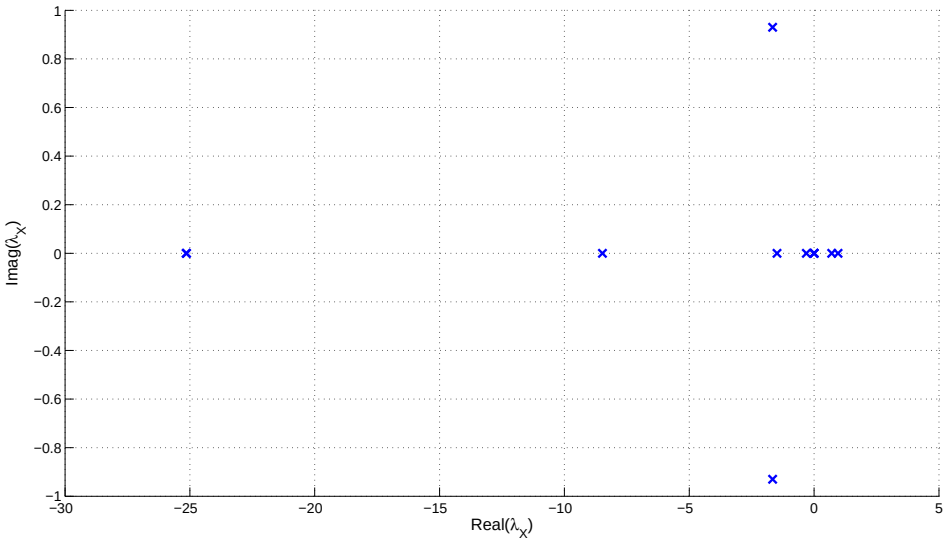

Figure 3.3: Transition operating point pole map.

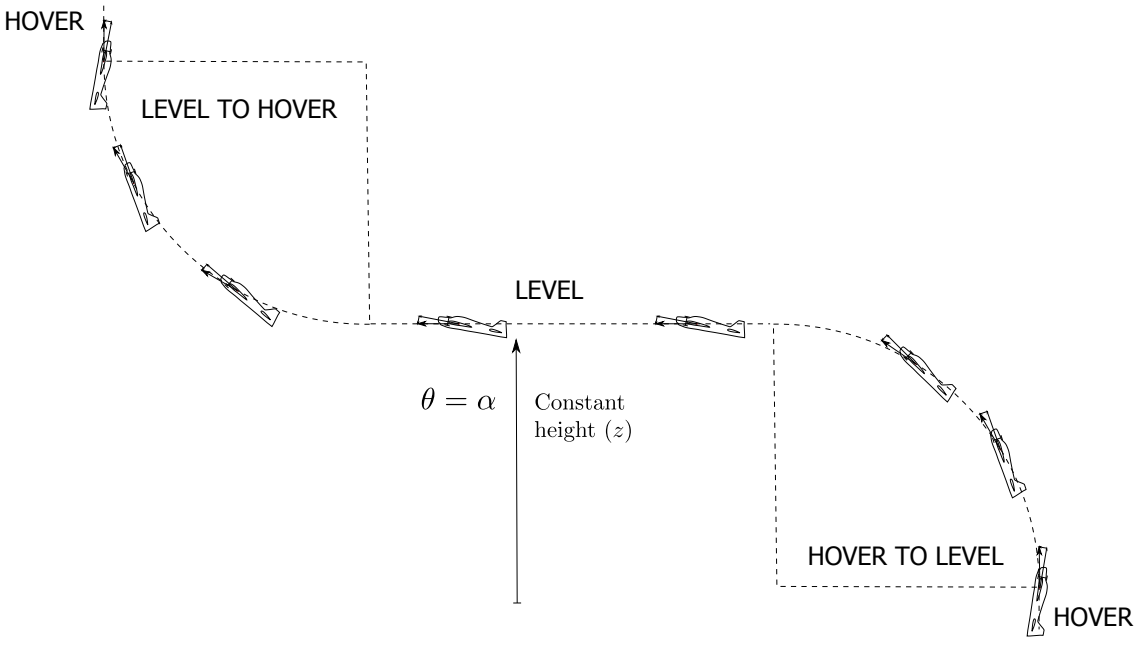

Figure 3.4: Transition trajectories concept.

3.3.1 Hover to Level Flight

Considering that the aircraft is able to climb up at a speed equal to that of Level Flight then the change in pitch angle is not troublesome, requiring solely the change of the main lifting force from thrust to wing lift. Under this assumption, the trajectories become very simple as the transition can be achieved with a step in the forward velocity u and a step in the pitch rate q. A ramp which takes the downward velocity w from the equilibrium value in Hover to the equilibrium in Level Flight is considered instead of a step input in order to prevent stall. These trajectories are depicted in Figure 3.5.

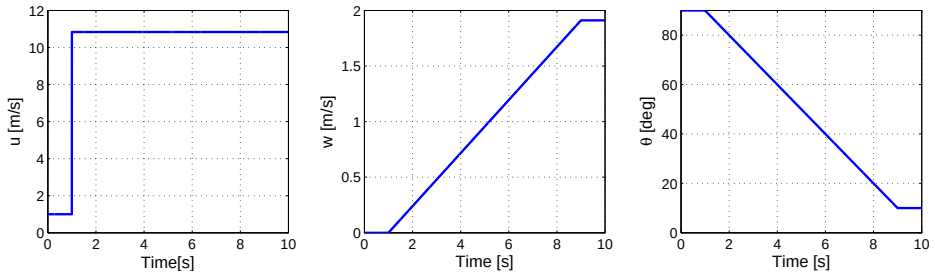

Figure 3.5: Hover to Level Flight reference forward velocity $u(t)$, downward velocity $w(t)$ and pitch angle $\theta(t)$.

3.3.2 Level Flight to Hover

The same assumption which was made in order to build the Hover to Level Flight transition is used to build the reference trajectories that will enable the transition from Level Flight to Hover, i.e. the aircraft is able to climb up at a speed equal to that of Level Flight. The aircraft begins its change in pitch angle and only near hover it decelerates to null speed. Similarly to the trajectories presented in the previous section, a ramp reference input is considered for the downward velocity in order to prevent stall. The reference trajectories for this maneuver are presented in Figure 3.6.

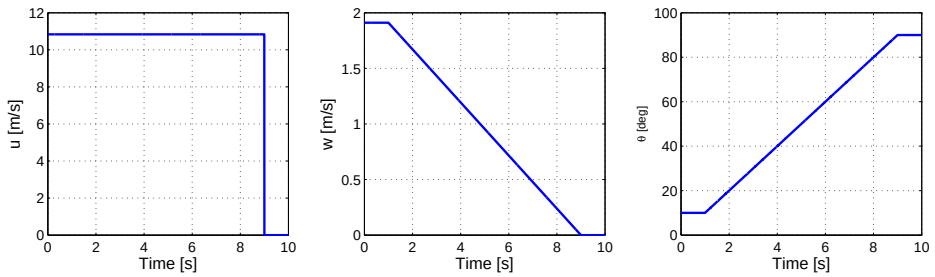

Figure 3.6: Level Flight to Hover reference forward velocity $u(t)$, downward velocity $w(t)$ and pitch angle $\theta(t)$.

The step inputs may cause the actuators to saturate due to their large magnitude. The controller structure which is explained in section 3.4.1 avoids saturation problems.

3.4 Controller Synthesis

The LQR is an optimal control solution in the sense that it minimizes the cost function (3.2) which is highly dependent on the fully customizable matrix pair $(\mathbf{Q}, \mathbf{R})$. Closed loop dynamic properties are bound to change radically with different matrix values. This issue is carefully studied in Section 3.4.2.

Actuator saturation is a part of the system which the LQR control alone is not able to handle therefore D-methodology will be used as explained in Section 3.4.1.

3.4.1 Controller Structure: D-methodology

The control law employed in a Linear Quadratic Regulator Problem is given in (3.3) and it requires full state feedback. However, the feedback states are not necessarily equal to the system state $\boldsymbol{\xi}$ but rather the state $\boldsymbol{\xi}_H$, $\boldsymbol{\xi}_X$ or $\boldsymbol{\xi}_L$ depending on the current Operating Mode. These states do not include all the variables in $\boldsymbol{\xi}$ and moreover they may include several integrator states from a selected range of variables $\bar{\boldsymbol{\xi}}$. This control structure is depicted in Figure 3.7.

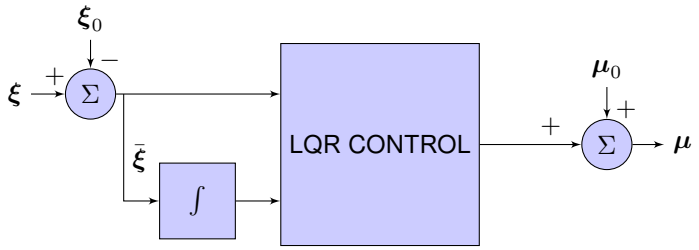

Figure 3.7: LQR Control Structure.

This controller structure requires absolute knowledge of the equilibrium point $(\boldsymbol{\xi}_0, \boldsymbol{\mu}_0)$ which is seldom known. A much more versatile controller structure is provided by the D-methodology depicted in Figure 3.8.

The D-methodology has several benefits over the classic structure depicted in Figure 3.7:

- It does not require the equilibrium point to be known;
- Controller gains changes due to mode switching do not instantaneously change the actuator input;

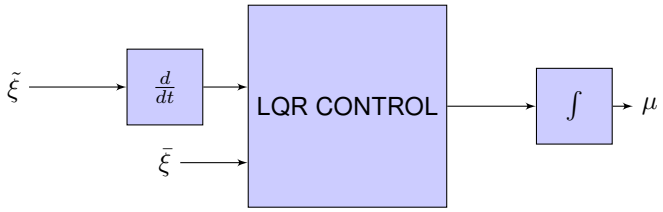

Figure 3.8: D-methodology control structure.

- It provides anti-windup to the control if integrator output saturates whenever the actuators limits are reached.

D-methodology controller structure is chosen due to its obvious advantages.

3.4.2 State and Input Weighting

The state and input weighting done by the matrices $\mathbf{Q}$ and $\mathbf{R}$ is performed in a trial and error basis, making use of Bryson's method [25] to come up with an initial weighting. This method builds diagonal matrices whose elements are the inverse of the maximum deviation expected for a given state/input variable squared as in (3.17) and (3.18). The new states and control dimensioning are fully described in sections that follow.

$$\mathbf{Q} = \begin{bmatrix} \boldsymbol{\xi}_{1_{max}}^{-2} & 0 & \dots & 0 \\ 0 & \boldsymbol{\xi}_{2_{max}}^{-2} & & 0 \\ \vdots & & \ddots & \vdots \\ 0 & 0 & \dots & \boldsymbol{\xi}_{n_{max}}^{-2} \end{bmatrix} \tag{3.17}$$

$$\mathbf{R} = \begin{bmatrix} \boldsymbol{\mu}_{1_{max}}^{-2} & 0 & \dots & 0 \\ 0 & \boldsymbol{\mu}_{2_{max}}^{-2} & & 0 \\ \vdots & & \ddots & \vdots \\ 0 & 0 & \dots & \boldsymbol{\mu}_{m_{max}}^{-2} \end{bmatrix} \tag{3.18}$$

The LQR weighting is different for each operating mode (Hover, Transition, Level) because each of these modes has different goals and objectives but the maximum deviation of each integrator state in matrices $\mathbf{Q}$ and $\mathbf{R}$ is ten times lower than the original state. This policy allows faster reference tracking as the position has always a larger penalty than the velocity, otherwise the velocity would be very rapidly brought close to zero while the position error remained large.

Hover

During Hover the control law is modified to fit the structure depicted in Figure 3.8 with

$$\begin{aligned}\tilde{\boldsymbol{\xi}}_H &= [n_1 \quad n_2 \quad u-u^*(t) \quad v \quad w-w^*(t) \quad p \quad q-q^*(t) \quad r \quad \phi \quad \theta-\theta^*(t) \quad \psi]^T \\ \bar{\boldsymbol{\xi}}_H &= [u-u^*(t) \quad v \quad w-w^*(t) \quad \phi \quad \theta-\theta^* \quad \psi]^T.\end{aligned} \tag{3.19}$$

Several features which result from this choice are:

- The trajectory $[x\ y\ z]^T$ is not included in the control for the transition control is performed with $u^*(t)$, $w^*(t)$ and $\theta^*(t)$ reference tracking;
- The integrator states in u, v and w ensure position stabilization;
- Integrator states in ϕ, θ and ψ ensure angular position stabilization;
- The system is still controllable through $\mathbf{B}_H$ despite additional states have been added.

The considered maximum deviations from equilibrium state which are applied in Bryson's method are listed in Table 3.5.

Variable	Maximum Deviation	Observations
$n_{1,2}$	200 rps	Propeller speed should be allowed to span a large velocity range because it provides both thrust control and yaw control.
u	10 m/s	Forward velocity tracking is loosened when compared to either downward velocity and lateral velocity because it is considered that the aircraft remains in Hover despite its forward velocity.
v,w	1 m/s	Lateral velocity and downward velocity should be more accurately tracked in order to prevent the aircraft from leaving Hover operating mode.
p,r	1 rad/s	Roll rate and yaw rate are loosened tracked.
q	0.1 rad/s	Pitch rate is more closely tracked for better transition performance.
$\tau_{1,2}$	τ_{max} N.m	Maximum rotor input torque is considered.
δ_a, δ_f	7.5 deg	Maximum allowable aileron and flap deflections are considered.
δ_e, δ_r	15 deg	Maximum allowable elevator and rudder deflections are considered.

Table 3.5: Maximum state and input deviations from equilibrium for $\mathbf{Q}_H$ and $\mathbf{R}_H$ matrix weighting.

Transition

The Transition Operating Mode control must allow close reference tracking and provide a stable flight during the maneuver. Linear models require linearization around some equilibrium point and do not depict the aircraft behavior throughout the maneuver. Figure 3.9 depicts the change in system poles which occurs during the transition from hover to level flight. Some features present in this pole map are:

- There is a large reduction in propeller damping which is identified by two leftmost poles;
- The phugoid dynamic mode is unstable at the maneuver start but becomes stable with increasing forward velocity;
- Spiral dynamic mode is always unstable;

The previous analysis is also valid for the transition from level flight to hover because the two maneuvers are identical. The Transition operating mode must provide stabilization for the full flight envelope,

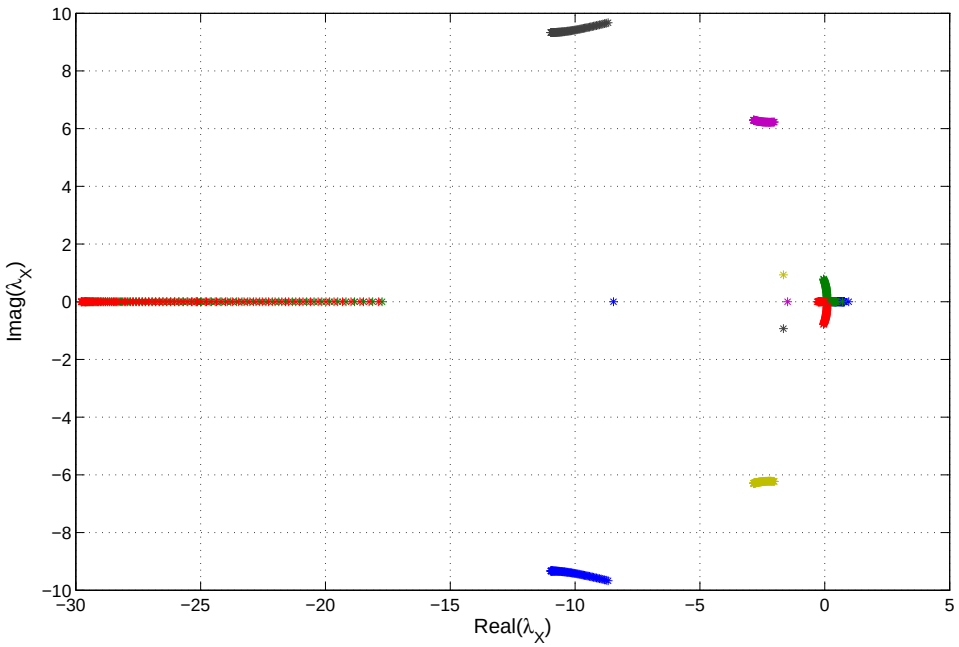

Figure 3.9: Operating points spanned during transition.

i.e. changes in aircraft dynamic modes during the maneuver must not render the aircraft unstable.

The trajectory tracking requires strict lateral stabilization for the transition to take place in the vertical plane or with as little deviation as possible. These requirements imply the need for integrators in the

variables $\tilde{u}$, v, $\tilde{w}$, ϕ, $\tilde{\theta}$ and ψ. The controller structure depicted in Figure 3.8 is used with

$$\begin{aligned}\tilde{\boldsymbol{\xi}} &= [n_1 \quad n_2 \quad u-u^*(t) \quad v \quad w-w^*(t) \quad p \quad q-q^*(t) \quad r \quad \phi \quad \theta-\theta^*(t) \quad \psi]^T \\ \bar{\boldsymbol{\xi}}_H &= [u-u^*(t) \quad v \quad w-w^*(t) \quad \phi \quad \theta-\theta^*(t) \quad \psi]^T.\end{aligned} \tag{3.20}$$

Several remarks can be made for this particular choice of state variables and integrator states:

- The system is still controllable through $\mathbf{B}_X$ despite having additional states;
- The trajectory $[x\ y\ z]^T$ is not included in the control loop;
- The integrators in v, ψ and ϕ ensure that the transition flight is executed in the vertical plane;
- The integrators in $\tilde{u}$, $\tilde{w}$ and $\tilde{\theta}$ ensure reference trajectory tracking.

The weights provided in Table 3.6 are used in the LQR algorithm which computes the feedback gain $\mathbf{K}_X$. This feedback gain not only stabilizes the aircraft near the equilibrium point but also in all the operating points spanned by the transition maneuver. The pole changes which occur during the transition are depicted in Figure 3.10 which prove that stability is always guaranteed.

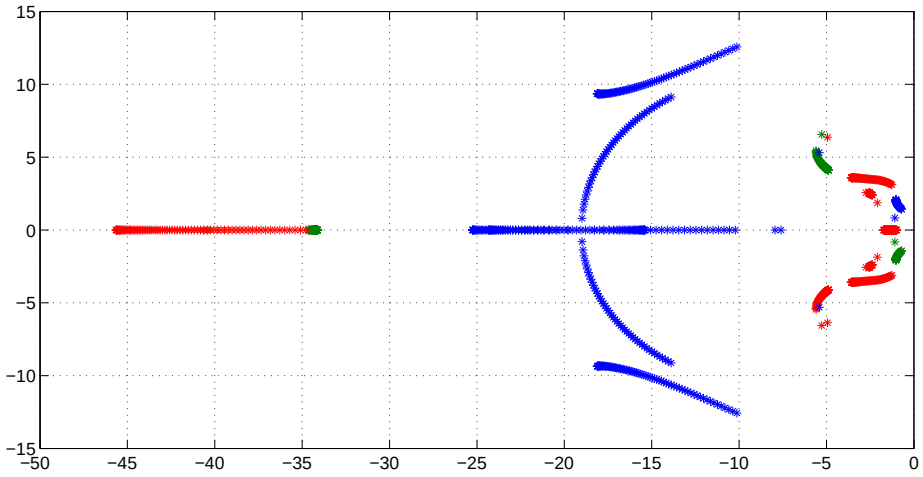

Figure 3.10: Controlled Transition system poles.

Level Flight

The objective when in the level flight mode is to keep the path at a constant height to the ground, therefore introducing the z state and integrators on the $\tilde{u}$, v, ϕ, $\tilde{\theta}$ and ψ variables. This strategy leads to the controller structure depicted in Figure 3.8 with

$$\begin{aligned}\tilde{\boldsymbol{\xi}} &= [n_1 \quad n_2 \quad u-u^*(t) \quad v \quad w \quad p \quad q-q^*(t) \quad r \quad \phi \quad \theta-\theta^*(t) \quad \psi \quad z]^T \\ \bar{\boldsymbol{\xi}}_H &= [u-u^*(t) \quad v \quad \phi \quad \theta-\theta^*(t) \quad \psi]^T.\end{aligned} \tag{3.21}$$

Similarly to Hover and Transition operating modes:

- The system is controllable through $\mathbf{B}_L$;
- The integrator state in $\tilde{w}$ was replaced by the state variable z which guarantees that the aircraft keeps a constant height to ground;

Table 3.7 lists the maximum expected deviations from equilibrium which are used in Bryson's method.

3.4.3 Controller Robustness

The controllers' $\boldsymbol{\mu}_H$, $\boldsymbol{\mu}_X$ and $\boldsymbol{\mu}_L$ robustness is tested against parameters change with respect to nominal values without changing the controllers' gains $\mathbf{K}_H$, $\mathbf{K}_X$ and $\mathbf{K}_L$. Due to the immense number of parameters which characterize the system, the forthcoming analysis focuses on a restricted set of these parameters which have more uncertainty. This particular choice includes every aerodynamic coefficient and aircraft Moments of Inertia. Furthermore, collective changes in parameters are considered, i.e. no parameter is analyzed alone thus preventing the escalating number of analyzed it would take to perform a full robustness test.

Figure 3.11 depicts the *root locus* for each Operating Mode given a change of $\pm 20\%$ in the model parameters. Despite altering the system dynamics, this change does not render the system unstable. The most prominent and hazardous change is that of the dominant pole which is seen to slide along the real axis towards the right hand plane in Hover and Transition operating modes causing slower responses to disturbances and input controls. These slower dynamics appear mainly due to a reduction in $C_{L_{\delta_{r_{vs}}}}$ and $C_{L_{\delta_{r_{p,vs}}}}$ which correspond to a reduction in lateral maneuverability which is not pronounced in level flight.

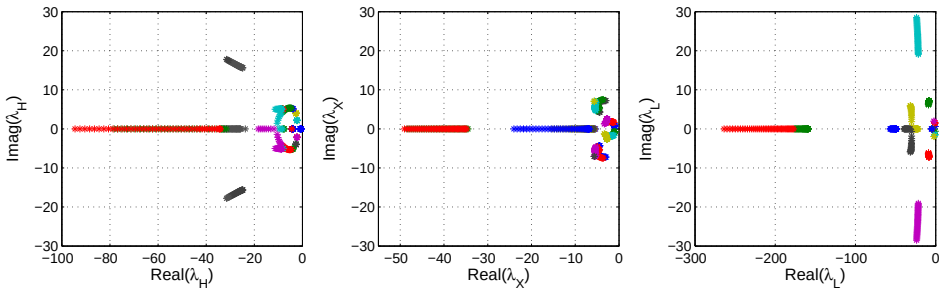

Figure 3.11: Controller robustness - the three *root locus* depict system poles with $\pm$20% change in parameters for Hover, Transition and Level Flight Operating Modes.

Variable	Maximum Deviation	Observations
$n_{1,2}$	200 rps	Propeller speed should be allowed to span a large velocity range because it provides both thrust control and yaw control.
u,v,w	10 m/s	Velocity tracking is loosened when compared with Hover.
p,q,r	1 rad/s	Angular velocity is more loosely tracked than in Hover.
$\tau_{1,2}$	τ_{max} N.m	Maximum rotor input torque is considered.
δ_a, δ_f	7.5 deg	Maximum allowable aileron and flap deflections are considered.
δ_e	15 deg	Maximum allowable elevator and rudder deflections are considered.
δ_r	45 deg	Maximum variation was increased above the maximum allowable rudder deflection in order to allow faster lateral stabilization. Saturation problems are avoided when using D-methodology.

Table 3.6: Maximum state and input deviations from equilibrium for $\mathbf{Q}_X$ and $\mathbf{R}_X$ matrix weighting.

Variable	Maximum Deviation	Observations
$n_{1,2}$	200 rps	Propeller speed should be allowed to span a large velocity range because it provides both thrust control and yaw control.
u	10 m/s	Forward velocity tracking is loosened when compared to either downward velocity and lateral velocity.
v,w	1 m/s	Lateral velocity and downward velocity should be more accurately tracked in order to prevent the aircraft from leaving Level operating mode.
p,r	1 rad/s	Roll rate and yaw rate are loosely tracked.
q	0.1 rad/s	Pitch rate is more closely tracked.
$\tau_{1,2}$	τ_{max} N.m	Maximum rotor input torque is considered.
δ_a, δ_f	7.5 deg	Maximum allowable aileron and flap deflections are considered.
δ_e, δ_r	15 deg	Maximum allowable elevator and rudder deflections are considered.

Table 3.7: Maximum state and input deviations from equilibrium for $\mathbf{Q}_L$ and $\mathbf{R}_L$ matrix weighting.

3.5 Simulation Results

Simulations were run in order to test the controllers' reliability in each one of the operating modes. Sections 3.5.1, 3.5.2, 3.5.3 and 3.5.4 present some simulation results in Hover, Level and Transition, respectively.

Throughout Sections 3.5.3 and 3.5.4 special emphasis is given to the aircraft's longitudinal variables $[u\ w\ q\ \theta\ x\ z]$ for the transition is to occur in the vertical plane. The variables which characterize the lateral behavior should always be zero.

3.5.1 Hover

Hover control simulations demonstrate the controller's ability to stabilize the aircraft at the operating point (3.5) starting from any initial condition which lies within Hover domain, $\boldsymbol{\xi}(0) \in \mathcal{D}(H)$, namely with initial conditions $\psi(0) = \bar{\psi}_H$ and $\theta(0) = \bar{\theta}_H$. Simulations results with the aforementioned starting angular values are depicted in Figure 3.12.

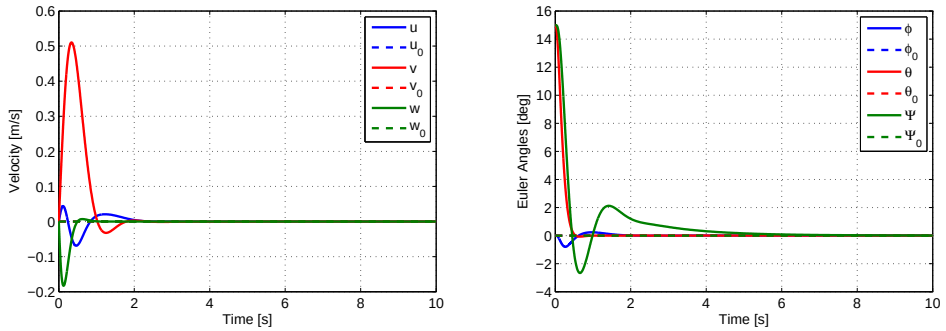

Figure 3.12: Hover simulation - Velocity and Euler Angles time evolution.

3.5.2 Level

Level flight control must stabilize the aircraft at the equilibrium point in equation (3.9) as long as its initial state lies within the Level Flight domain, $\boldsymbol{\xi}(0) \in \mathcal{D}(L)$, namely with initial angles $\phi(0) = \bar{\phi}_L$ and $\theta(0) = \bar{\theta}_L$. Simulations results with the aforementioned starting angular values are depicted in Figure 3.13.

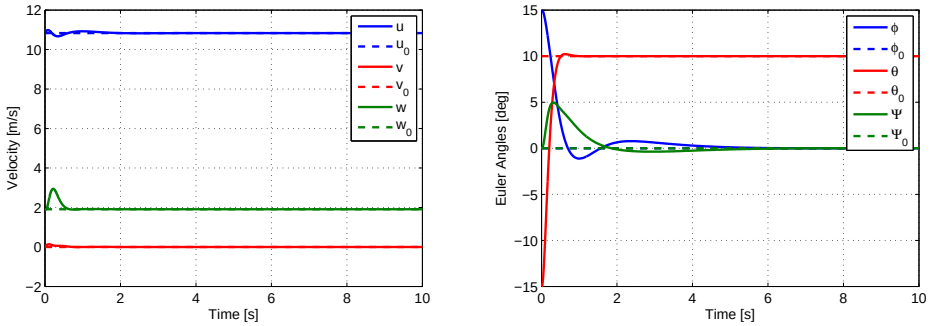

Figure 3.13: Level Flight simulation - Velocity and Euler Angles time evolution.

3.5.3 Transition: Hover to Level

The Aircraft starts its transition to Level Flight in Hover configuration and since the reference transition trajectory starts at $u = 1\ m/s$ a step input with the same magnitude is required when in Hover. The system's behavior is represented in Figure 3.14 for this particular case. The aircraft starts in Hover, switches to Transition Flight at time $t = 0.9$ s when the aircraft state enters the Guard Map $\mathcal{D}(H, X)$ and switches to Level Flight at $t = 9.6$ s when the Guard Map $\mathcal{D}(X, L)$ is breached. Nonlinear behavior is highly noticeable during switching from Hover to Transition flight due to input torque saturation. Figure 3.15 depicts the tracking errors which arise during the transition maneuver. The velocity tracking is more loosened than the pitch angle tracking whose error is always below 1°. It can also be noticed the erratic behavior in $w^*(t)$ tracking due to the very simple reference trajectories which are somewhat far from the model dynamics.

Figure 3.16 depicts the aircraft's trajectory during the transition which is seen to maintain the desired constant height when Level Flight Operating Mode is reached.

3.5.4 Transition: Level to Hover

In the simulation results presented in this section, the aircraft switches from Level to Transition operating mode at $t = 0$ s because the initial state lies within the Guard Map $\mathcal{G}(L, X)$. The switch to Hover Operating mode occurs at $t = 7.7$ s when the aircraft state enters the Guard Map $\mathcal{G}(X, H)$.

Figure 3.17 depicts the forward velocity flow which is seen to deviate slightly from the reference value when the pitch angle starts to increase and has nonlinear behavior when the switch to Hover is performed due to actuator saturation. Figure 3.18 depicts trajectory tracking errors which complement the information given in Figure 3.17. The highest errors during the transition do not occur during transition tracking but rather during operating mode switching. Yet again it is noticeable higher errors in velocity tracking than in pitch angle tracking which is a desirable feature since slight deviations in the pitch

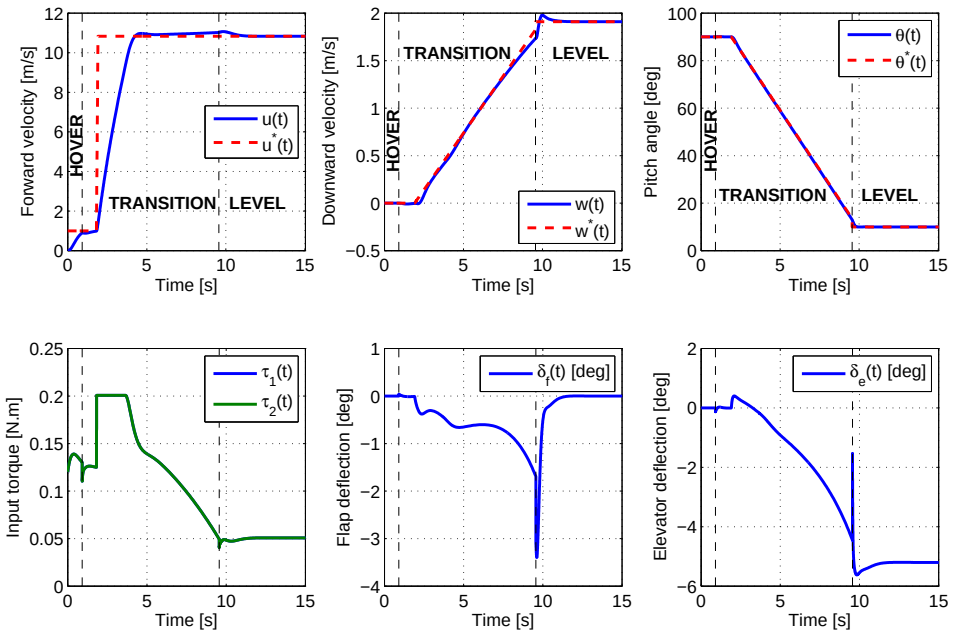

Figure 3.14: Transition from Hover to Level Flight simulation. The upper row depicts the forward velocity u, the downward velocity w and the pitch angle θ flow in time (blue line) and the references (red dashed line). The second row depicts the actuators' flow which have the highest influence on the variable portraited directly above.

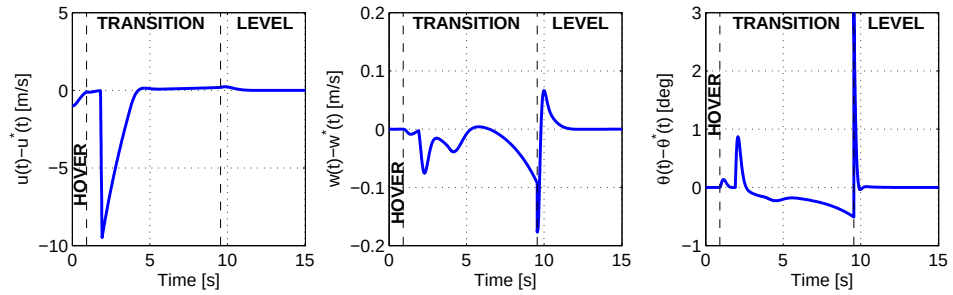

Figure 3.15: Transition from Hover to Level Flight simulation tracking errors.

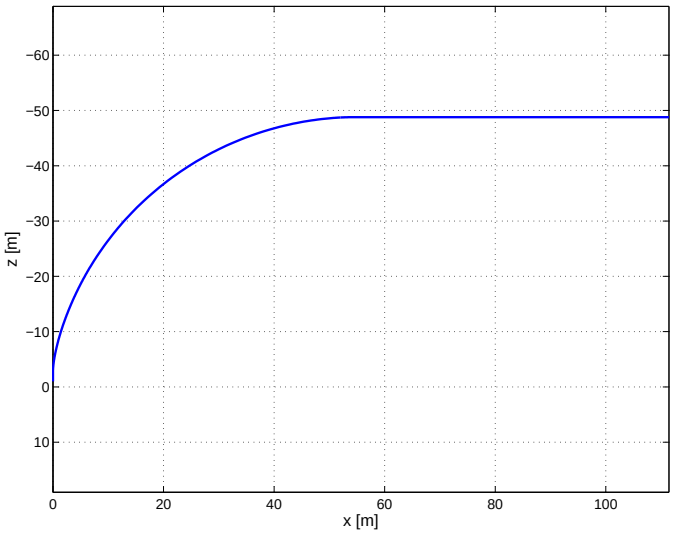

Figure 3.16: Aircraft vertical trajectory.

angle are more disturbing than deviations in the vehicle's velocity.

Figure 3.19 depicts the aircraft trajectory during the transition from Level Flight to Hover where it is possible to verify that the UAV does not collide with ground.

3.6 Summary

This chapter introduced the Linear Quadratic Regulator as a possible solution for hover and level flights stabilization as well as reference tracking. The aircraft linear model was obtained for three different operating points which correspond to the three operating modes defined by the hybrid automaton. The local system behavior was analyzed by the inspection of its eigenvalues, revealing that:

- The hover flight linear model is very simple depicting a slight damping in the $n_{1,2}$, u, p and r state variables;
- The level flight linear model is mainly affected by two slow modes: a slightly damped phugoid mode and an unstable spiral mode;
- The Transition operating point is similar to that of Hover but with an ascending velocity of $u = 1$ m/s, which provides the linear model with characteristics that are present in both hover and level flights.

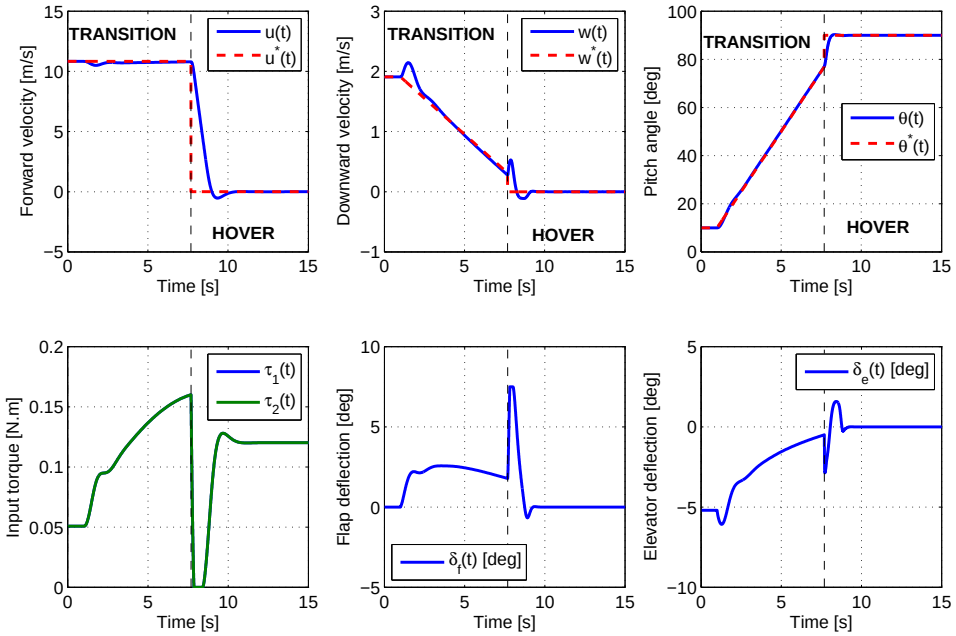

Figure 3.17: Transition from Level Flight to Hover simulation. The upper row depicts the forward velocity u, the downward velocity w and the pitch angle θ flow in time (blue line) and the references (red dashed line). The second row depicts the actuators' flow which have the highest influence on the variable portraited directly above.

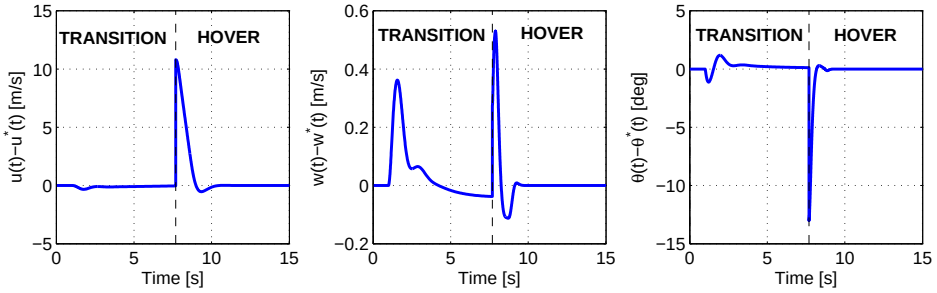

Figure 3.18: Tracking errors during transition from level flight to hover.

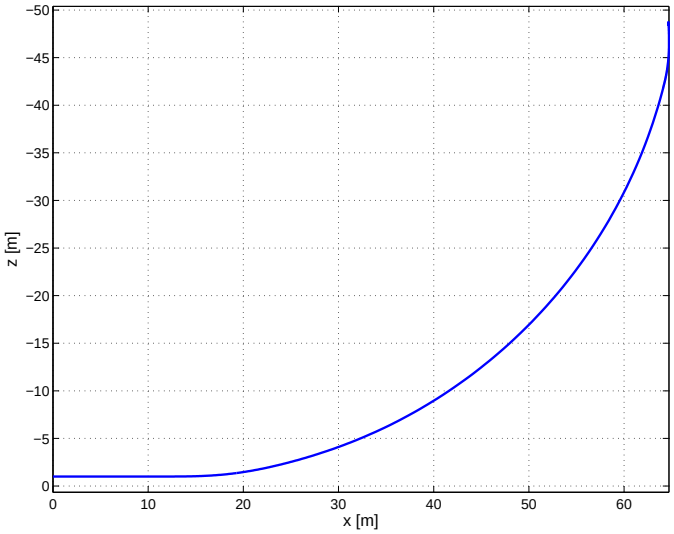

Figure 3.19: Aircraft vertical trajectory.

Simple reference trajectories were built according to some intuitive insight of the system. Appropriate controller dimensioning stabilized the aircraft in hover, level and all the equilibrium points spanned by the transition maneuver, according to simulation results. Moreover, the controllers proved to be robust to a collective change of ± 20 in the aircraft parameters.

Chapter 4

UAV Nonlinear Control

De spite the linear control solution feasibility, nonlinear control techniques are also exploited. However, due to its inherent complexity, model simplification is performed in Section 4.1. The nonlinear control synthesis is presented in Section 4.4 considering the simplified model but tested against the full model in Section 4.5.

4.1 Simplified UAV Model

Throughout this section the UAV model is described in the configuration manifold $\mathbb{S}^1 \times \mathbb{R}^2$ considering that the aircraft motion occurs solely on the vertical plane, i.e. the lateral motion is assumed to be non-existent which constitutes a reasonable approximation provided that there is additional lateral stabilization. This simplification is particularly important in the aircraft kinematic. The configuration of the body frame $\{B\}$ with respect to $\{N\}$ can be viewed as an element of the Special Euclidean group, $(\mathbf{R}, \mathbf{p}) = ({}^N_B\mathbf{R}, {}^N\mathbf{p}_B) \in \mathrm{SE}(2)$ where

$$\begin{aligned} {}^N\mathbf{p}_B &= [x\ z]^T, \\ {}^N_B\mathbf{R} &= \begin{bmatrix} \cos\theta & \sin\theta \\ -\sin\theta & \cos\theta \end{bmatrix}, \end{aligned} \tag{4.1}$$

thus eliminating the singularity in the rotation matrix parametrization which occurs in three-dimensional rotations. The kinematics are described by

$$\begin{aligned} {}^N\dot{\mathbf{p}}_B &= {}^N_B\mathbf{R}\mathbf{v}_B \\ \dot{\theta} &= q, \end{aligned} \tag{4.2}$$

where ${}^N\mathbf{p}_B = [x\ z]^T$ and $\mathbf{v}_B = [u\ w]^T$. Other simplifications made to the full system model described in Chapter 2 include:

- Propellers' dynamics are neglected. The thrust they provide is given by

$$T = \frac{T_1 + T_2}{2}. \tag{4.3}$$

- Lateral motion is stabilized which in turn implies that $T_1 - T_2$, δ_a, δ_r, v, p, r and y are all null;

- The stall angle does not depend on the actuator deflection but only on the angle of attack which must verify $|\alpha| < \bar{\alpha}$, where $\bar{\alpha} = 15\,^\circ$. Equation (2.40) was built under a very conservative view which is hereupon relaxed;

- Since the main contribution to the aircraft drag is that of the wing, the horizontal and vertical stabilizers drag as well as the flap contribution to the wing drag are neglected.

Under the previous considerations, the main forces acting on the aircraft body are the wing lift L_w, the horizontal stabilizer lift L_{hs} and the wing drag D_w which are given by

$$L_w = -\frac{1}{2}\rho A_w u^2 (C_{L_\alpha}\alpha + C_{L_{\delta_f}}\delta_f) - \frac{1}{2}\rho A_{p,w}(2u_p^2) C_{L_{\delta_f}}\delta_f \tag{4.4}$$

$$D_w = -\frac{1}{2}\rho A_w u^2 \left(C_{D_{0_w}} + \frac{(C_{L_\alpha}\alpha)^2}{\pi \mathcal{AR}_w e_w} \right) \tag{4.5}$$

$$L_{hs} = -\frac{1}{2}\rho A_{hs} u^2 (C_{L_\alpha}\alpha + C_{L_{\delta_e}}\delta_e) - \frac{1}{2}\rho A_{p,hs}(2u_p^2) C_{L_{\delta_e}}\delta_e. \tag{4.6}$$

The lifting forces L_{hs} and L_w produce the moments M_{hs} and M_w, respectively, due to their displacement with respect to the center of gravity. The moment M_{damp_q} defined in (2.49) remains valid in this analysis.

$$M_{hs} = -\,\mathbf{r}_{hs}.\,\mathbf{i}_B L_{hs} \tag{4.7}$$

$$M_w = -\,\mathbf{r}_w.\,\mathbf{i}_B L_w \tag{4.8}$$

The actuators input variables δ_e and δ_f can be changed into forces L_e and L_f, respectively, according to (4.9) and (4.10).

$$\delta_e = -\frac{L_e}{\frac{1}{2}\rho(2u_p^2)A_{p,hs}C_{L_{\delta_{e_{p,hs}}}} + \frac{1}{2}\rho u^2 A_{hs} C_{L_{\delta_{e_{hs}}}}} \tag{4.9}$$

$$\delta_f = -\frac{L_f}{\frac{1}{2}\rho(2u_p^2)A_{p,w}C_{L_{\delta_{f_{p,w}}}} + \frac{1}{2}\rho u^2 A_w C_{L_{\delta_{f_w}}}} \tag{4.10}$$

The dynamics equations (2.9) and (2.10) are rewritten in (4.11), (4.12) and (4.13) for the longitudinal case, under the aforementioned simplifications.

$$\dot{u} = \frac{1}{m}\left(2T - \frac{1}{2}\rho A_w u^2 \left(C_{D_{0_w}} + \frac{(C_{L_{\alpha_w}} \arctan\left(\frac{w}{u}\right))^2}{\pi \mathcal{AR}_w e_w}\right)\right) - g\sin\theta - qw \tag{4.11}$$

$$\dot{w} = \frac{1}{m}\left(L_f + L_e - \frac{1}{2}\rho u^2 (A_w C_{L_{\alpha_w}} + A_{hs} C_{L_{\alpha_{hs}}}) \arctan\left(\frac{w}{u}\right)\right) + g\cos\theta + qu \tag{4.12}$$

$$\dot{q} = \frac{1}{\mathbf{I}_y}\Bigg(- \mathbf{r}_w.\mathbf{i}_B L_f - \mathbf{r}_{hs}.\mathbf{i}_B L_e - \frac{1}{2}\rho(A_w C_{L_{\alpha_w}} \mathbf{r}_w.\mathbf{i}_B + A_{hs} C_{L_{\alpha_{hs}}} \mathbf{r}_w.\mathbf{i}_B) \arctan\left(\frac{w}{u}\right) \tag{4.13}$$
$$- \frac{1}{2}\rho A_{p,hs} C_{L_{\alpha_{p,hs}}} (\mathbf{r}_p.\mathbf{i}_B - \mathbf{r}_{hs}.\mathbf{i}_B) u_p q - \frac{1}{2}\rho A_{hs} C_{L_{\alpha_{p,hs}}} |\mathbf{r}_{hs}.\mathbf{i}_B| uq \Bigg)$$

Figure 4.1 depicts the overall planar dynamics described in this section which are the basis for the construction of the simplified Hybrid Automaton in Section 4.2

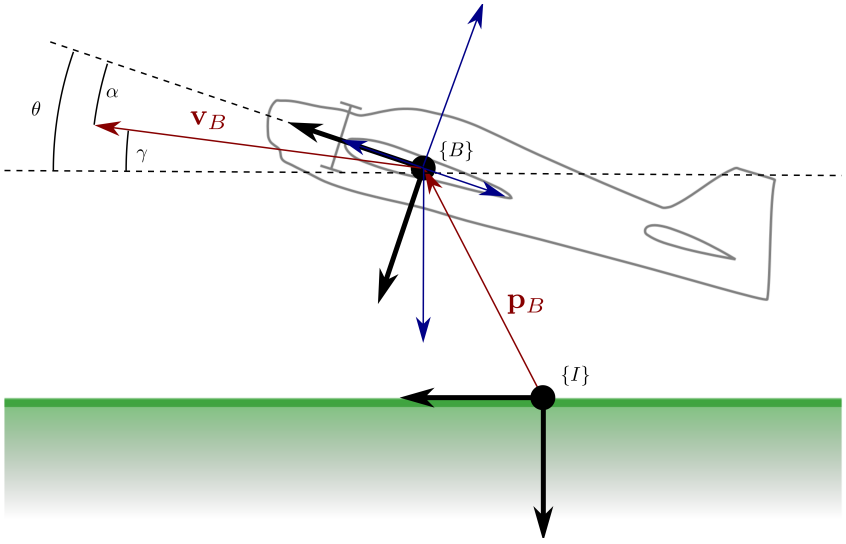

Figure 4.1: Aircraft two-dimensional representation.

4.2 Simplified Hybrid Automaton

The new state variable to be monitored is

$$\boldsymbol{\xi} = [u\ w\ q\ \theta\ x\ z]^T$$

where the motion outside the vertical plane is assumed already controlled and the propellers dynamic behavior is neglected. The Hybrid Automaton described in Section 2.4 is therefore required to change

accordingly being the most prominent changes those of the flow map. Since the set of operating modes and edges does not change their definition is not mentioned in this section.

4.2.1 Domain Mapping

The domain mapping is characterized by the set valued mapping $\mathcal{D} : \mathcal{Q} \rightrightarrows \mathbb{R}^6 \times \mathbb{R}^3 \times \mathcal{Q}^*$ where the actuators domain is the set $U \subset \mathbb{R}^3 \times \mathcal{Q}^*$ given by

$$U = [T_{min}, T_{max}] \times [\delta_{e_{min}}, \delta_{e_{max}}] \times [\delta_{f_{min}}, \delta_{f_{max}}] \times \mathcal{Q}^* \tag{4.14}$$

The domain mapping is

$$\begin{aligned}
\mathcal{D}(H) &= \mathbb{R}^3 \times B_{\bar{\theta}_H}(\pi/2) \times \mathbb{R} \times \mathbb{R}_{\leq 0} \times U, \\
\mathcal{D}(X) &= \mathbb{R}_{\geq 0} \times \mathbb{R}^4 \times \mathbb{R}_{\leq 0} \times U \bigcap \left\{(u, w) \in \mathbb{R}^2 : |\arctan(w/u)| < \bar{\alpha}\right\}, \\
\mathcal{D}(L) &= \mathbb{R}_{\geq 0} \times \mathbb{R}^3 \times \ B_{\bar{\theta}_L}(0) \times \mathbb{R} \times \mathbb{R}_{\leq 0} \times U \bigcap, \left\{(u, w) \in \mathbb{R}^2 : |\arctan(w/u)| < \bar{\alpha}\right\}
\end{aligned} \tag{4.15}$$

where an additional constraint has been added to the Transition domain in order to prevent discontinuities in the nonlinear controller.

4.2.2 Flow Map

The flow map $f : \mathcal{Q} \times \mathbb{R}^6 \times U \rightarrow \mathbb{R}^6$ describes the evolution of the state variables in each operating mode $q \in \mathcal{Q}$, i.e. in each operating mode the state's derivative is given by

$$\dot{\boldsymbol{\xi}} = f(q, \boldsymbol{\xi}, \boldsymbol{\mu}), \tag{4.16}$$

where function f is the the set of previously defined differential equations (4.11), (4.12), (4.13) and (4.2).

4.2.3 Guard Mapping

The guard mapping $\mathcal{G} : \mathcal{E} \rightrightarrows \mathbb{R}^6 \times \mathbb{R}^3 \times \mathcal{Q}^*$ is defined below.

$$\begin{aligned}
\mathcal{G}(H, X) &= B_{\chi_{H \rightarrow X}}(v^*_{X \rightarrow L}(0)), \\
\mathcal{G}(X, L) &= \left\{(\boldsymbol{\xi}, \boldsymbol{\mu}) \in \mathcal{D}(L) : |\theta| \leq \bar{\theta}_{X \rightarrow L} \wedge q^* = L\right\}, \\
\mathcal{G}(L, X) &= B_{\chi_{L \rightarrow X}}(v^*_{X \rightarrow H}(0)), \\
\mathcal{G}(X, H) &= \left\{(\boldsymbol{\xi}, \boldsymbol{\mu}) \in \mathcal{D}(H) : |\theta - \pi/2| \leq \bar{\theta}_{X \rightarrow H} \wedge q^* = H\right\},
\end{aligned} \tag{4.17}$$

4.2.4 Reset Map

The reset map is trivial because no changes in kinematics parametrization are required.

$$\begin{aligned}\mathcal{R}(H,X) &= \boldsymbol{\xi}\\ \mathcal{R}(X,L) &= \boldsymbol{\xi}\\ \mathcal{R}(L,X) &= \boldsymbol{\xi}\\ \mathcal{R}(X,H) &= \boldsymbol{\xi}\end{aligned} \tag{4.18}$$

4.3 Robust Maneuvers

The robust maneuvers are divided into three types within the Hybrid Automata framework described in [17]:

- ϵ-robust q_1 single reference maneuver $t \in [t_0, t_1)$;
- ϵ-robust $q_1 \to q_2$ approach maneuver in $t \in [t_0, t_f]$;
- (ϵ, δ_e)-robust $q_1 \to q_2$ transition maneuver in $t \in [t_0, t_1)$.

A maneuver taking place in operative mode q is ϵ-robust if it is ϵ-distant from any guard sets for any $t \in [t_0, t_1)$. A $q_1 \to q_2$ approach maneuver is ϵ-robust if its graph does not intersect any guard sets other than $\mathcal{G}(q_1, q_2)$ during time $t \in [t_0, t_f]$. Moreover, $v_{q_1}(t_f)$ must belong to the Guard set $\mathcal{G}(q_1, q_2)$. The $q_1 \to q_2$ transition maneuver is the $q_1 \to q_2$ approach maneuver union with a set of q_2 single maneuvers each of which is at most δ_ϵ-distant to the trajectory $v^*_{q_2}(t)$ starting point when the transition occurs. It is possible to successfully accomplish these maneuvers with a feedback control method which achieves reference trajectory tracking with an error lower than ϵ.

4.3.1 ϵ-robust H,L and X single maneuvers

A H single maneuver $v^*_H(t)$ is ϵ-robust if the following condition is verified

$$(\text{gr } v^*_H + B_\epsilon) \bigcap \mathcal{G}(H, X) = \varnothing, \tag{4.19}$$

where gr v^*_H is the reference maneuver graph. This condition is trivially satisfied if $q^* = H$. However, in the case that $q^* = L$ the maneuver must satisfy[1]

$$(\text{gr } v^*_H + B_\epsilon) \bigcap B_{\chi_{H\to X}}(v^*_{X\to L}(0)) = \varnothing \tag{4.20}$$

[1] For any given set $X \subseteq \mathbb{R}^n$ we denote with $X + B_\epsilon$ the set of all points ϵ-close to X, i.e. $\{y \in \mathbb{R}^n : \exists x' \in X s.t. \|x' - y\| \leq \epsilon\}$.

which constitutes an uninteresting scenario since the controller is asked to take the aircraft to level flight. A similar analysis may be built for the L single maneuver which is ϵ-robust if its graph $v_L^*(t)$ verifies

$$(\text{gr } v_L^* + B_\epsilon) \bigcap \mathcal{G}(L, X) = \varnothing. \tag{4.21}$$

Again, condition (4.21) is trivially verified if $q^* = L$ and is an uninteresting maneuver otherwise.

A X single maneuver is ϵ-robust if

$$(\text{gr } v_X^*(t) + B_\epsilon) \bigcap (\mathcal{G}(X, H) \cup \mathcal{G}(X, L)) = \varnothing. \tag{4.22}$$

These trajectories are uninteresting since the final state of the aircraft is intended to be in either Hover or Level and will not be further exploited.

4.3.2 ϵ-robust $H \to X$ and $L \to X$ approach maneuvers

A $H \to X$ approach maneuver is ϵ-robust if is at least ϵ-distant to any guard set other than $\mathcal{G}(H, X)$ and if

$$B_\epsilon(v_{H\to X}^*(t_f)) \subset \mathcal{G}(H, X) \tag{4.23}$$

which in turn implies that

$$B_\epsilon(v_{H\to X}^*(t_f)) \subset B_{\chi_{H\to X}}(v_{H\to L}^*(0)). \tag{4.24}$$

Similarly, a $L \to X$ approach maneuver is ϵ-robust if it is ϵ-distant to any guard sets different from $\mathcal{G}(H, X)$ and if the following condition is satisfied.

$$B_\epsilon(v_{L\to X}^*(t_f)) \subset B_{\chi_{L\to X}}(v_{H\to X}^*(0)). \tag{4.25}$$

An obvious consequence is that the conditions

$$\epsilon < \chi_{H\to X} \tag{4.26}$$

$$\epsilon < \chi_{L\to X} \tag{4.27}$$

must be verified for the approach maneuvers to be ϵ-robust.

4.3.3 ϵ-robust $X \to H$ and $X \to L$ approach maneuvers

A $X \to L$ approach maneuver is ϵ-robust if in addition to being at least ϵ-distant to the Guard set $\mathcal{G}(X, H)$ its graph also verifies

$$B_\epsilon(v^*_{X\to L}(t_f)) \bigcap \mathcal{G}(X, L). \tag{4.28}$$

The first condition is trivially satisfied with $q* = L$. Similarly to the $X \to L$ maneuver, the $X \to H$ approach maneuver is ϵ-robust if it is always ϵ-distant to any Guard set other than $\mathcal{G}(X, H)$ and furthermore condition (4.29) is verified.

$$B_\epsilon(v^*_{X\to H}(t_f)) \bigcap \mathcal{G}(X, H) \tag{4.29}$$

The second condition for either maneuver requires reference input $\boldsymbol{\mu}^*_{X\to L}$ calculation by means of system inversion. Given twice differentiable desired state trajectories $u^*(t)$ and $\theta^*(t)$, the downward velocity initial state $w(0)$ and considering the flaps nominally at rest, i.e. $L_f = 0$, for the whole approach maneuver, then the reference control inputs T^* and L^*_e, and the reference state variable w are computed numerically by solving (4.11), (4.12), (4.13) and (4.2). The chosen reference trajectories are

$$u^*(t) = \begin{cases} u_0 & \text{if } t_0 \le t < t_u \\ u_0 + (u_\infty - u_0)\exp(-\Phi_u(t-t_u))\left(\exp(\Phi_u(t-t_u)) - \Phi_u(t-t_u) - 1\right) & \text{if } t \ge t_u \end{cases} \tag{4.30}$$

$$\theta^*(t) = \begin{cases} \theta_0 & \text{if } t_0 \le t < t_\theta \\ \theta_0 + (\theta_\infty - \theta_0)\exp(-\Phi_\theta(t-t_\theta))\left(\exp(\Phi_\theta(t-t_\theta)) - \Phi_\theta(t-t_\theta) - 1\right) & \text{if } t \ge t_\theta \end{cases} \tag{4.31}$$

which are characterized by the initial forward velocity u_0, the final forward velocity u_∞, the initial pitch angle θ_0, the final pitch angle θ_∞, the transition start times t_θ and t_u and the parameters Φ_u and Φ_θ which determine the rate at which the transition is performed for each of the state variables u and θ, respectively. Figures 4.2 and 4.3 depict the $X \to L$ and $X \to H$ approach maneuver reference trajectories given the parameters listed in Tables 4.1 and 4.2. These reference maneuvers lie within the Transition Operating Mode domain and are far from any of its boundaries.

Variable	Value
u_0	1 m/s
u_∞	10.83 m/s
Φ_u	1 s$^-1$
t_u	0 s
θ_0	90 deg
θ_∞	10 deg
Φ_θ	0.7 s$^-1$
t_θ	0.1 s

Table 4.1: $X \rightarrow L$ approach maneuver parameters.

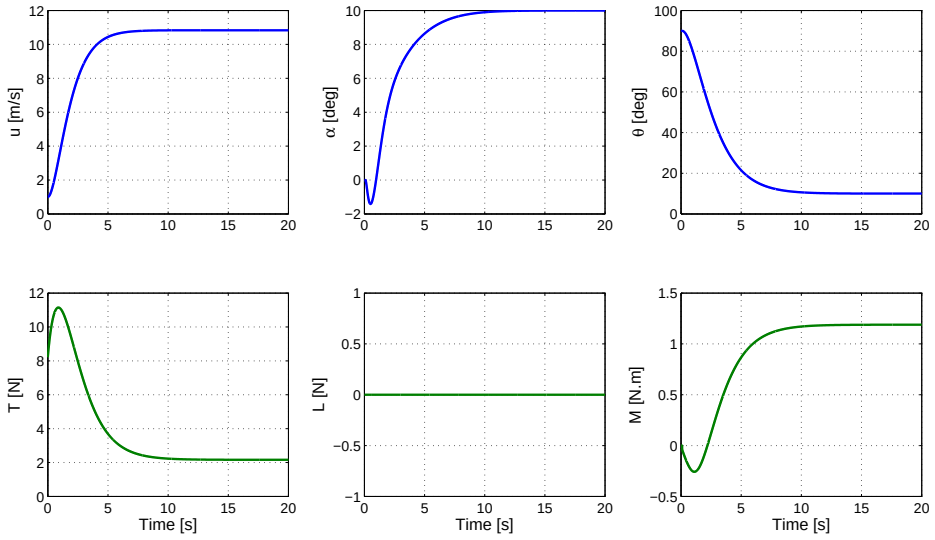

Figure 4.2: Hover to Level reference trajectories.

Variable	Value
u_0	10.83 m/s
u_∞	1 m/s
Φ_u	1 s$^-1$
t_u	8 s
θ_0	10 deg
θ_∞	90 deg
Φ_θ	0.7 s$^-1$
t_θ	0.1 s

Table 4.2: $X \rightarrow H$ approach maneuver parameters.

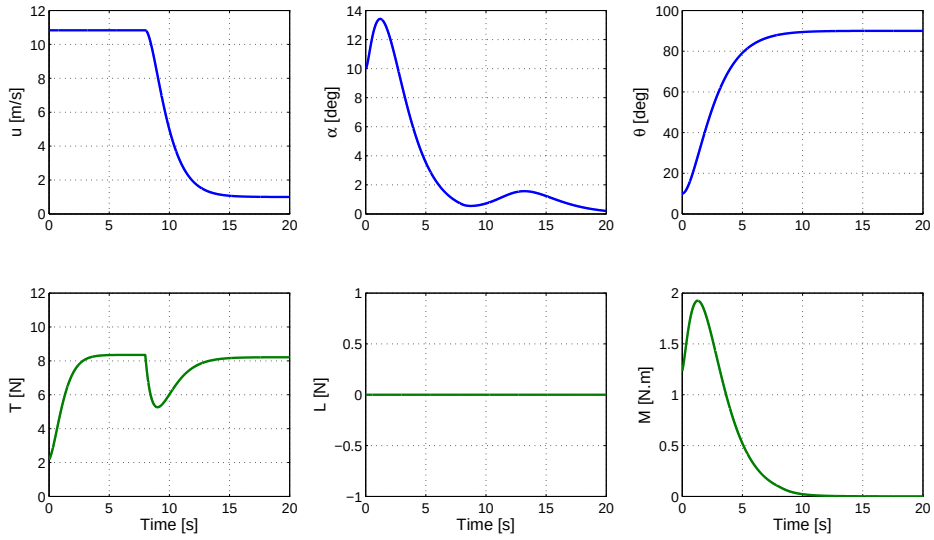

Figure 4.3: Level to Hover reference trajectories.

4.3.4 $(\epsilon, \delta_\epsilon)$-robust $q_1 \to q_2$ transition maneuver

Any $q_1 \to q_2$ transition maneuver with $(q_1, q_2) \in \mathcal{E}$ requires the corresponding $q_1 \to q_2$ approach maneuver to be ϵ-robust and the set $S^{q_1 \to q_2}$ defined in (4.33) to be populated with J_{δ_ϵ} q_2-single reference trajectories which ensure that after Operating Mode switching the state lies at most δ_ϵ-distant to some of the reference trajectories.

$$S^{q_1} = \left(\text{gr}v^*_{q_1 \to q_2}(t) + B_\epsilon\right) \bigcap \mathcal{G}(q_1, q_2) \tag{4.32}$$

$$S^{q_1 \to q_2} = \left\{ (\boldsymbol{\xi}, \boldsymbol{\mu}_{q_2}) \in \mathcal{D}(q_2) : \forall_{(\boldsymbol{\xi}', \boldsymbol{\mu}'_{q_1}) \in S^{q_1}}, \boldsymbol{\xi} = \mathcal{R}((q_1, q_2), \boldsymbol{\xi}', \boldsymbol{\mu}'_{q_1}) \right\} \tag{4.33}$$

As an example, if the $H \to X$ transition maneuver if $J_{\delta_\epsilon} = 1$ then $\delta_\epsilon \geq \chi_{H \to X}$.

4.4 Controller Design

Classic Linear Quadratic Regulator controllers are used in hover and level flight. A Transition Flight nonlinear controller is developed throughout this section which renders the aircraft Input-to-State stable (ISS) with restrictions. Complete information on this topic can be found in [26]. The input-to-state stability meaning outlined in Definition 2 requires the definition of class $\mathcal{K}$ functions given in Definition 1 and other mathematical constructions which evaluate the bounds of any given function. One such mathematical construction is that of infinite norm of a bounded piecewise-continuous function $f : [0, \infty) \to \mathbb{R}^k$, which is the quantity

$$\|f\|_\infty = \sup_{t \in [0, \infty)} \|f(t)\|. \tag{4.34}$$

The set of all such functions is denoted by $\mathcal{L}^k_\infty$. For any function $f \in \mathcal{L}^k_\infty$ another important quantity is the asymptotic norm $\|f\|_a$ which is given by

$$\|f\|_a = \lim_{t \to \infty} \sup \|f(t)\|. \tag{4.35}$$

Definition 1. *A continuous function $\gamma : [0, d) \to [0, \infty)$ is said to belong to the class $\mathcal{K}$ if it is strictly increasing and $\gamma(0) = 0$. If $d = \infty$ and γ is proper, i.e. $\lim_{r \to \infty} \gamma(r) = \infty$, then the function is said to belong to the class $\mathcal{K}_\infty$.*

Definition 2. *The dynamic system $\dot{\boldsymbol{\xi}} = f(\boldsymbol{\xi}, \boldsymbol{\mu})$ is said to be input-to-state stable with restrictions $X \subseteq \mathbb{R}^n$ on the initial state and $\Delta > 0$ on the input if there exist class $\mathcal{K}$ functions $\gamma_0 : \mathbb{R}^n \to \mathbb{R}$ and $\gamma : \mathbb{R}^m \to \mathbb{R}$ such that, for any input $\boldsymbol{\mu} \in \mathcal{L}^m_\infty$ satisfying $\|\boldsymbol{\mu}\|_\infty < \Delta$ and for any $\boldsymbol{\xi}_0 \in X$, the response*

$\boldsymbol{\xi}(t)$ *satisfies*

$$\begin{aligned} \|\boldsymbol{\xi}\| &\leq \max\{\gamma_0(\|\boldsymbol{\xi}_0\|), \gamma(\|\boldsymbol{\mu}\|_\infty)\} \\ \|\boldsymbol{\xi}\|_a &\leq \gamma(\|\boldsymbol{\mu}\|_a). \end{aligned} \tag{4.36}$$

Another important definition in the ISS systems framework establishment is that of local ISS-Lyapunov function, given in Definition 3

Definition 3. . *A C^1 function $V : \mathbb{R}^n \to \mathbb{R}$ is called a local ISS-Lyapunov function for the dynamic system $\dot{\boldsymbol{\xi}} = f(\boldsymbol{\xi}, \boldsymbol{\mu})$ if there exist class $\mathcal{K}_\infty$ functions $\bar{\eta} : \mathbb{R}^n \to \mathbb{R}$, $\underline{\eta} : \mathbb{R}^n \to \mathbb{R}$, $\eta : \mathbb{R}^n \to \mathbb{R}$, a class $\mathcal{K}$ function $\chi : \mathbb{R}^m \to \mathbb{R}$ and positive numbers δ_ξ and δ_μ such that, for all $\boldsymbol{\xi} \in \mathbb{R}^n$ and $\boldsymbol{\mu} \in \mathbb{R}^m$ such that $\|\boldsymbol{\xi}\| < \delta_\xi$ and $\|\boldsymbol{\mu}\| < \delta_\mu$ the following holds*

$$\underline{\eta}(\|\xi\|) \leq V(\boldsymbol{\xi}) \leq \bar{\eta}(\|\boldsymbol{\xi}\|) \tag{4.37}$$

and

$$\|\boldsymbol{\xi}\| \geq \chi(\|\boldsymbol{\mu}\|) \Rightarrow \frac{\partial V}{\partial \boldsymbol{\xi}} f(\boldsymbol{\xi}, \boldsymbol{\mu}) \leq -\eta(\|\boldsymbol{\xi}\|). \tag{4.38}$$

Proposition 1 follows from the local ISS-Lyapunov function definition.

Proposition 1. *The dynamic system $\dot{\boldsymbol{\xi}} = f(\boldsymbol{\xi}, \boldsymbol{\mu})$ is ISS with restrictions if and only if there exists a local Lyapunov function.*

Proof. See [26]. □

In order to build the nonlinear controller and prove the overall system stability and robustness the state equations are rewritten in a simpler form by substituting the relations

$$\begin{bmatrix} L \\ M \end{bmatrix} = \begin{bmatrix} 1 & 1 \\ -x_{ac_{hs}} & -x_{ac_w} \end{bmatrix} \begin{bmatrix} L_e \\ L_f \end{bmatrix} \tag{4.39}$$

into (4.11), (4.12) and (4.13), yielding

$$\begin{aligned} \dot{u} &= \frac{2T}{m} + h_u(u, w, q, \theta), \\ \dot{w} &= \frac{L}{m} + h_w(u, w, q, \theta), \\ \dot{q} &= \frac{M}{\mathbf{I}_y} + h_q(u, w, q), \\ \dot{\theta} &= q. \end{aligned} \tag{4.40}$$

This substitution effectively rescales the control input throughout the maneuver. The new control input is described by

$$\boldsymbol{\mu} = \begin{bmatrix} T^*(t) + \tilde{T} \\ M^*(t) + \tilde{M} \\ L^*(t) + \tilde{L} \end{bmatrix}, \quad \begin{aligned} \tilde{T} &= -k_u \tilde{u} \\ \tilde{M} &= -k_\theta(\tilde{\theta} + k_q \tilde{q}), \\ \tilde{L} &= -k_w \tilde{w} \end{aligned} \tag{4.41}$$

where $T^*(t)$, $M^*(t)$ and $L^*(t)$ are the reference inputs obtained by model inversion as explained in Section 4.3 and $\tilde{T}$, $\tilde{M}$ and $\tilde{L}$ are the errors which result from practical reference tracking. Proportional-derivative (PD) controllers are used to track the reference trajectories. Substituting (4.41) into the system state equations (4.40), the aircraft error dynamics are described by

$$\dot{\tilde{u}} = \frac{2\tilde{T}}{m} + \Psi_u(\tilde{u}, \tilde{w}, \tilde{q}, \tilde{\theta}, t) + \delta_u(t), \tag{4.42a}$$

$$\dot{\tilde{w}} = \frac{\tilde{L}}{m} + \Psi_w(\tilde{u}, \tilde{w}, \tilde{q}, \tilde{\theta}, t) + \delta_w(t), \tag{4.42b}$$

$$\dot{\tilde{q}} = \frac{\tilde{M}}{\mathbf{I}_y} + \Psi_q(\tilde{u}, \tilde{w}, \tilde{q}, t) + \delta_q(t), \tag{4.42c}$$

$$\dot{\tilde{\theta}} = q, \tag{4.42d}$$

where the functions Ψ_u, Ψ_w and Ψ_q described by (4.43) have been introduced and the perturbation terms $\delta_u(t)$, $\delta_w(t)$ and $\delta_q(t)$ have been added. These perturbations may appear due to parametric uncertainty, external disturbances and/or due to deviations from the vertical plane.

$$\begin{aligned}
\Psi_u(\tilde{u}, \tilde{w}, \tilde{q}, \tilde{\theta}, t) =& h_u(u^*(t) + \tilde{u}, w^*(t) + \tilde{w}, q^*(t) + \tilde{q}, \theta + \tilde{\theta}) \\
&- h_u(u^*(t), w^*(t), q^*(t), \theta^*(t)) \\
\Psi_w(\tilde{u}, \tilde{w}, \tilde{q}, \tilde{\theta}, t) =& h_w(u^*(t) + \tilde{u}, w^*(t) + \tilde{w}, q^*(t) + \tilde{q}, \theta + \tilde{\theta}) \\
&- h_w(u^*(t), w^*(t), q^*(t), \theta^*(t)) \\
\Psi_q(\tilde{u}, \tilde{w}, \tilde{q}, t) =& h_q(u^*(t) + \tilde{u}, w^*(t) + \tilde{w}, q^*(t) + \tilde{q}) \\
&- h_q(u^*(t), w^*(t), q^*(t))
\end{aligned} \tag{4.43}$$

The reference trajectory is one of equilibrium (if $\delta_u = \delta_w = \delta_q = 0$) because

$$[\tilde{u}\ \tilde{w}\ \tilde{q}\ \tilde{\theta}] = [0\ 0\ 0\ 0] \Rightarrow [\dot{\tilde{u}}\ \dot{\tilde{w}}\ \dot{\tilde{q}}\ \dot{\tilde{\theta}}] = [0\ 0\ 0\ 0].$$

The previous set of equations provides the foundations upon which the nonlinear controller's robustness emerges. Consider two separate but interconnected systems which describe the pairs $(\tilde{u}, \tilde{w})$ and (θ_1, θ_2), where $\theta_1 = \tilde{\theta}$ and $\theta_2 = \tilde{q} + \frac{\tilde{\theta}}{k_q}$. Input-to-State Stability is proven firstly for each of these system separately in Propositions 2 and 3. Input-to-State Stability for the overall system then follows from the Small Gain Theorem described in both [26] and [27], which is applied to the feedback interconnection depicted in Figure 4.4.

Proposition 2. *For some $c_u^* > 0$ and $c_w^* > 0$ and any numbers satisfying $\Delta > 0$, $\overline{\|(\theta_1, \theta_2\|} > 0$, $0 < c_u < c_u^*$ and $0 < c_w < c_w^*$ there exist $k_u > k_u^*$ and $k_w > k_w^*$ such that the system with the dynamics* (4.42a) *and* (4.42b) *is rendered ISS with restrictions c_u in the initial state $\tilde{u}(0)$, c_w on the initial state $\tilde{w}(0)$, Δ on the inputs $\delta_u(t)$ and $\delta_w(t)$ and $\overline{\|(\theta_1, \theta_2\|}$ on the input (θ_1, θ_2).*

Proof. Consider the Lyapunov function (4.44) and the level set definition given in (4.45).

$$V_1(\tilde{u}, \tilde{w}) = \frac{1}{2}(\tilde{u}^2 + \tilde{w}^2) \tag{4.44}$$

$$\Omega_1(l) = \{(\tilde{u}, \tilde{w}) \in \mathbb{R}^2 : V_1(\tilde{u}, \tilde{w}) \leq l\} \tag{4.45}$$

It turns out that, due to radial unboundedness there exist positive l_1 such that

$$\{(\tilde{u}, \tilde{w}) \in \mathbb{R}^2 : |\tilde{u}| \leq c_u \wedge |\tilde{w}| \leq c_w\} \subset \Omega_1(l_1). \tag{4.46}$$

Moreover, for any given reference trajectory it is possible to find c_u^*, c_w^* and l_1^* such that

$$\{(\tilde{u}, \tilde{w}) \in \mathbb{R}^2 : |\tilde{u}| \leq c_u^* \wedge |\tilde{w}| \leq c_w^*\} \subset \Omega_1(l_1^*), \tag{4.47}$$

and

$$\left\{(\tilde{u}, \tilde{w}) \in \Omega_1(l_1^*) : u^*(t) + \tilde{u} > 0 \wedge \left|\arctan\left(\frac{w^*(t) + \tilde{w}}{u^*(t) + \tilde{u}}\right)\right| < \bar{\alpha}\right\}, \tag{4.48}$$

hold true for all $t \geq 0$.

The functions defined in (4.43) are locally Lipschitz because the functions h_u, h_w and h_q are continuous and proper, therefore there exist positive L_u and L_w such that for all $(u, w) \in \Omega_1(l_1)$ and $\|(\theta_1, \theta_2)\| < \overline{\|(\theta_1, \theta_2)\|}$ the following holds

$$\left\|\Psi_u\left(\tilde{u}, \tilde{w}, \theta_2 - \frac{\theta_1}{k_q}, \theta_1, t\right)\right\| \leq L_u\|(\tilde{u}, \tilde{w}, \theta_1, \theta_2, t)\|, \tag{4.49}$$

$$\left\|\Psi_w\left(\tilde{u}, \tilde{w}, \theta_2 - \frac{\theta_1}{k_q}, \theta_1, t\right)\right\| \leq L_w\|(\tilde{u}, \tilde{w}, \theta_1, \theta_2, t)\|, \tag{4.50}$$

for all $t \geq 0$. The Lyapunov function derivative $\dot{V}_1$ is given by

$$\begin{aligned}\dot{V}_1 = \tilde{u}&\left(-\frac{2k_u}{m}\tilde{u} + \Psi_u\left(\tilde{u}, \tilde{w}, \theta_2 - \frac{\theta_1}{k_q}, \theta_1, t\right) + \delta_u(t)\right) \\ &+ \tilde{w}\left(-\frac{k_w}{m}\tilde{w} + \Psi_w\left(\tilde{u}, \tilde{w}, \theta_2 - \frac{\theta_1}{k_q}, \theta_1, t\right) + \delta_w(t)\right).\end{aligned} \tag{4.51}$$

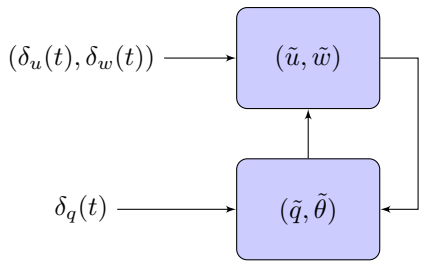

Figure 4.4: Interconnected systems $(\tilde{u}, \tilde{w})$ and (θ_1, θ_2).

Substituting (4.49) and (4.50) into (4.51) and using the triangle inequality the following relation is derived

$$\begin{aligned}\dot{V}_1 \leq & -\left(\frac{2k_u}{m} - L_u\right)\tilde{u}^2 + |\tilde{u}|(L_u + L_w)|\tilde{w}| - \left(\frac{k_w}{m} - L_w\right)\tilde{w}^2 \\ & + |\tilde{u}|L_u\|(\theta_1, \theta_2)\| + |\tilde{u}||\delta_u(t)| \\ & + |\tilde{w}|L_w\|(\theta_1, \theta_2)\| + |\tilde{w}||\delta_w(t)|,\end{aligned} \tag{4.52}$$

which can be rewritten as

$$\begin{aligned}\dot{V}_1 \leq & -\begin{bmatrix}\tilde{u} & \tilde{w}\end{bmatrix}\begin{bmatrix}\frac{2k_u}{m} - L_u & \pm\frac{1}{2}(L_u + L_w) \\ \pm\frac{1}{2}(L_u + L_w) & \frac{k_w}{m} - L_w\end{bmatrix}\begin{bmatrix}\tilde{u} \\ \tilde{w}\end{bmatrix} \\ & + |\tilde{u}|L_u\|(\theta_1, \theta_2)\| + |\tilde{u}||\delta_u(t)| \\ & + |\tilde{w}|L_w\|(\theta_1, \theta_2)\| + |\tilde{w}||\delta_w(t)|.\end{aligned} \tag{4.53}$$

The off-diagonal elements' sign in (4.53) may change with changes in the product $|\tilde{u}\tilde{w}|$. The symbol $\pm$ is used to account for this sign changes. The Lyapunov function's derivative can be upper bounded as by

$$\dot{V}_1 \leq -\lambda_{min}\|(\tilde{u}, \tilde{w})\|^2 + \|(\tilde{u}, \tilde{w})\|((L_u + L_w)\|(\theta_1, \theta_2)\| + \delta_u(t) + \delta_w(t)), \tag{4.54}$$

where λ_{min} is the smallest eigenvalue of the matrix in (4.53). It is easy to verify that for any $\Delta > 0$ and $\overline{\|(\theta_1, \theta_2)\|} > 0$ there exist $k_w^* > 0$ and $k_u^*(k_w^*) > 0$ such that for any $k_u > k_u^*$, $k_w > k_w^*$, $(\delta_u(t), \delta_w(t))$ satisfying $\|\delta_u(t)\|_\infty \leq \Delta$, $\|\delta_w(t)\|_\infty \leq \Delta$, and $\|(\theta_1, \theta_2)\| < \overline{\|(\theta_1, \theta_2)\|}$ and for any $(\tilde{u}, \tilde{w}) \in \Omega_1(l_1)$ the following holds

$$\dot{V}_1 < 0 \text{ if } \|(\tilde{u}, \tilde{w})\| > \frac{L_u + L_w}{\lambda_{min}}|(\theta_1, \theta_2)| + \frac{\delta_u(t) + \delta_w(t)}{\lambda_{min}}. \tag{4.55}$$

The system has a local ISS function, therefore it is ISS with restrictions c_u on the initial state $\tilde{u}(0)$, c_w on the initial state $\tilde{w}(0)$ and Δ on the inputs $\delta_u(t)$ and $\delta_w(t)$ as long as the conditions $c_u < c_u^*$ and $c_w < c_w^*$ are satisfied.

□

Proposition 3 employs similar arguments to those in Proposition 2 proof in order to justify the Input-to-State Stability of the closed-loop system (θ_1, θ_2).

Proposition 3. *For any arbitrary positive numbers Δ, $\overline{\|\tilde{u}, \tilde{w}\|}$, k_q, c_q and c_θ there exists $k_\theta^*(k_q) > 0$ such that $k_\theta > k_\theta^*$ renders the system with the dynamics* (4.42c) *and* (4.42d) *ISS with restrictions c_q on the initial state $\tilde{q}(0)$, c_θ on the initial state $\tilde{\theta}(0)$, $\overline{\|\tilde{u}, \tilde{w}\|}$ on the input $(\tilde{u}, \tilde{w})$ and Δ on the input $\delta_q(t)$.*

Proof. Consider the Lyapunov function described by (4.56) and the level set definition given in (4.57).

$$V_2(\theta_1, \theta_2) = \frac{1}{2}(\theta_1^2 + \theta_2^2) \tag{4.56}$$

$$\Omega_2(l) = \{(\theta_1, \theta_2) \in \mathbb{R}^2 : V_2(\theta_1, \theta_2) \leq l\} \tag{4.57}$$

Due to radial unboundedness there exists positive l_2 such that

$$\left\{(\theta_1, \theta_2)) \in \mathbb{R}^2 : |\theta_1| \leq c_\theta \wedge \left|\theta_2 - \frac{\theta_1}{k_q}\right| \leq c_q\right\} \subset \Omega_2(l_2). \tag{4.58}$$

The function Ψ_q is continuous and proper in $\Omega_2(l_2)$, therefore there exists positive L_q such that for all $(\theta_1, \theta_2) \in \Omega_2(l_2)$, $\|(\tilde{u}, \tilde{w})\| < \overline{\|(\tilde{u}, \tilde{w})\|}$ the following holds

$$\left\|\Psi_q\left(\tilde{u}, \tilde{w}, \theta_2 - \frac{\theta_1}{k_q}, t\right)\right\| \leq L_q\|(\tilde{u}, \tilde{w}, \theta_1, \theta_2, t)\|, \tag{4.59}$$

for all $t \geq 0$. The Lyapunov function derivative $\dot{V}_2$ is given by

$$\dot{V}_2 = \theta_1\left(\theta_2 - \frac{\theta_1}{k_q}\right) + \theta_2\left(-\frac{k_\theta k_q}{\mathbf{I}_y}\theta_2 + \Psi_q\left(\tilde{u}, \tilde{w}, \theta_2 - \frac{\theta_1}{k_q}, t\right) + \frac{\theta_2}{k_q} - \frac{\theta_1}{k_q^2}\right), \tag{4.60}$$

where the derivatives $\dot{\theta_1}$ and $\dot{\theta_2}$ are

$$\begin{aligned}\dot{\theta_1} &= \theta_2 - \frac{\theta_1}{K_q},\\ \dot{\theta_2} &= -\frac{k_\theta k_q}{\mathbf{I}_y}\theta_2 + \Psi_q\left(\tilde{u}, \tilde{w}, \theta_2 - \frac{\theta_1}{k_q}, t\right) + \frac{\theta_2}{k_q} - \frac{\theta_1}{k_q^2}.\end{aligned} \tag{4.61}$$

Let Ω be the set defined by

$$\Omega(\underline{l}, \bar{l}) = \left\{(\theta_1, \theta_2) \in \mathbb{R}^2 : \underline{l} \leq \|(\theta_1, \theta_2)\| \leq \bar{l}\right\}, \tag{4.62}$$

and let $\bar{l} = l_2$ and choose a number $\underline{l} \in \mathbb{R}^+$ satisfying $0 < \underline{l} < \bar{l}$. The Lyapunov function derivative taken on the set $\Omega(\underline{l}, \bar{l}) \cap \{(\theta_1, \theta_2) \in \mathbb{R}^2 : \theta_2 = 0\}$ is

$$\dot{V}_2 = -\frac{\theta_1^2}{k_q}, \tag{4.63}$$

verifying that $\dot{V}_2 < 0$. By continuity, the Lyapunov function derivative verifies this condition also in an open superset $\mathcal{M}$ of $\Omega(\underline{l}, \bar{l}) \cap \{(\theta_1, \theta_2) \in \mathbb{R}^2 : \theta_2 = 0\}$. Note that $\Omega(\underline{l}, \bar{l})/\mathcal{M}$ is compact and let

$$\begin{aligned}\underline{\theta_2} &= \min_{\theta_2 \in \Omega_2((\underline{l}), (\bar{l}))/\mathcal{M}} |\theta_2|,\\ \bar{\theta_2} &= \max_{\theta_2 \in \Omega_2((\underline{l}), (\bar{l}))/\mathcal{M}} |\theta_2| \text{ and}\\ \bar{\theta_1} &= \max_{\theta_1 \in \Omega_2(l_2)} |\theta_1|.\end{aligned}$$

Making use of the previous definitions it is possible to find the upper bound of the Lyapunov function derivative given in (4.64).

$$\dot{V}_2 \leq -\left(\frac{k_\theta k_q}{\mathbf{I}_y}\underline{\theta_2} - \left(\frac{1}{k_q} + L_q\right)\bar{\theta_2} - \left(1 + \frac{1}{k_q^2} + L_q\right)\bar{\theta_1} - L_q\overline{\|(\tilde{u}, \tilde{w})\|} - \Delta\right)|\theta_2| - \frac{\theta_1^2}{k_q} \tag{4.64}$$

It is easy to see that for any $\Delta > 0$ and $\overline{\|(\tilde{u},\tilde{w})\|} > 0$ there exists a suitable choice of $k_\theta^*(k_q) > 0$ such that for $k_\theta > k_\theta^*$, $\tilde{u}$, $\tilde{w}$ and $\delta_q(t)$ satisfying $\|(\tilde{u},\tilde{w})\| < \overline{\|(\tilde{u},\tilde{w})\|}$ and $|\delta_q(t)| < \Delta$ the Lyapunov function's derivative verifies $\dot{V}_2 < 0$ for any (θ_1,θ_2) belonging to $\Omega_2(\underline{l},\bar{l})$.

The system has a local ISS Lyapunov function therefore it is ISS with restrictions c_θ on the initial state $\tilde{\theta}(0)$, c_q on the initial state $\tilde{q}(0)$, $\overline{\|(\tilde{u},\tilde{w})\|}$ on the input $(\tilde{u},\tilde{u})$ and Δ on the input $\delta_q(t)$. □

Notice that the restrictions on the inputs of the interconnected systems

$$\|(\tilde{u},\tilde{w})\|_\infty < \overline{\|(\tilde{u},\tilde{w})\|} \text{ and } \|(\theta_1,\theta_2)\|_\infty < \overline{\|(\theta_1,\theta_2)\|}$$

are satisfied by taking

$$\overline{\|(\tilde{u},\tilde{w})\|} = \max_{(\tilde{u},\tilde{w})\in\Omega_1(l_1)} \|(\tilde{u},\tilde{w})\|$$

and

$$\overline{\|(\theta_1,\theta_2)\|} = \max_{(\theta_1,\theta_2)\in\Omega_2(l_2)} \|(\theta_1,\theta_2)\|.$$

Furthermore, it is possible to estimate the asymptotic gains k_1 and k_2 of the systems $(\tilde{u},\tilde{w})$ and (θ_1,θ_2), respectively, analysing the Lyapunov functions and considering null disturbances. For the first system, the asymptotic gain estimate is given by

$$k_1 = \frac{L_u + L_w}{\lambda_{min}}, \tag{4.65}$$

where λ_{min} decreases with increasing k_u and k_w. For the second system, the asymptotic gain estimate given in (4.67) is derived from the Lyapunov derivative upper bound given by

$$\dot{V}_2 \leq -\left(\frac{k_\theta k_q}{\mathbf{I}_y} - \frac{1}{k_q} - L_q\right)\theta_2^2 - \frac{1}{k_q^2}\theta_1^2 + |\theta_1\theta_2|\left(1 + \frac{1}{k_q^2} + L_q\right) + |\theta_2| L_q \overline{\|(\tilde{u},\tilde{w})\|}. \tag{4.66}$$

$$k_2 = \frac{L_q}{\frac{k_\theta k_q}{\mathbf{I}_y} - \frac{1}{k_q} - L_q}. \tag{4.67}$$

Under the previous definitions and results, the input-to-state stability for the overall system is established in Proposition 4.

Proposition 4. *For some $c_u^* > 0$ and $c_w^* > 0$ and any numbers satisfying $\Delta > 0$, $0 < c_u < c_u^*$, $0 < c_w < c_w^*$, $k_q > 0$, $c_q > 0$ and $c_\theta > 0$ there exist $k_u^* > 0$, $k_w^* > 0$ and $k_\theta^*(k_q) > 0$ such that the system with dynamics* (4.42) *is rendered ISS with restrictions c_u on the initial state $\tilde{u}(0)$, c_w on the initial state $\tilde{w}(0)$, c_q on the initial state $\tilde{q}(0)$, c_θ on the initial state $\tilde{\theta}(0)$ and Δ on the inputs $\delta_u(t)$, $\delta_w(t)$ and $\delta_q(t)$.*

Proof. Input-to-state stability with restrictions for the individual systems $(\tilde{u},\tilde{w})$ and (θ_1,θ_2) is proved in Propositions 2 and 3, respectively. The small gain theorem requires that the condition

$$k_1 k_2 < 1$$

is met, where k_1 is the closed-loop system $(\tilde{u}, \tilde{w})$ asymptotic gain relative to the input (θ_1, θ_2) and, similarly, k_2 is the closed-loop system (θ_1, θ_2) asymptotic gain relative to the input $(\tilde{u}, \tilde{w})$. The asymptotic gain k_1 decreases with increasing k_u or k_w and k_2 can be fixed arbitrarily with an appropriate choice of k_θ, therefore, the small gain theorem condition is met. Moreover, the tracking error can be made arbitrarily small. □

Proposition 4 concludes the stability and robustness analysis. We have proven that a transition trajectory can be tracked with an arbitrary small error. This allows for the use of the Hybrid Automata framework to achieve stability of the overall hybrid system. The next section presents simulation results which makes use of the open-source hybrid systems simulator presented in [28].

4.5 Simulation Results

The controller is tested in the full model with the controller gains specified in Table 4.3 and an LQR controller providing lateral stabilization during transition[2]. The input variable T must be transformed

Gain	Value
k_u	$10\ Ns/m$
k_w	$10\ Ns/m$
k_q	$1\ s$
k_θ	$10\ Nms/rad$

Table 4.3: Controller gains.

into the real input variables $\tau_{1,2}$. This task is accomplished using the relation

$$\tau = \frac{\rho d^5 C_P n^2}{2\pi} \tag{4.68}$$

where n is the propeller speed which provides the thrust $T = T^* + \tilde{T}$ and it is the solution of (2.21) therefore disregarding the propellers' dynamic behavior which would require $\dot{n}$ computation. This imprecision adds to the perturbation terms δ_u, δ_w and δ_q which the control loop is able to handle.

[2]The linearization point is that of Section 3.2.3.

4.5.1 Hover to Level Flight transition

The simulation results for the Hover to Level transition are presented in Figure 4.5. The aircraft starts in Hover and its velocity immediately starts to increase up to 1 m/s which is the maneuver $v^*_{X\to L}(t)$ starting point. The aircraft operating mode switches to Transition at $t = 0.9$ s and to Level at $t = 7.9$ s. It is noticeable from Figure 4.5 that the time lag in $u^*(t)$ tracking which increases tracking errors in every other variables. Figure 4.6 depicts the tracking errors $\tilde{u}$, $\tilde{w}$ and $\tilde{\theta}$ in the upper row and the input errors $\tilde{T}$, $\tilde{\delta_f}$ and $\tilde{\delta_e}$ are depicted in the bottom row. The major tracking error is $\tilde{u}$ due to the propellers' lag time. The maneuver trajectory on the vertical plane is depicted in Figure 4.7 which is very similar to that presented in Chapter 3.

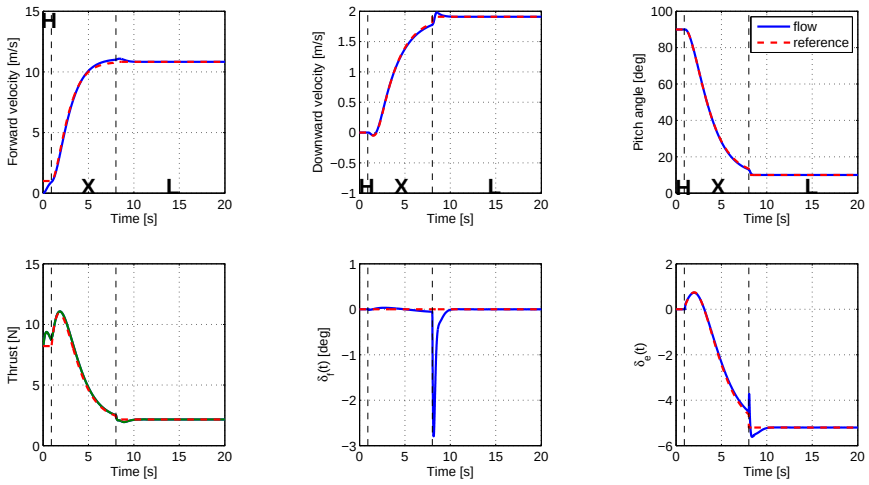

Figure 4.5: Hover to Level Flight simulation. The upper row depicts the system state variables u, w and θ, while the second row depicts the actuators input.

4.5.2 Level Flight to Hover transition

The simulation results for the Level to Hover transition are presented in Figure 4.8. The switching from Level to Transition occurs at $t = 0$ s because the aircraft is at the equilibrium point which lies within the guard map. Switching to Hover occurs at $t = 4.4$ s thus providing a faster transition between Level Flight and Hover than that of Hover to Level Flight. However, this more demanding transition induces higher errors in reference tracking. Figure 4.9 depicts the tracking errors during the maneuver, complementing the information depicted in Figure 4.8. The maneuver trajectory on the vertical plane is depicted in Figure 4.10 which is also very similar to that presented in Chapter 3.

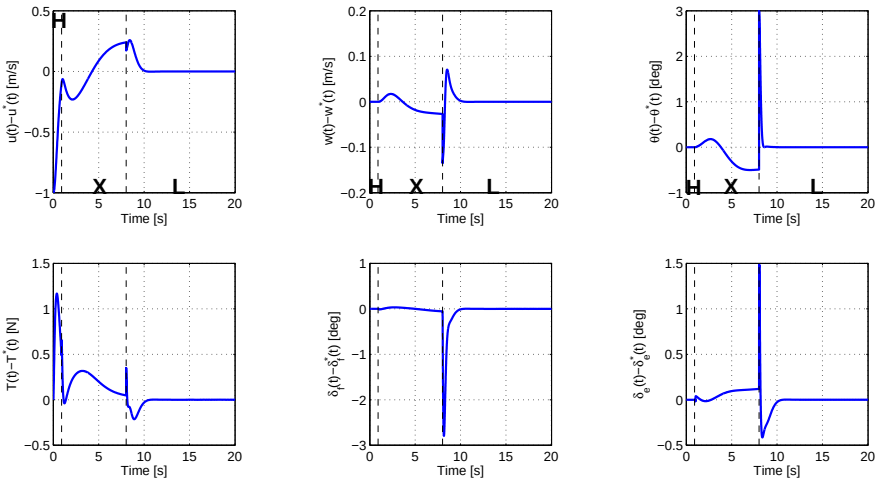

Figure 4.6: Tracking errors during transition from Hover to Level Flight.

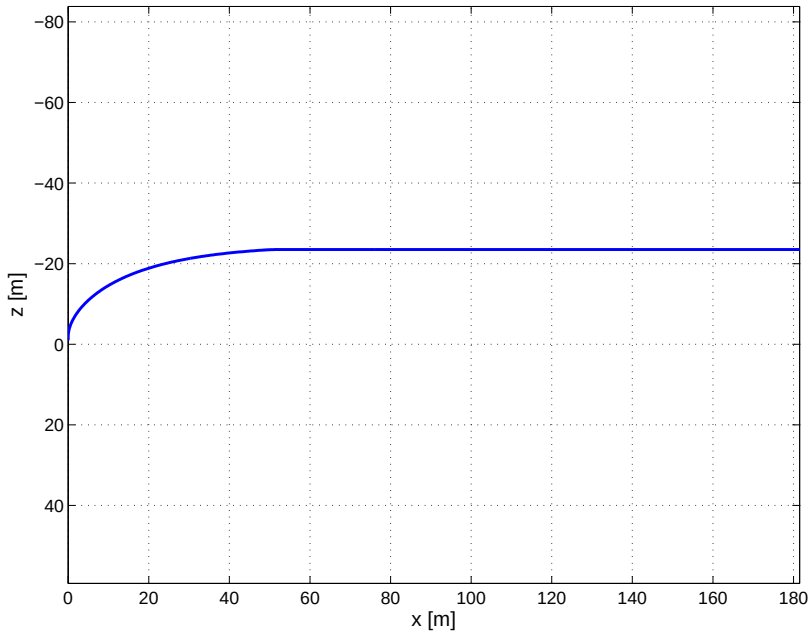

Figure 4.7: Aircraft vertical trajectory.

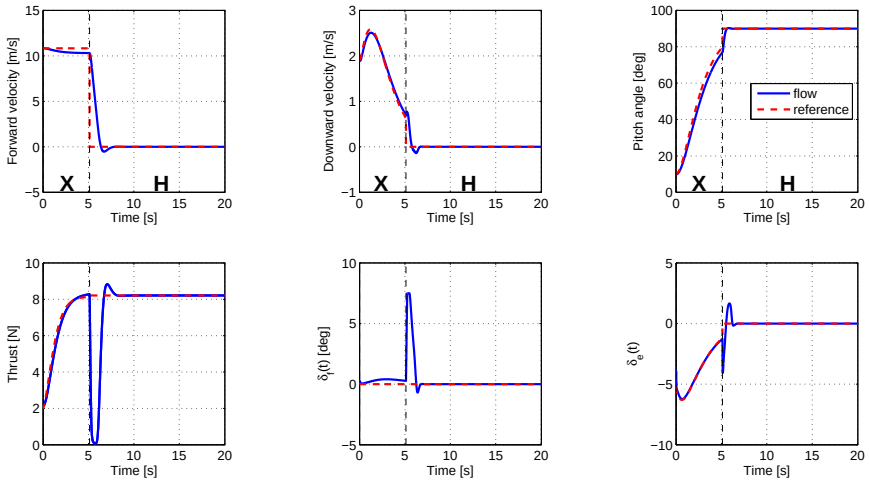

Figure 4.8: Level flight to hover simulation. The upper row depicts the system state variables u, w and θ, while the second row depicts the actuators input.

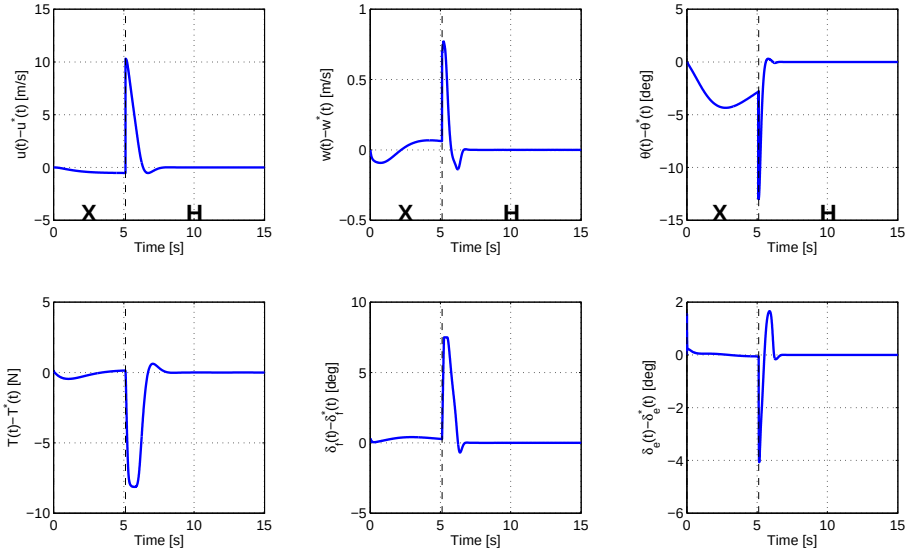

Figure 4.9: Tracking errors during transition from level flight to hover.

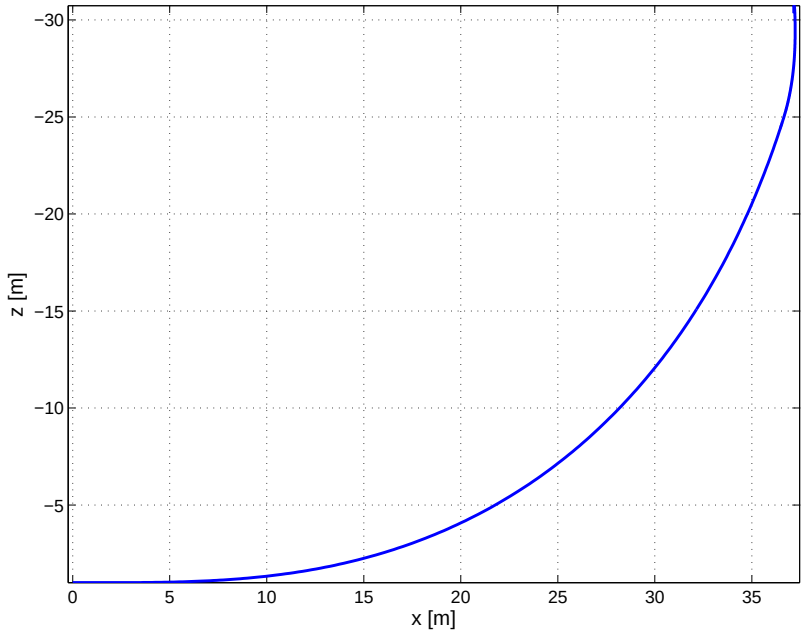

Figure 4.10: Level to Hover -Aircraft vertical trajectory.

4.6 Summary

This chapter elaborates a simpler nonlinear aircraft model and hybrid automaton than that presented in Chapter 2. Namely the general 3-dimensional dynamics are substituted by the 2-dimensional dynamics which characterize the aircraft motion in the vertical plane, assuming that the lateral motion is fully stabilized.

Under these assumptions, the reference ϵ-robust approach maneuvers $v^*_{X\to L}$ and $v^*_{X\to H}$ are built by means of model inversion. A locally input-to-state stable controller with restrictions on the initial state and inputs provides practical reference tracking with arbitrarily small tracking error.

The controller is dimensioned in Appendix D and tested within the Hybrid Systems simulation environment with the full 3-dimensional model implementation. The Linear Quadratic Regulator is used to provide hover and level flights stabilization as well as lateral stabilization while in Transition. These simulations demonstrate the controller's ability to deal with the external disturbances.

Chapter 5

Conclusion & Future Work

This thesis presented an Unmanned Air Vehicle (UAV) model which described the aircraft dynamics during both hover and level flights. The main forces and moments affecting the aircraft dynamics can be divided into three different classes - gravity, propeller and aerodynamics - according to their nature. The aerodynamic forces and moments arise from the free-stream flow and the propeller slipstream which are computed separately and combined together in the end using superposition. An appropriate choice of the inertial and body-fixed coordinates frames was essential for kinematic modeling, where the Euler angles provided rotation parametrization. Moreover, this model also included the propeller dynamics, increasing the model's accuracy with respect to the model presented in [6]. The Hybrid Automata framework provided the means to handle controller switching between the three operating modes: Hover, Level and Transition.

Linear Optimal techniques successfully provided Hover and Level stabilization as well as reference tracking during the transition between these two operating modes. Furthermore, this solution proved to be robust with respect to parameters change. Similar solutions were employed in [8], [9], [10] and [11] and their success was only proved within a simulation environment. Successful real world transitions between hover and level flights are presented in [4], [6] and [7] which employ either open-loop or remotely operated maneuvers.

Therefore, Chapter 4 constitutes the most important contribution of this thesis for it provides a formal proof of stability and robustness within a 2-dimensional aircraft model. The nonlinear controller designed in this chapter renders the system locally input-to-state stable with restriction on the disturbances inputs and initial state. Reference maneuvers design by means of model inversion combined with practical reference tracking provides robust transition between the two disjoint operating modes Hover and Level.

Simulation results proved that both linear and nonlinear control laws constitute a feasible solution to the problem which was stated in Chapter 1. Future work relies on:

- Controller analysis in the presence of wind disturbances and sensor noise within the simulation environment;
- Transition trajectories optimization;
- Model verification and more accurate parameter estimation with real world testing which would create a reliable platform for controller design, verification and validation;
- Controller implementation at the given aircraft platform constitutes also the basis for future work.

Appendix A

Model Parameters Estimation

The model parameters outlined in Chapter 2 are organized according the aircraft element they describe. However, throughout this section the model parameters are organized into the following categories:

- Geometry;
- Mass properties;
- Aerodynamics.

These categories group several parameters sharing similar methods, assumptions and procedures throughout the estimation process. They are described in Sections A.1, A.2, and A.3, respectively.

A.1 Geometry

Model geometry measurement is a very straightforward procedure which requires only a ruler. During this procedure the following variables were measured:

- Propellers' locations $\mathbf{r}_{p_{1,2}}$;
- Propellers' diameter d;
- Lifting surfaces' distance to the center of gravity $\mathbf{r}_{hs,vs,w}$[1];
- Lifting surfaces' root chords $c_{r_{hs,vs,w}}$;

[1] This measurement was made under the assumption that the aerodynamic center of a lifting surface lies in the quarter-chord line. The center of gravity is easily marked on the aircraft body.

- Lifting surfaces' tip chords $c_{t_{hs,vs,w}}$ and;
- Lifting surfaces' span $b_{hs,vs,w}$.

Other geometric parameters were derived from this measurements, including:

- Lifting surfaces' areas $A_{hs,vs,w}$ and;
- Lifting surfaces' aspect ratio $\mathcal{R}_{hs,vs,w}$, given by

$$\mathcal{R} = \frac{b^2}{A}. \tag{A.1}$$

A design table built with Microsoft® Excel was linked with Solidworks® Computer Aided Design software allowing automatic geometry generation. The result is presented in Figure A.1.

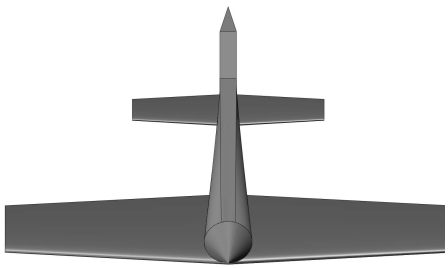

Figure A.1: Aircraft CAD model.

Figure A.2 depicts the aircraft top view with the propellers washed surfaces in grey. Propeller washed areas are very hard to estimate and they generally depend on the current thrust and forward velocity. Assuming that the propellers' slipstream always fills a cylinder with the same radius as the propellers then the washed areas are constant. Moreover, some flow is dragged by the propellers' slipstream due to viscous effects which interact with the vertical stabilizer. For the sake of simplicity it is considered that the vertical stabilizer area affected by the slipstream is the projection of the slipstream cylinder onto this surface. Under these assumptions, the parameters $A_{p,hs}$, $A_{p,vs}$, and $A_{p,w}$ are computed using the equations (A.2) and (A.3)

$$c(y) = c_r \left(1 + \frac{y}{b/2}\left(\lambda - 1\right)\right) \tag{A.2}$$

$$A = \frac{(y_1 - y_0)(c(y_1) + c(y_0))}{2} \tag{A.3}$$

where y_0 and y_0 are spanwise coordinates, $c(y)$ is the surface's chord at y, A is the trapeze area and λ is the taper ratio which is given by

$$\lambda = \frac{c_t}{c_r}. \tag{A.4}$$

The last geometry parameters are the aileron center of pressure distance to the symmetry plane

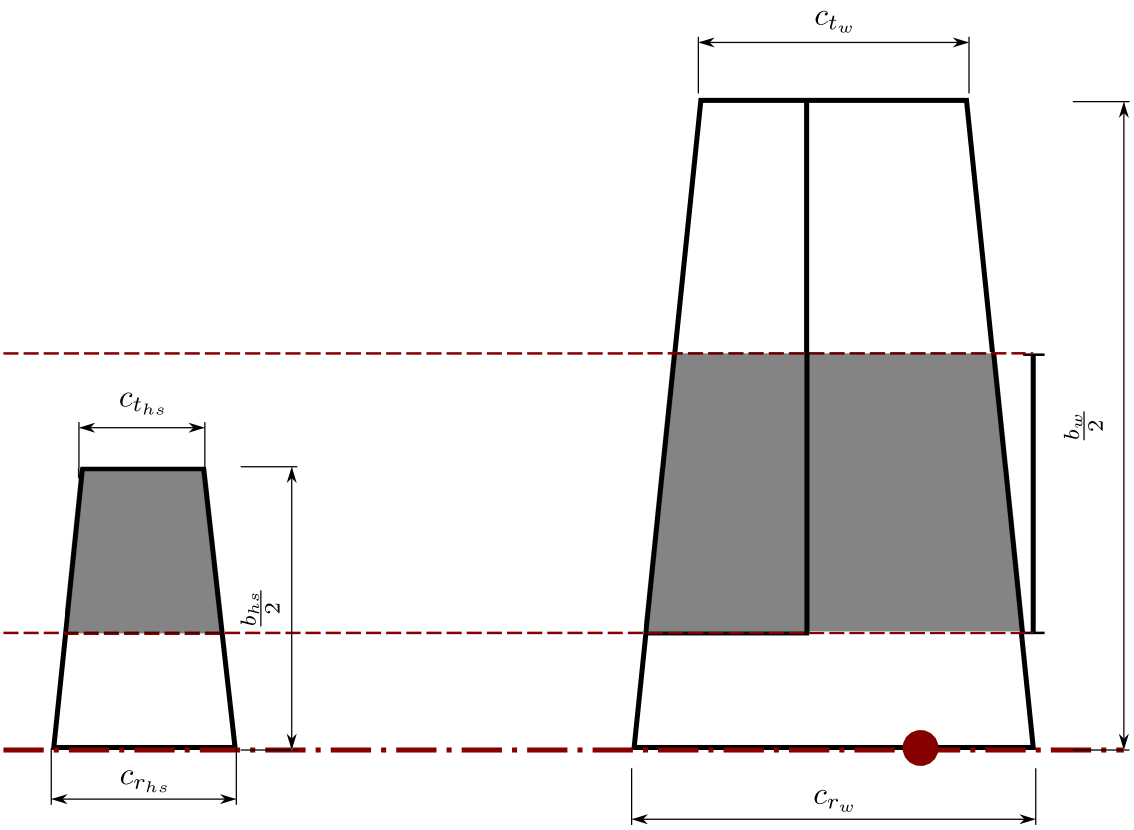

Figure A.2: Aircraft basic geometry - top view. The figure depicts important geometry dimensions and the propeller washed areas which are greyed out.

$\mathbf{r}_a \cdot \mathbf{j}_B$ and its washed counterpart $\mathbf{r}_{p,a} \cdot \mathbf{j}_B$[2]. Assuming a linear distribution of lift the center of pressure is coincident with the surface geometric center c_p which is given by

$$c_p = y_0 + \frac{(y_1 - y0)(2\lambda + 1)}{3(\lambda + 1)}. \tag{A.5}$$

[2]Although $\mathbf{r}_{p,a} \in \mathbb{R}^3$ only the y-coordinate is important in aerodynamic moments calculations (see Section 2.3.3)

A.2 Mass properties

Model geometry provided the required data to build the rough three dimensional aircraft model presented in Figure A.1. The CAD model body parts were given the styrofoam physical properties out of which the real-world model was built. The fuselage's fore side is a simple representation of the aircraft avionics. This conic element has a higher density which was chosen so as to match the CAD model's mass with that of the real aircraft. Another mass properties such as Moments of Inertia $\mathbf{I}_x$, $\mathbf{I}_y$ and $\mathbf{I}_z$ are calculated with the given software.

A.3 Aerodynamics

The aircraft aerodynamic parameters' accurate calculation requires either Computational Fluid Dynamics methods or wind-tunnel testing. However, some simple calculations presented below provide reasonable first estimates. The aircraft controllers are expected to deal with parametric uncertainty up to some degree.

- The Oswald's efficiency parameter $e = 0.8$ is assumed to be the same for every lifting surface. This approximation is valid for trapezoidal surfaces according to [29];
- The parasitic coefficient of drag $C_{D_0} = 0.01$ lies within the acceptable range of values according to [29] and is the same for every lifting surface;
- The parameter C_{L_α} (and similarly C_{L_β}) is given by

$$C_{L_\alpha} = \frac{C_{l_\alpha}}{1 + \frac{C_{l_\alpha}}{\pi \mathcal{AR}}} \tag{A.6}$$

  where $C_{l_\alpha} = 2\pi$ is the derivative C_{L_α} of a infinite wing (see [30] for further details);
- Actuator deflection δ_j changes the airfoil curvature which corresponds to an angle of attack increase given by[3]

$$\Delta\alpha = -\frac{\partial C_l}{\partial \delta_j}\frac{K'}{C_{l_\alpha}}\delta_j \tag{A.7}$$

  where $\frac{\partial C_l}{\partial \delta_j}$ is a function of the ratio between the actuator chord and the lifting surface chord. The derivative $C_{L_{\delta_j}}$ is given by

[3] The actuator is considered to be a plane flap.

$$C_{L_{\delta_j}} = C_{L_\alpha} \frac{\partial \alpha}{\partial \delta_j} \frac{A_j}{A} \tag{A.8}$$

where $\frac{A_j}{A}$ is a area correction which distinguishes the lifting surface's area spanned by the actuator A_j and the overall area A. The values $K' = 1$ and $\frac{\partial C_l}{\partial \delta_j} = 5.5$ are taken from table values in [29] considering $c_f/c = 0.4$;

- The previous analysis is performed for flap deflections but not for rudder and elevator deflections because these actuators have very high chord ratios. It is assumed that:

$$\begin{aligned} C_{L_{\delta_e}} &= C_{L_{\delta_{e_p}}} = C_{L_\alpha} \\ C_{L_{\delta_r}} &= C_{L_{\delta_{r_p}}} = C_{L_\beta}, \end{aligned} \tag{A.9}$$

  i.e. the actuators are assumed to move the whole lifting surface.

Appendix B

Propeller Slipstream Velocity

The propeller slipstream velocity u_p is computed using the Bernoulli's law and the momentum transfer theory. The Bernoulli's law states that for an inviscid, incompressible, and steady fluid flow equation (B.1) holds true along any streamline,

$$\frac{1}{2}\rho u_i^2 + \rho g h_i + p_i = constant \tag{B.1}$$

where u_i, h_i and p_i are the velocity, height and pressure at any given location i. Figure B.1 depicts the thrust generation process where:

- The control volume in black dashed lines preserves the fluid mass within its boundaries;
- The control volume in blue dashed lines has a infinitesimal extension dx;
- The blue lines inside the control volume depict two different streamlines.

Starting with the infinitesimal control volume and applying the conservation of mass principle the following equation is derived,

$$\rho\frac{\pi d^2}{4}u_{in} = \rho\frac{\pi d^2}{4}u_{out} \Rightarrow u_{in} = u_{out}. \tag{B.2}$$

Computing the momentum transfer in the flow direction which provides the thrust T around the same control volume the following equation is derived,

$$T = \frac{\pi d^2}{4}\left(p_{in} - p_{out}\right) + \rho\frac{\pi d^2}{4}\left(u_{in}^2 - u_{out}^2\right) \Rightarrow T = \frac{\pi d^2}{4}\left(p_{in} - p_{out}\right) \tag{B.3}$$

Applying Bernoulli's law to both stream lines, the following relations hold true

$$p_0 + \frac{1}{2}\rho u^2 = p_{out} + \frac{1}{2}\rho u_{out}^2 \tag{B.4}$$

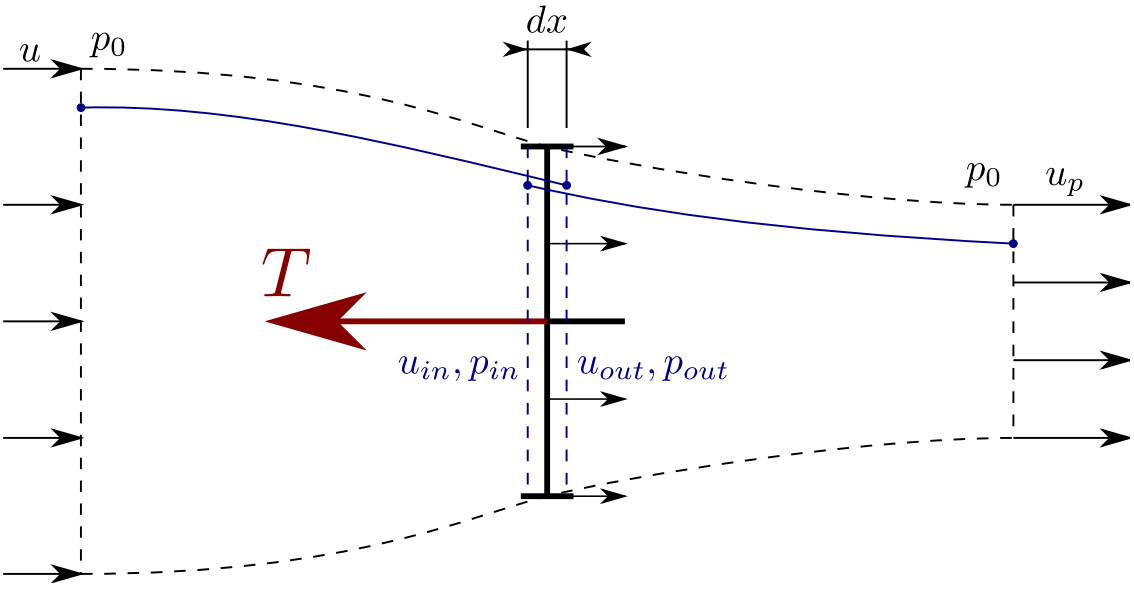

Figure B.1: Propeller Thrust and slipstream velocity.

$$p_{in} + \frac{1}{2}\rho u_{in}^2 = p_0 + \frac{1}{2}\rho u_p^2. \tag{B.5}$$

By construction, the conservation of mass also applies to the black dashed control volume in Figure B.1

$$\rho A_1 u = \rho A_2 u_p = \rho \frac{\pi d^2}{4} \bar{u} \tag{B.6}$$

where A_1 is the fore side area, A_2 is the aft side area and $\bar{u} = u_{in} = u_{out}$. Combining equation (B.5), (B.4) and (B.6) the Thrust relation with slipstream velocity is derived

$$T = \frac{1}{2}\rho \frac{\pi d^2}{4} \left(u_p^2 - u^2\right). \tag{B.7}$$

Appendix C

Simulation Environment

There are not any straightforward Hybrid Systems simulation tools to this date and this subject is undergoing active research [28]. The Matlab/Simulink simulation environment provided in [31] was used throughout the work reported in this thesis with slight modifications depicted in C.1.

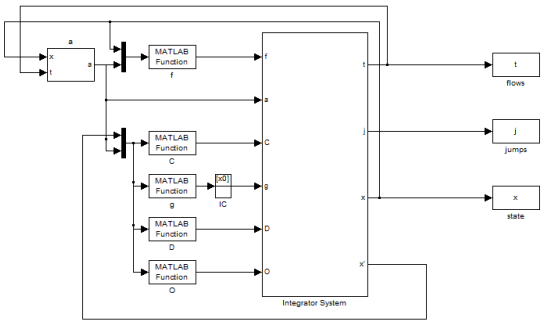

Figure C.1: Simulation environment overview.

This simulation tool requires the Hybrid Automaton framework to be described as a generic Hybrid System which is characterized by a Flow Map F, a Jump Map G, a Flow Set C and a Jump Set D, where

$$
\begin{aligned}
C_q &= \mathcal{D}(q) \\
F_q &= f(q, \boldsymbol{\xi}, \boldsymbol{\mu}), \text{for all } (\boldsymbol{\xi}, \boldsymbol{\mu}) \in C_q \\
D_q &= \bigcup_{\{(q,q') \in \mathcal{E}\}} \mathcal{G}(q, q') \\
G_q &= \bigcup_{\{q' : \boldsymbol{\xi} \in \mathcal{G}(q,q')\}} \left(\mathcal{R}(q, q', \boldsymbol{\xi}), q'\right), \text{for all } (\boldsymbol{\xi}, \boldsymbol{\mu}) \in D_q
\end{aligned}
\tag{C.1}
$$

The simulation blocks f, C, D, and g depicted in C.1 identify F, C, D and G, respectively. The block a identifies the implemented control law and the block O is not included in the Hybrid System description but may comprise logic assertions which render the current simulation either valid or invalid. Further details on this simulation tool may be found in [12] or in the author's web page [31].

Appendix D

Nonlinear controller analysis

This appendix presents a numerical analysis on the concepts exploited throughout Chapter 4.

D.1 Lipschitz constants estimation

The functions $\Psi_u(\tilde{u}, \tilde{w}, \tilde{q}, \tilde{\theta}, t)$, $\Psi_w(\tilde{u}, \tilde{w}, \tilde{q}, \tilde{\theta}, t)$ and $\Psi_q(\tilde{u}, \tilde{w}, \tilde{q}, t)$ are Lipschitz but their Lipschitz constants L_u, L_w and L_θ remain to be estimated during the forthcoming analysis. The Lipschitz constants in (4.49), (4.50) and (4.59) verify

$$\begin{aligned} \|\nabla\Psi_u(\tilde{u}, \tilde{w}, \tilde{q}, \tilde{\theta}, t)\|\Big|_{(\tilde{u},\tilde{w},\tilde{q},\tilde{\theta})=(0,0,0,0)} &\leq L_u \\ \|\nabla\Psi_w(\tilde{u}, \tilde{w}, \tilde{q}, \tilde{\theta}, t)\|\Big|_{(\tilde{u},\tilde{w},\tilde{q},\tilde{\theta})=(0,0,0,0)} &\leq L_w \\ \|\nabla\Psi_q(\tilde{u}, \tilde{w}, \tilde{q}, t)\|\big|_{(\tilde{u},\tilde{w},\tilde{q})=(0,0,0)} &\leq L_q \end{aligned} \tag{D.1}$$

for all $t \geq 0$. This property suggests that near the equilibrium point $(\tilde{u}, \tilde{w}, \tilde{q}, \tilde{\theta}) = (0, 0, 0, 0)$ the Lipschitz constants can be estimated by gradient computation at that point for the whole trajectory. According to the results of this computation presented in Figure D.1, a plausible choice for the Lipschitz constants is

$$L_u = L_w = L_q = 2. \tag{D.2}$$

This particular choice is valid as long as the error variables do not stray too far from the equilibrium and it allows the computation of another variables of interest.

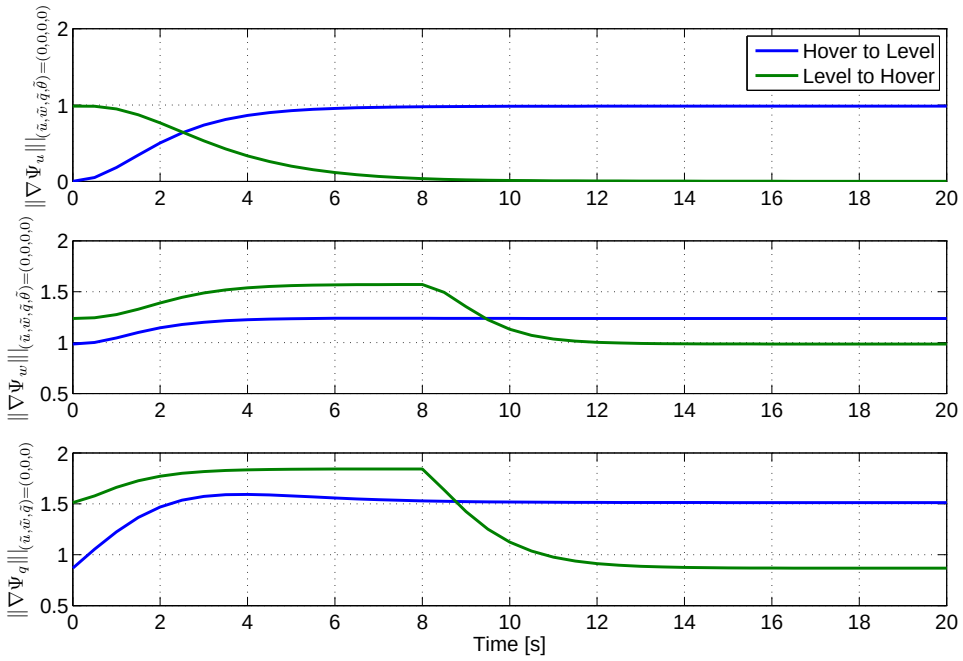

Figure D.1: Functions $\|\nabla\Psi_u(\tilde{u},\tilde{w},\tilde{q},\tilde{\theta},t)\|\Big|_{(\tilde{u},\tilde{w},\tilde{q},\tilde{\theta})=(0,0,0,0)}$, $\|\nabla\Psi_w(\tilde{u},\tilde{w},\tilde{q},\tilde{\theta},t)\|\Big|_{(\tilde{u},\tilde{w},\tilde{q},\tilde{\theta})=(0,0,0,0)}$ and $\|\nabla\Psi_q(\tilde{u},\tilde{w},\tilde{q},t)\|\|_{(\tilde{u},\tilde{w},\tilde{q})=(0,0,0)}$ representation.

D.2 Controller restrictions

The restrictions on the initial state are dependent on the selected gains and vice-versa. This loops requires an iterative process which is stopped when a satisfiable solution for the given problem is found. For the reader's convenience only the final solution is presented.

Consider the following restrictions on the initial state

$$\begin{aligned} c_u &= 0.1 \text{ m/s} \\ c_w &= 0.1 \text{ m/s} \\ c_q &= 0.02 \text{ rad/s} \\ c_\theta &= 0.02 \text{ rad,} \end{aligned} \tag{D.3}$$

and the controller gains

$$\begin{aligned} k_u &= 10 \text{ N.s/m} \\ k_w &= 10 \text{ N.s/m} \\ k_q &= 1 \text{ s} \\ k_\theta &= 10 \text{ N.m.s/rad,} \end{aligned} \tag{D.4}$$

The computation of l_1 and l_2 allows the determination of the level sets $\Omega_1(l_1)$ and $\Omega_2(l_2)$ and the

quantities $\bar{u}$, $\bar{w}$, $\bar{\theta}_1$ and $\bar{\theta}_2$. Taking into account the Lyapunov function definitions (4.44) and (4.56) it is possible to derive the relations (D.5).

$$\begin{aligned} l_1 =& \frac{1}{2}\left(c_u^2 + c_w^2\right) \\ l_2 =& \frac{1}{2}\left(\left(c_q + \frac{c_\theta}{k_q}\right)^2 + c_\theta^2\right) \end{aligned} \tag{D.5}$$

Substituting the values in (D.3) and (D.4) into (D.5) one finds that $l_1 = 0.01$ and $l_2 = 0.001$. The maximum velocity $\|(\tilde{u}, \tilde{w})\|$ and the maximum value of $\|(\theta_1, \theta_2)\|$ within the level sets $\Omega_1(l_1)$ and $\Omega_2(l_2)$, respectively, are given by

$$\begin{aligned} \overline{\|(\tilde{u}, \tilde{w})\|} &= \max_{(\tilde{u},\tilde{w})\in\Omega_1(l_1)} \|(\tilde{u}, \tilde{w})\| &&= \sqrt{2l_1}, \\ \overline{\|(\theta_1, \theta_2)\|} &= \max_{(\theta_1,\theta_2)\in\Omega_2(l_2)} \|(\theta_1, \theta_2)\| &&= \sqrt{2l_2}. \end{aligned} \tag{D.6}$$

Furthermore, it is possible to find that

$$\begin{aligned} \bar{u} = \bar{w} =& \sqrt{2l_1} \simeq 0.1414\text{m/s}, \\ \bar{\theta_1} =& \sqrt{2l_2} \simeq 0.0447\text{rad}, \\ \bar{\theta_2} =& \sqrt{2l_2} \simeq 0.0447\text{rad/s}, \end{aligned}$$

where

$$\begin{aligned} \bar{u} &= \max_{(\tilde{u},\tilde{w})\in\Omega_1(l_1)} |\tilde{u}|, & \bar{w} &= \max_{(\tilde{u},\tilde{w})\in\Omega_1(l_1)} |\tilde{w}|, \\ \bar{\theta}_1 &= \max_{(\theta_1,\theta_2)\in\Omega_2(l_2)} |\theta_1| \text{ and} & \bar{\theta}_2 &= \max_{(\theta_1,\theta_2)\in\Omega_2(l_2)} |\theta_2|. \end{aligned}$$

Having in mind the previous values it is possible to verify that the conditions $u^*(t) + \tilde{u} > 0$ and $|\arctan((w^*(t) + \tilde{w})/(u^*(t) + \tilde{u}))| < \bar{\alpha}$ for every value $\tilde{u}$ and $\tilde{w}$ belonging to the set $\Omega_1(l_1)$. The first condition verification is trivial but the same is not true for the second condition. Notice that the angle of attack is bounded as follows

$$\arctan\left(\frac{w^*(t) - \bar{w}}{u^*(t) + \bar{u}}\right) \leq \arctan\left(\frac{w^*(t) + \tilde{w}}{u^*(t) + \tilde{u}}\right)\Bigg|_{(\tilde{u},\tilde{w})\in\Omega_1(l_1)} \leq \arctan\left(\frac{w^*(t) + \bar{w}}{u^*(t) - \bar{u}}\right). \tag{D.7}$$

Plotting these bounds along the trajectories it is possible to find that the system remains within its domain even in the worst case scenario. Figure D.2 depicts these bounds and the reference trajectory.

The maximum value for $\tilde{q}$ within the level set $\Omega_2(l_2)$ is found by means of a constraint satisfaction problem which yields

$$\bar{q} = \max_{(\theta_1,\theta_2)\in\Omega_2(l_2)} \left|\theta_2 - \frac{\theta_1}{k_q}\right| = \left|k_q + \frac{1}{k_q}\right| \sqrt{\frac{2l_2}{k_q^2 + 1}}. \tag{D.8}$$

Substituting the variables k_q and l_2 into (D.8) one gets $\bar{q} = 0.0632$ rad/s.

The system's $(\tilde{u}, \tilde{w})$ input-to-state stability is indicated by the eigenvalues of the matrix

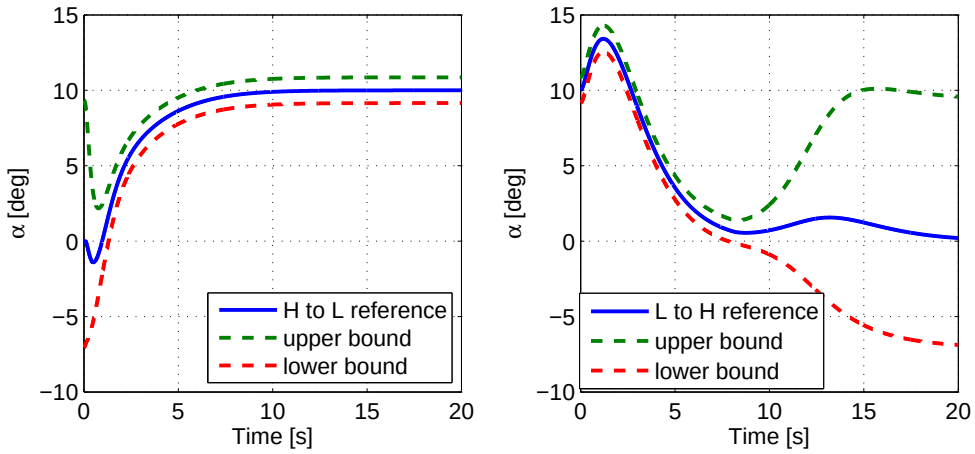

Figure D.2: Angle of attack reference trajectory, upper and lower bounds.

$$\begin{bmatrix} \frac{2k_u}{m} - L_u & \pm\frac{1}{2}(L_u + L_w) \\ \pm\frac{1}{2}(L_u + L_w) & \frac{k_w}{m} - L_w \end{bmatrix}$$

which naturally depend on the gains k_u and k_w. This dependence is shown in Figure D.3. Higher

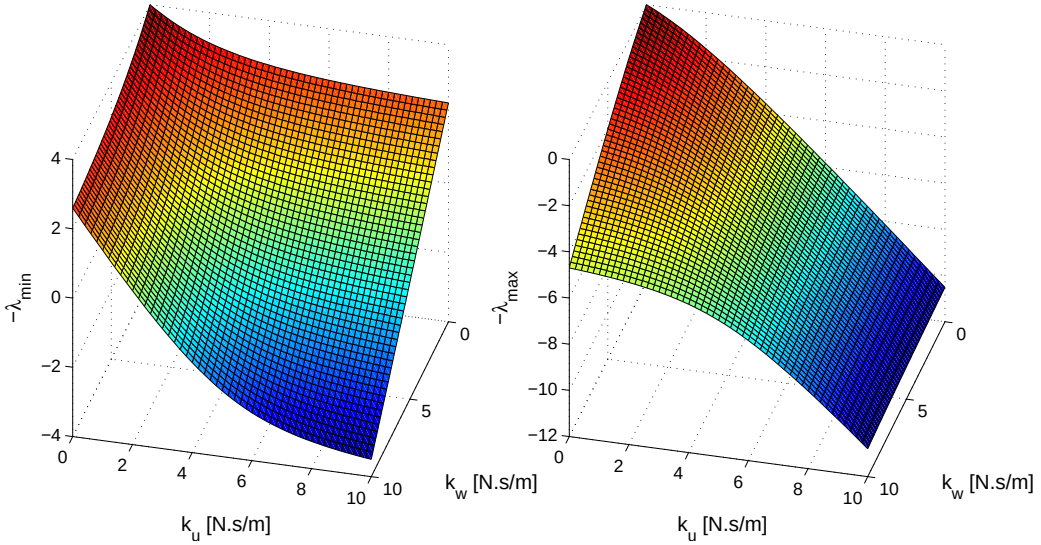

Figure D.3: $(\tilde{u}, \tilde{w})$ stability analysis.

gains decrease $-\lambda_{min}$ which in turn increases the system's stability and robustness, justifying the argument which was made in Section 4.4. Substituting the values in (D.4) into the matrix the following eigenvalues are obtained,

$$\lambda_{min} \simeq 3.5 \text{ and } \lambda_{max} \simeq 10.8,$$

justifying the system's input-to-state stability.

The Lyapunov function derivative in (4.60) can be upper bounded by (4.66) which is depicted in Figure D.4 for the worst case scenario $k_\theta = 0$ N.m/rad. The figure portraits some features which have already been discussed, including:

- The origin is a saddle point, i.e. the scalar map increases along the θ_2 direction and decreases along θ_1 and;
- It is possible to find a value $\underline{\theta_2}$ within the set $\Omega(\underline{l}, l_2)$ for any arbitrary number$\underline{l}$ satisfying $0 < \underline{l} < l_2$. Conversely, it is possible to find a value $\underline{l}$ for any given value $\underline{\theta_2}$.

Fixing $\underline{\theta_2} = 0.2$ rad/s it is possible to find $\underline{l}$ such that $0 < \underline{l} < l_2$ and also that $k_\theta^* \sim 5.1$ N.m/rad for $\Delta = 0$. Any value $k_\theta > k_\theta^*$ provides the ability to handle non-zero disturbances, i.e. even with $\Delta > 0$ the system state $(\tilde{\theta_1}, \tilde{\theta_2})$ remains within the level set $\Omega_2(l_2)$. It is noticeable in Figure D.4 the small set near the origin where $\dot{V}_2 < 0$ may not hold true.

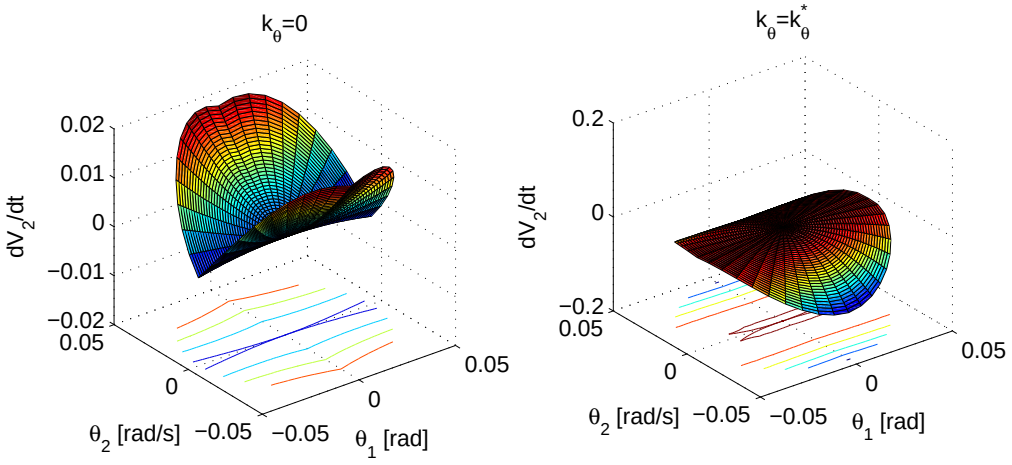

Figure D.4: Lyapunov function derivative upper bound representation within the level set $\Omega_2(l_2)$ for $k_\theta = 0$ (left hand side) and $k_\theta = k_\theta^*$ (right hand side).

Input-to-state stability of the overall system $(\tilde{u}, \tilde{w}, \theta_1, \theta_2)$ is guarateed if the condition$k_1 k_2 < 1$ holds true which is in fact the case because $k_1 k_2 \simeq 0.019$ taking into account the values presented throughout this section. Moreover, it is possible to verify that under all the previous considerations, the actuators do not reach saturation during the transition maneuvers. Similarly to the angle of attack analysis, the actuators T, δ_e and δ_f can be lower bounded by T_{min}, $\underline{\delta_e}(t)$ and $\underline{\delta_f}(t)$ and upper bounded by T_{max}, $\bar{\delta_e}(t)$ and $\bar{\delta_f}(t)$ such that for all possible values of $(\tilde{u}, \tilde{w}, \theta_1, \theta_2)$, the following conditions

$$T_{min} \leq T \leq T_{max}$$

$$\underline{\delta_e}(t) \leq \delta_e(t) \leq \bar{\delta_e}(t)$$
$$\underline{\delta_f}(t) \leq \delta_f(t) \leq \bar{\delta_f}(t)$$

hold true for all $t \geq 0$. These results are presented in Figures D.5, D.6 and D.7

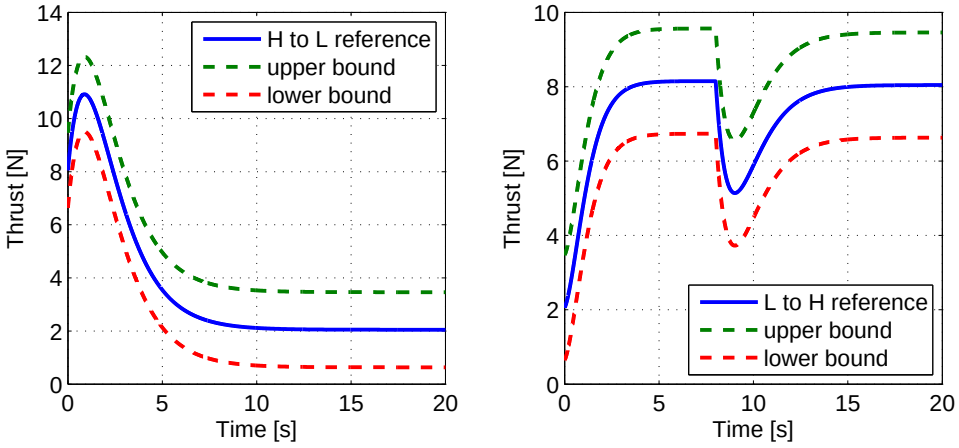

Figure D.5: Thrust reference trajectory, upper and lower bounds.

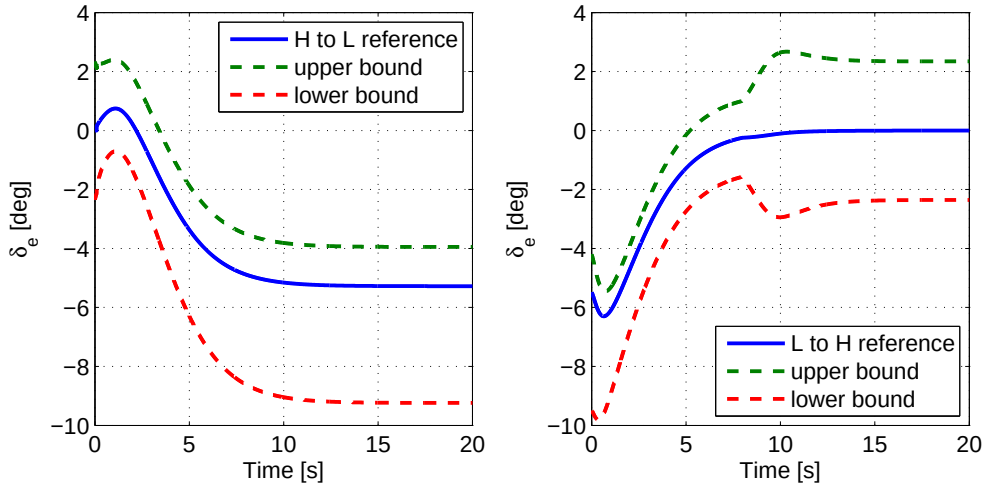

Figure D.6: Elevator deflection reference trajectory, upper and lower bounds.

D.3 Transition Maneuvers Simulation

In order to assess further the nonlinear controller's performance a Transition operating mode simulation was performed for the maneuvers $v^*_{X\to L}(t)$ and $v^*_{X\to H}(t)$ whose results are depicted in D.8 and D.9, respectively. The top row depicts the state variables u, w and θ evolution with time while

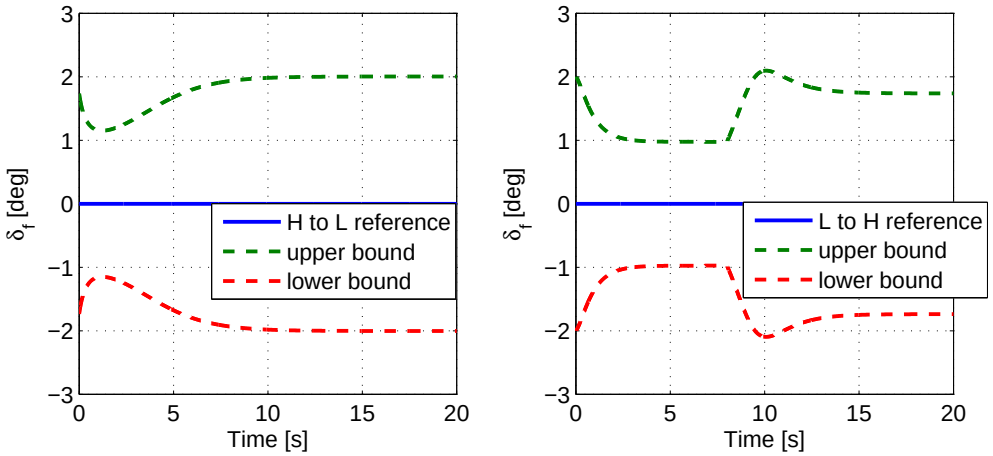

Figure D.7: Flap deflection reference trajectory, upper and lower bounds.

the bottom row depicts the actuators input. The state variables starting points are not coincident with the reference's starting points because the maximum allowable tracking error which is imposed by the controller restrictions is used. Moreover, the figures depict the upper and lower bounds where the variables may range according to the calculations performed in the previous section.

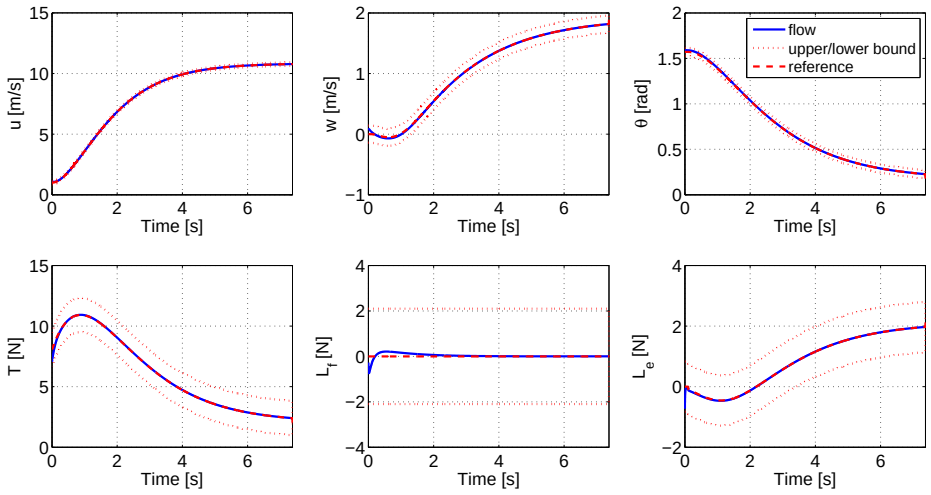

Figure D.8: Hover to Level flight transition maneuver simulation.

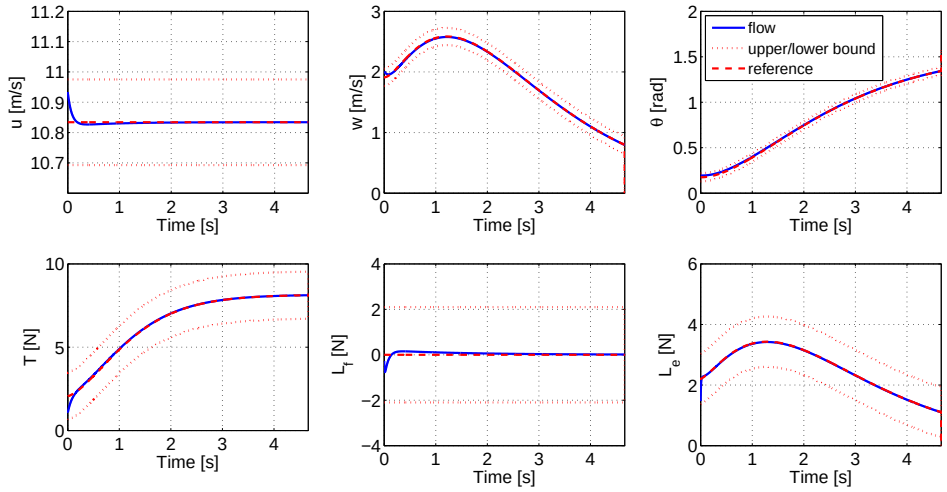

Figure D.9: Level to Hover transition maneuver simulation.

Bibliography

[1] Civilian applications: the challenges facing the uav industry. Air & Space Europe, 1999.

[2] T. Samad, J. Bay, and D. Godbole. Network-centric systems for military operations in urban terrain: The role of uavs. In *Proceedings of the IEEE*, 2007.

[3] G. Zhou and D. Zang. uav system for earth observation. *Geoscience and Remote Sensing Symposium*, 2007.

[4] William E. Green and Paul Y. Oh. A mav that flies like an airplane and hovers like a helicopter. In *Proceeding of the 2005 IEEE/ASME*, 2005.

[5] K. Ro, J. S. Oh, and L. Dong. Lessons learned: Application of small uav for urban highway traffic monitoring. In *45th AIAA Aerospace Sciences Meeting and Exhibit*, 2007.

[6] Frank Adrian, James S. McGrew, Mario Valenti, Daniel Levine, and Jonathan P. How. Hover, transition, and level flight control design for a single-propeller indoor airplane. In *AIAA Guidance, Navigation and Control Conference*, 2007.

[7] Alexis Lussier Desbiens, Alan Asbeck, and Mark Cutkosky. Hybrid aerial and scansorial robotics. In *IEEE Conference on Robotics and Automation*, 2010.

[8] Steven Cornelius Kriel. A comparison of control systems for the flight transition of vtol unmanned aerial vehicles. Master's thesis, University of Stellenbosch, 2008.

[9] R. Hugh Stone. *Modelling and control of mini-flying machines*, chapter 7. Springer, 2005.

[10] Nathan B. Knoebel. Adaptive quaternion control of a miniature tailsitter uav. Master's thesis, Brigham Young University, United States of America, 2007.

[11] Stephen R. Osborne. Transitions between hover and level flight for a tailsitter uav. Master's thesis, Brigham Young University, United States of America, 2007.

[12] Rafal Goebel, Ricardo G. Sanfelice, and Andrew R. Teel. Hybrid dynamical systems. *IEEE Control Systems Magazine*, 2009.

[13] Ricardo G. Sanfelice and Andrew R. Teel. A throw-and-catch hybrid control strategy for robust global stabilization of nonlinear system. In *American Control Conference*, 2007.

[14] L. Marconi, R. Naldi, and L. Gentili. A control framework for robust practical tracking of hybrid automata. In *Joint 48th IEEE Conference on Decision and Control and 28th Chinese Control Conference*, 2009.

[15] Daniel Liberzon and Stephen Morse. Basic problems in stability and design of switched systems. *IEEE Control Systems Magazine*, 1999.

[16] Roberto Naldi, Luca Gentili, and Lorenzo Marconi. Modeling and control of a flying robot interacting with the environment. *submitted to Automatica*, 2009.

[17] D. Cabecinhas, R. Naldi, L. Marconi, C. Silvestre, and R. Cunha. Robust take-off and landing for a quadrotor vehicle. In *IEEE Conference on Robotics and Automation*, 2010.

[18] Xenofon D. Koutsoukos, Panos J. Antsaklis, James A. Stiver, and Michael D. Lemmon. Supervisory control of hybrid systems. In *Proceedings of the IEEE*, 2000.

[19] Bernard Etkin and Lloyd Duff Reid. *Dynamics of Flight - Stability and Control*. John Wiley and Sons, Inc., 1996.

[20] Wu-Ki Tung. *Group Theory in Physics*. World Scientific Publishing Co., 1985.

[21] Richard Von Mises. *Theory of Flight*. General Publishing Company, 1959.

[22] Huibert Kwakernaak and Raphael Sivan. *Linear Optimal Control Systems*. John Wiley and Sons, Inc, 1972.

[23] Gene F. Franklin, J. David Powell, and Abbas Emami-Naeini. *Feedback Control of Dynamic Systems*. Addison-Wesley, 1994.

[24] Jean-Jacques E. Slotine and Weiping Li. *Applied Nonlinear Control*. Prentice Hall, 1991.

[25] José R. Azinheira. Sebenta de controlo de voo, 2008.

[26] Alberto Isidori, Lorenzo Marconi, and Andrea Serrani. *Robust Autonomous Guidance*. Springer, 2003.

[27] Hassan K. Khalil. *Nonlinear Systems*. Prentice Hall, 2002.

[28] Ricardo G. Sanfelice and Andrew R. Teel. Dynamical properties of hybrid systems simulators. *Automatica*, 46, 2009.

[29] Thomas C. Corke. *Design of Aircraft*. Prentice Hall, 2003.

[30] John D. Anderson. *Fundamentals of Aerodynamics*. McGraw-Hill, 1991.

[31] Ricardo G. Sanfelice. Matlab/simulink hybrid systems simulator. `http://www.u.arizona.edu/~sricardo/index.php?n=Main.Software`.